SURFACE PLASMON FLUORESCENCE MICROSCOPY: CHARACTERISTICS AND APPLICATION TO BIOIMAGING

TANG WAI TENG

(*B. Eng. (Hons), NUS*)

A THESIS SUBMITTED

FOR THE DEREE OF DOCTOR OF PHILOSOPHY

IN COMPUTATION AND SYSTEMS BIOLOGY (CSB)

SINGAPORE-MIT ALLIANCE

NATIONAL UNIVERSITY OF SINGAPORE

2010

Acknowledgments

First and foremost, thanks to my supervisors Prof. Colin Sheppard and Prof. Peter So for their guidance in my project, their patience and timely advice without which this work would not have been possible. I am also grateful to Peter for the time I spent at So Lab during my exchange at MIT. And not forgetting many thanks to the members of So Lab – Hyuk Sang Kwon, Euiheon Chung, Maxine Jonas, Jaewon Cha, Daekeun Kim, Heejin Choi, and Yanghyo Kim for making my stay a pleasant and memorable one. Special thanks go to Euiheon who taught me about his standing wave TIRF system, and who has remained a wonderful collaborator and great friend. Chapter six is a result of our collaboration together with Yanghyo.

I was fortunate to work with many wonderful people at Optical Bioimaging Lab – Kou Shan Shan, Naveen Balla, Shakil Rehman, Shalin Mehta, Elijah Yew, Zheng Wei, Si Ke, and Gong Wei. Thanks to them for making the lab a fun and pleasant place to work in. Our weekly Journal club was very enjoyable although our discussions always seemed to digress somehow. Also, special thanks to Naveen and Sounderya Nagarajan for their help with cell culturing. It was not always easy to find someone to coat the glass substrates. I am thus indebted to Naganivetha Thiyagarajah and Xu Yingshun for their help with thin film deposition. Finally, I am grateful to SMA for their support and funding over the past years for making this project possible. Last but not least, I wish to thank my parents for their support while I complete my studies.

Table of Contents

Table of Contents i

Summary iv

List of Tables vi

List of Figures vii

List of Symbols and Abbreviations x

CHAPTER 1: INTRODUCTION 1

1.1 Motivation 1

1.2 Literature Review 4

1.3 Background 6
1.3.1 Total Internal Reflection Fluorescence (TIRF) 6
1.3.2 Surface Plasmon Resonance (SPR) 12

1.4 An overview 17

CHAPTER 2: MODELING SURFACE PLASMON-COUPLED EMISSION MICROSCOPY 18

2.1 Surface Plasmon-Coupled Emission 18

2.2 Description of Angular Spectrum Representation 22

2.3 A Model for SPCEM 23
2.3.1 Excitation of dipole in the object space 23
2.3.2 Electric field in the image space 25
2.3.3 Addition of a linear polarizer in the detection path 32
2.3.4 Intensity in image space 33

CHAPTER 3: EXPERIMENTAL RESULTS OF SPCEM 35

3.1 Simulation Parameters 36

3.2 Radiation Characteristics of SPCEM **38**
3.2.1 *P*-polarized emission and fluorescence quenching 38
3.2.2 Back-focal plane image of SPCEM 41

3.3 Point Spread Function Characteristics of SPCEM **42**
3.3.1 Electric field distributions 42
3.3.2 Calculated intensity point spread function 45
3.3.3 Experimental set-up of SPCEM 45

3.4 Discussion **51**

CHAPTER 4: OPTICAL TRANSFER FUNCTION OF SURFACE PLASMON-COUPLED EMISSION MICROSCOPY **53**

4.1 Vectorial Optical Transfer Function **53**

4.2 Comparison between TIRFM and SPCEM **57**

4.3 Deconvolution for SPCEM **60**

CHAPTER 5: OPTICAL COMPENSATION FOR SURFACE PLASMON-COUPLED EMISSION MICROSCOPY **71**

5.1 Theoretical Basis **72**

5.2 Modification to SPCEM **75**
5.2.1 Spiral phase plate 76
5.2.2 Polarization mode converter 78
5.2.3 Comparison of SPP and PMC 80

5.3 Experimental Results **87**
5.3.1 Modified SPCEM imaging 92

CHAPTER 6: STANDING-WAVE SURFACE PLASMON-COUPLED EMISSION MICROSCOPY **98**

6.1 Background **98**

6.2 Theory **99**
6.2.1 Creating standing wave with *p*-polarized light 103
6.2.2 SW-SPRF algorithm and resolution 108

6.3 Experimental Results **110**
6.3.1 SW-SPRF set-up 110

CHAPTER 7: CONFOCAL SURFACE PLASMON RESONANCE FLUORESCENCE MICROSCOPY 117

7.1 SPR Excitation by Focused Beam.....118

7.2 Theory for Confocal SPRF 125

7.3 Experimental Results 127
7.3.1 Generation of radially polarized beam.....127
7.3.2 Confocal SPRF imaging.....129

7.4 Detection with Conversion Element 132

CHAPTER 8: PERSPECTIVES AND CONCLUSION 139

BIBLIOGRAPHY.....147

PUBLICATIONS 161

Summary

The characteristics of imaging through a metal-coated glass cover slip using the TIRF configuration are examined. This configuration makes use of surface plasmons to excite fluorescent molecules as well as to collect the emission light. Also known as surface plasmon coupled emission microscopy (SPCEM), the advantages of this method include better background rejection and reduced photobleaching due to decreased fluorescence lifetime. Through back and front focal plane imaging of subdiffraction-limit fluorescent beads, the experimental characteristics of surface plasmon-coupled emission microscopy are elucidated. Furthermore, at the angle at which surface plasmon resonance occurs, it is shown that the emission of fluorescent beads collected through the metal layer results in an irregular point spread function that has a donut-like morphology with multiple rings extending out. Based on the vectorial Debye-Wolf method, a model for the microscope is derived and used to compare with the experimental results. In addition, the vectorial OTF of the microscope is obtained and it is shown to have zero crossings and negative values which contribute to the donut shape morphology.

Because of the distorted point spread function, point spread function engineering approaches or numerical deconvolution are necessary to compensate for the irregularity for practical use in cellular imaging. Numerical deconvolution methods such as the Richardson-Lucy algorithm can compensate for the distortion. However, an optical method is preferable because of less sensitivity to noise. Due to

the anisotropic and highly *p*-polarized emission characteristics, we proposed to engineer the point spread function using a conversion element, either a radial to linear mode converter or a spiral phase plate, which can compensate for the distortion. Experimental results of compensated and uncompensated imaging using the conversion elements are presented. It is shown that the conversion elements can restore the point spread function to one which is single-lobed, either by rotating the polarization of the emission light or by modifying its wavefront. This change is beneficial for imaging. Further improvements to the resolution of the microscope can be achieved by using standing surface plasmon resonance waves. A sub-diffraction limited resolution of 120 nm is demonstrated by illuminating the sample with a standing wave and synthesizing the final image from three images of different phases. Finally, a confocal-based surface plasmon microscope is demonstrated which employs radially polarized illumination. This results in a tightly focused spot and better excitation. Together with a spiral phase plate in the detection path, its detection efficiency is shown to be improved without sacrificing the lateral resolution of the microscope.

List of Tables

Table 3-1 Values used for numerical simulation 38

List of Figures

Figure 1-1 Total internal reflection occurring at interface 7

Figure 1-2 Total internal reflection with *s*- and *p*-polarized beams 9

Figure 1-3 Intensity at interface while varying the angle of incidence 10

Figure 1-4 Plot of the penetration depth of the evanescent field 11

Figure 1-5 A metal and dielectric half-space supporting surface plasmons 13

Figure 1-6 Dispersion relation of surface plasmons 14

Figure 1-7 Geometry of the Kretschmann-Raether configuration 15

Figure 1-8 Right shift in the SPR reflectivity curve 16

Figure 2-1 Comparison of intensity enhancement 19

Figure 2-2 An objective-launched set-up for SPCE imaging 21

Figure 2-3 Excitation of dipole by *p*-polarized incident plane wave 24

Figure 2-4 A schematic view of the SPCEM imaging process 25

Figure 2-5 Axis convention used in the derivation of the field in medium 3 26

Figure 3-1 Contour plot of reflectivity 36

Figure 3-2 Family of reflectivity curves 37

Figure 3-3 Polar plot of the emission intensity of SPCEM 39

Figure 3-4 Plot of fluorescence collected by objective lens 40

Figure 3-5 Comparison of back-focal plane emission pattern of SPCEM 41

Figure 3-6 Electric field components for a perpendicular dipole 43

Figure 3-7 Electric field components for a parallel dipole 44

Figure 3-8 Intensity point spread function of SPCEM 45

Figure 3-9 Experimental set-up of SPCEM 46

Figure 3-10 Comparison of theoretical and experimental point spread function 49

Figure 3-11 Comparison of cross-sectional profile 50

Figure 4-1 Comparison of 2D vectorial OTF 58

Figure 4-2 Cross-section profile of vectorial OTFs 59

Figure 4-3 Image acquisition model 61

Figure 4-4 Flow chart for Richardson-Lucy deconvolution algorithm 63

Figure 4-5 Segment of the EIA 1956 resolution chart 64

Figure 4-6 Test images are blurred and degraded by noise 67

Figure 4-7 Simple inverse filtering 68

Figure 4-8 Wiener deconvolution 69

Figure 4-9 Richardson-Lucy deconvolution 70

Figure 5-1 Polarization pattern of the electric field 72

Figure 5-2 A log-log plot of the vectorial OTFs 73

Figure 5-3 Proposed modified SPCEM imaging 76

Figure 5-4 A spiral phase plate 77

Figure 5-5 A polarization mode converter 81

Figure 5-6 A comparison of the cross-sectional profile of vectorial OTFs 83

Figure 5-7 Point spread function comparison of SPCEM 85

Figure 5-8 Characteristics of SPP and PMC errors 86

Figure 5-9 Experimental set-up with SPP and PMC 87

Figure 5-10 Experimental results for SPP 90

Figure 5-11 Experimental results for PMC 91

Figure 5-12 Comparison of simulation and experimental results for SPP 93

Figure 5-13 Comparison of simulation and experimental results for PMC 94

Figure 5-14 SPCEM images of HeLa cells 96

Figure 6-1 Schematic diagram illustrating standing-wave excitation 102

Figure 6-2 Standing wave patterns 106

Figure 6-3 Contrast of *p*-polarized standing-waves 107

Figure 6-4 Modified standing-wave algorithm 108

Figure 6-5 Simulation of point spread function 110

Figure 6-6 Schematic diagram of the experimental set-up 111

Figure 6-7 Extended resolution imaging with standing-wave surface plasmons 115

Figure 7-1 Effects of focusing radially polarized light 119

Figure 7-2 Axis convention 121

Figure 7-3 Focused beam excitation with linearly polarized light 122

Figure 7-4 Focused beam excitation with radially polarized light 123

Figure 7-5 Plot of normalized transmission coefficient 125

Figure 7-6 Illustration of calculation of confocal SPRF 127

Figure 7-7 Linear to radial polarization converter 128

Figure 7-8 Comparison of point spread function 131

Figure 7-9 Comparison of power collected by pinhole 134

Figure 7-10 Comparison of power collected by pinhole for NA 1.45 objective 136

Figure 7-11 Comparison of images without and with SPP 137

List of Symbols and Abbreviations

$\otimes$	Convolution operation
2D	Two dimensional
3D	Three dimensional
CCD	Charged coupled device
FFT	Fast Fourier Transform
$FT_{2D}[\bullet]$	2D Fourier transformation
FWHM	Full-width at half-maximum
NA	Numerical aperture
OTF	Optical transfer function
PMC	Polarization mode converter
SPR	Surface plasmon resonance
SPCE	Surface plasmon coupled emission
SPCEM	Surface plasmon coupled emission microscopy
SPP	Spiral phase plate
SW	Standing wave
TE	Transverse electric
TIRF	Total internal reflection fluorescence
TIRFM	Total internal reflection fluorescence microscopy
TM	Transverse magnetic

CHAPTER 1: INTRODUCTION

1.1 Motivation

Presently, there exist many microscopy techniques available for visualizing tissues and biological samples, which can help scientific investigation and discovery in many areas such as in tissue pathogenesis as well as in probing of cellular processes. Each of these techniques varies in its ability to discriminate objects, for example, in terms of lateral or axial resolution, depth of field, as well as their applicability or suitability for a particular imaging study. The various imaging methods can be broadly classified into label-free techniques, and fluorescence techniques which make use of fluorescent probes introduced into the sample for imaging. For label-free methods, there are phase contrast methods such as Differential Interference Contrast (DIC), methods based on interference such as Optical Coherence Tomography (OCT), or Second Harmonic Generation (SHG) microscopy which rely on the scattering or phase properties of the sample under investigation. For fluorescence methods, techniques such as Confocal Laser Scanning Fluorescence Microscopy (CLSFM) and Multi-Photon Excitation (MPE) microscopy are commonly used for imaging due to advantages such as 3D

sectioning capability arising from the rejection of out-of-focus fluorescence or improved tissue penetration owing to longer wavelength used in MPE.

For imaging biological specimens, an advantage of using fluorescent probes is that the signal-to-background ratio is relatively high since only proteins of interest are labeled. Another advantage is the ability to study cellular processes that would otherwise be impossible with non-fluorescent techniques owing to the specificity achievable by tagging the proteins under study with fluorescence labels. This makes fluorescence imaging one of the commonly used tools of biologists. While CLSFM is commonly used in many biological studies, for situations where it is required to study processes near the cell membrane, a surface imaging technique called Total Internal Reflection Fluorescence Microscopy (TIRFM) (Axelrod 2001) is preferred due to its better axial resolution and improved background rejection. This favorable characteristic of TIRFM stems from the fact that the fluorescent probes are excited by the evanescent waves when light at the glass and water interface is totally internally reflected due to the incident angle being larger than the critical angle of the medium. Depending on the angle of incidence of the incoming beam, the depth of the evanescent waves is typically restricted to about 100 nm near the surface of the interface, and this contributes to the good axial resolution as compared to confocal microscopy which has an optical section of approximately 500 nm. This quality of TIRFM makes it ideal for probing processes near the cell membrane. For instance, this technique has been used to study actin dynamics (Sund and Axelrod 2000), exocytosis (Steyer et al. 1997) as well as receptor-ligand binding (Schmid et al. 1998).

At the same time as developments in fluorescence techniques rapidly progressed over the past few decades, interest in another area involving surface plasmons was renewed and gained momentum, especially over the past ten years after Ebbesen and coworkers' discovery of the surface plasmons' role in the extraordinary transmission of light through sub-wavelength holes in metal (Ebbesen et al. 1998). Since then, there has been a lot of research into using surface plasmons in negative index metamaterials and cloaking (Veselago 1968; Schurig et al. 2006), in a perfect lens (Fang et al. 2005; Pendry 2000; Smolyaninov et al. 2007), and in optical waveguides (Bozhevolnyi et al. 2001; Weeber et al. 1999).

In addition, apart from the engineering applications listed above, studies into the application of surface plasmons in biology have also been ongoing. For instance, the use of plasmonic gold nanoparticles has been investigated as a contrast agent in OCT due to the enhanced scattering caused by surface plasmons (Kah et al. 2009; Lin et al. 2005), and as a possible aid in photodynamic therapy due to their increased absorption cross-section (Huang et al. 2007; Loo et al. 2005). In the field of biosensing applications, developments utilizing surface plasmons have also been active. For example, surface plasmon coupling between gold or silver particles has been demonstrated as an optical ruler, with the ability to monitor intramolecular distances of approximately 70 nm without photobleaching unlike Förster Resonance Energy Transfer (FRET) (Sönnichsen et al. 2005). More importantly, before these recent advances, surface plasmons have long been used for sensitive and quantitative biosensing applications such as for quantifying the kinetics of biomolecular interactions (Liedberg 1983; Fägerstam et al. 1992). Likewise, the first surface

plasmon resonance based biosensor instrument was commercially available in 1992 and has been used in a number of key areas such as food analysis, drug discovery and biotherapeutics (Biacore 2010). Recent advances in the surface plasmon resonance (SPR) biosensor include improved sensitivity and resolution as well as higher throughput detection (Slavík and Homola 2007; Alleyne et al. 2007; Piliarik et al. 2005).

While progress has been made in many areas mentioned above, to date there have not been many studies devoted to understanding the application of surface plasmons to bioimaging, much less to fluorescence microscopy. In many of the previous studies, the investigators mainly made use of the reflectivity and transmission characteristics of surface plasmons. But the use of surface plasmons involving fluorescence excitation and emission in microscopy up till now has not been amply studied. The aim of this thesis is therefore to study the effects of using surface plasmons specifically to fluorescence imaging and to elucidate the properties of such an imaging modality in order to properly understand its characteristics and applicability for imaging purposes.

1.2 Literature Review

In this section, we review some of the prior work that has so far been carried out to apply surface plasmons to microscopy and look at some of the applications that have been explored. The use of surface plasmons in microscopy was initially proposed as a way to measure small variations on surfaces (Rothenhäusler and Knoll 1988; Yeatman and Ash 1987). This is due to the sensitivity of the surface plasmons to

small changes in the local dielectric environment of the surfaces. In effect, small changes to the refractive index near a metal coated surface can give rise to a larger change in the reflectivity and transmission of light at that interface, therefore a high sensitivity can be achieved by simply detecting the change in the reflectivity of the light. Experiments have shown the thickness sensitivity to be about 3Å while lateral resolution is in the order of 25μm. Kano has proposed using a focused laser beam to excite surface plasmons and scanning the surface plasmon probe to form an image (Kano 2000; Kawata 2001). Somekh analysed and simulated two-photon and second harmonic surface plasmon microscopy with input beams of linear and circular polarizations (Somekh 2002) while Stabler proposed a Köhler illuminated configuration (Stabler et al. 2004). Other input polarizations such as radial polarization have been recently demonstrated for single photon as well as two-photon imaging (Moh et al. 2008, 2009). Recently, Giebel and coworkers made use of surface plasmons to quantify the distance of a cell membrane from the substrate (Giebel et al. 1999). It is to be noted that the above works were based on the reflectivity and transmission characteristics of surface plasmon resonance, where one disadvantage is the long propagation length of surface plasmons which leads to a poor lateral resolution.

Instead of using the reflectivity characteristics, surface plasmons can also be used to excite fluorescent molecules (Kitson et al. 1996). For example, Yokota demonstrated single molecule fluorescence imaging of proteins using surface plasmon excitation (Yokota et al. 1998) while Borejdo and coworkers used it with fluorescence correlation spectroscopy to study the dynamics of molecules (Borejdo, Calander, et al.

2006). It has been shown that the enhanced electric field caused by surface plasmons at the metal surface leads to a higher intensity of fluorescence signal (He et al. 2006; Hung et al. 2006). Furthermore, it was also shown that the metal surface contributes to decreased lifetime of fluorescent molecules, which delays photobleaching (Chance et al. 1974; Drexhage 1970; Lukosz and Kuhn 1977; Vasilev et al. 2004), and can be beneficial for fluorescence imaging. Recently, surface plasmons were also used to image fluorescently labeled muscle fibers (Borejdo, Gryczynski, et al. 2006; Burghardt et al. 2006). The technique used was based on the TIRF configuration and the effect used is also commonly known as surface plasmon-coupled emission where the detection optics reside on the same side as the excitation optics (Gryczynski et al. 2004b; Lakowicz et al. 2003). So far, these experiments have been conducted using fluorescence in surface plasmon microscopy without having a clear comprehension of its imaging properties and characteristics. It is therefore the aim of this thesis to study in detail the imaging characteristics of surface plasmon microscopy.

1.3 Background

In the following sections, the concepts of Total Internal Reflection Fluorescence (TIRF) and Surface Plasmon Resonance (SPR) are briefly reviewed.

1.3.1 Total Internal Reflection Fluorescence (TIRF)

Total internal reflection can occur when light travels from a medium with a high refractive index to one with a low refractive index, for example from glass to air. According to Snell's Law which can be derived by considering the boundary

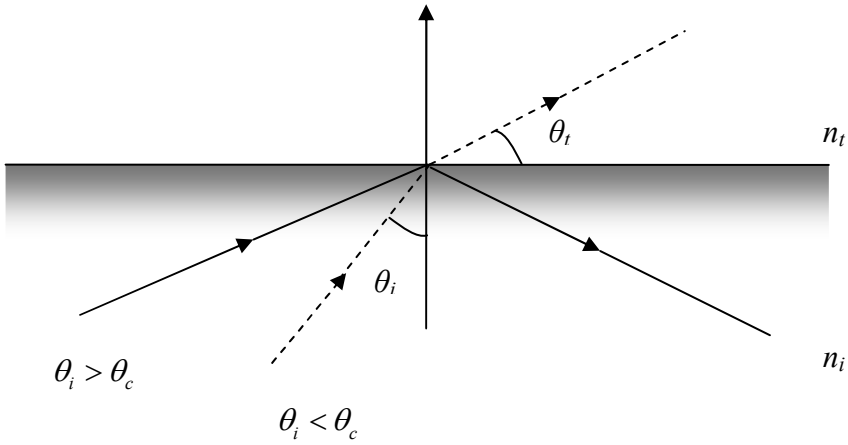

Figure 1-1. Total internal reflection occurs when light travels from a high refractive index medium to a lower refractive index medium with an incident angle larger than the critical angle (solid line), otherwise the ray is refracted (dash line).

conditions for Maxwell's Equations, the condition for this to happen is when the angle of the incident light at the glass and air interface is greater than the critical angle (Hecht 2002). From Snell's Law,

$$n_i \sin\theta_i = n_t \sin\theta_t, \tag{1.1}$$

where n_i and n_t denote the refractive index of the first (higher refractive index) and second (lower refractive index) medium, and θ_i and θ_t denote the angles the incident and refracted rays make with the normal at the interface of the media. Therefore, when total internal reflection starts to occur, the refracted angle is at right angles to the normal and the critical angle is therefore defined as

$$\theta_c = \sin^{-1}\frac{n_t}{n_i} = \sin^{-1}\eta, \tag{1.2}$$

where η is the ratio of the refractive indices of the media. This is depicted in Figure 1-1 for two cases, one for which the incident angle is less than the critical angle, and the other where it is greater than the critical angle.

When total internal reflection occurs, an evanescent field is set up at the interface between the two media. The evanescent field is a localized and non-propagating field decaying in the axial direction but propagating in the transverse direction. This can be seen in the following equations. Assuming that the incident light which has *s*-polarization is given by

$$\mathbf{E}_{\mathbf{s,i}} = \begin{bmatrix} 0 \\ 1 \\ 0 \end{bmatrix} \exp\left(ik_i x \sin\theta_i + ik_i z \cos\theta_i\right), \tag{1.3}$$

where k_i denotes the incident wave vector and θ_i is the incident angle, then under total internal reflection, the transmitted field and intensity can be expressed as

$$\mathbf{E}_{\mathbf{s,t}} = t_s \begin{bmatrix} 0 \\ 1 \\ 0 \end{bmatrix} \exp\left(ik_i x \sin\theta_i\right) \exp\left(-k_i z \sqrt{\sin^2\theta_i - \eta^2}\right), \tag{1.4}$$

$$I_s = \left|t_s\right|^2 \exp\left(-2k_i z \sqrt{\sin^2\theta_i - \eta^2}\right). \tag{1.5}$$

From the above equations, it is evident that the evanescent field and the intensity decay exponentially away from the interface with increasing *z*. Hence the field is localized and does not propagate in the *z* direction; however it still propagates in the *x* direction. In addition, it is also possible for total internal reflection to occur when the incident light is *p*-polarized (see Figure 1-2). The related expressions when using *p*-polarized light are

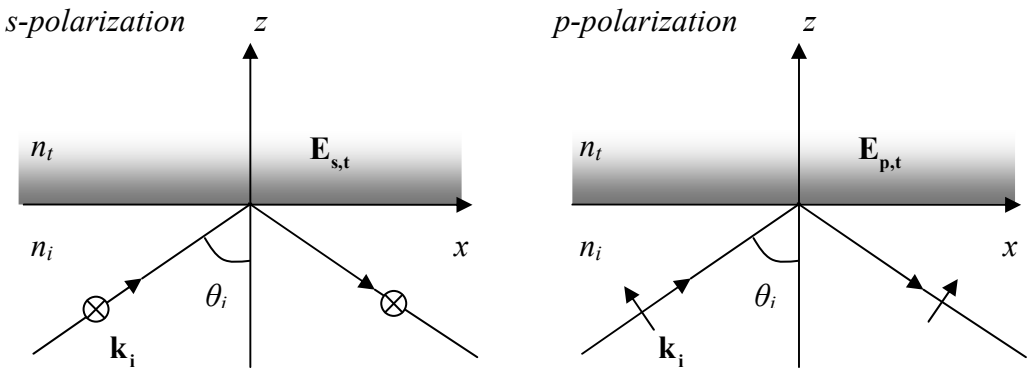

Figure 1-2. Total internal reflection with *s*- and *p*-polarized incident beams result in an evanescent field that decays exponentially with increasing *z*.

$$\mathbf{E}_{\mathbf{p,i}} = \begin{bmatrix} -\cos\theta_i \\ 0 \\ \sin\theta_i \end{bmatrix} \exp\left(ik_i x \sin\theta_i + ik_i z \cos\theta_i\right), \tag{1.6}$$

$$\mathbf{E}_{\mathbf{p,t}} = \frac{t_p}{\eta} \begin{bmatrix} -i\sqrt{\sin^2\theta_i - \eta^2} \\ 0 \\ \sin\theta_i \end{bmatrix} \exp\left(ik_i x \sin\theta_i\right) \exp\left(-k_i z \sqrt{\sin^2\theta_i - \eta^2}\right), \tag{1.7}$$

$$I_p = \left|\frac{t_p}{\eta}\right|^2 \left(2\sin^2\theta_i - \eta^2\right) \exp\left(-2k_i z \sqrt{\sin^2\theta_i - \eta^2}\right). \tag{1.8}$$

The Fresnel transmission coefficients t_s, t_p are given by

$$\begin{aligned} t_s &= \frac{2\cos\theta_i}{\cos\theta_i + i\sqrt{\sin^2\theta_i - \eta^2}}, \\ t_p &= \frac{2\eta\cos\theta_i}{\eta^2\cos\theta_i + i\sqrt{\sin^2\theta_i - \eta^2}}. \end{aligned} \tag{1.9}$$

For both *s*- and *p*-polarized incident light, the resulting evanescent field is capable of exciting fluorophores which are placed at the interface (Axelrod 2001). It is noted that for *p*-polarized incident light, there exists a 90 degrees phase difference

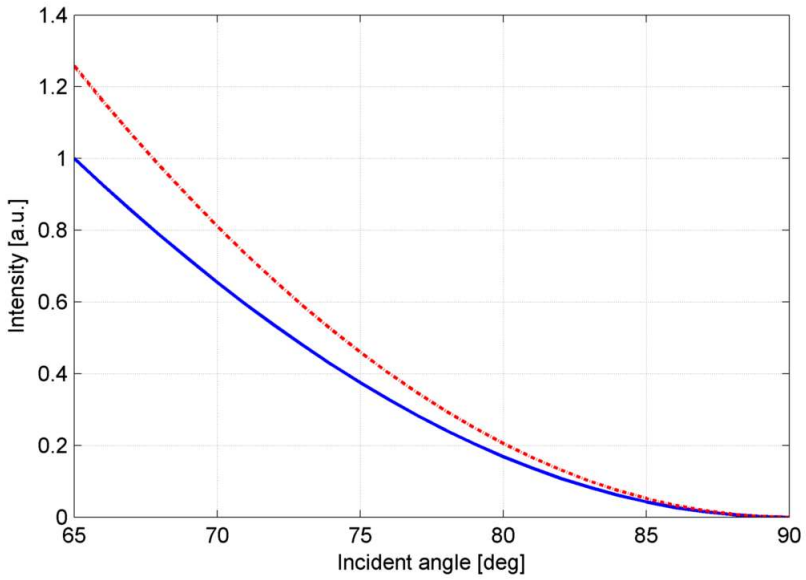

Figure 1-3. Intensity at interface while varying the angle of incidence for *s*-polarized light (solid line) and *p*-polarized light (dash line).

between the *x* and *z* components, which implies having circular polarization in the *x*-*z* plane. The penetration depth of the evanescent field is given by the expression

$$\delta = \frac{\lambda_0}{4\pi n_i \sqrt{\sin^2 \theta_i - \eta^2}} \tag{1.10}$$

where λ_0 is the wavelength in free space. For light within the visible range, the penetration depth of the evanescent field is typically around 100 nm ~ 200 nm. Comparing this with the axial sectioning of confocal microscopy of about 500 nm, the thinner optical section of the evanescent field gives rise to better out-of-focus rejection, thus providing an improved imaging capability for fluorescence emission which is close to the substrate. This feature of TIRF can be used to great advantage in various studies that probe processes close to the cellular membrane. Figure 1-3 shows a plot of the intensity at $z = 0$ as a function of the angle of incidence for both *s*- and

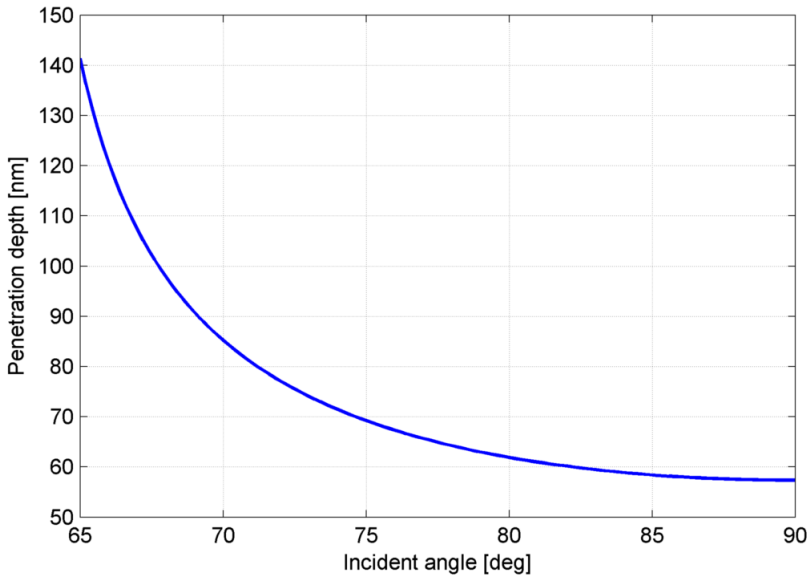

Figure 1-4. Plot of the penetration depth of the evanescent field as a function of angle of incidence of *s*-polarized light.

p-polarized light with $n_i = 1.5$, $n_t = 1.33$ and $\lambda_0 = 500\text{nm}$ while Figure 1-4 plots the penetration depth as a function of the angle of incidence. These plots show that as the angle of incidence is increased, both the intensity and penetration depth decrease. Hence, a compromise must be made between the desired intensity which affects the signal-to-noise and the penetration depth which affects the out-of-focus rejection.

While TIRF can be implemented using a prism, it is also commonly integrated into a microscope that uses an objective launched configuration owing to system simplicity and ease of use. Many vendors such as Olympus and Leica have commercialized TIRF systems based on an objective launched configuration. This configuration will be described in more detail in the next chapter.

1.3.2 Surface Plasmon Resonance (SPR)

Surface Plasmon Resonance (SPR) is a phenomenon in which free electrons near the surface of a metal-dielectric interface oscillate coherently in response to an applied electromagnetic field. These charged oscillations are accompanied by a mixed transversal and longitudinal electromagnetic field which decays exponentially, and result in an enhanced field inside the dielectric medium which can be used to excite fluorescent probes. As a variation to TIRF, the effect of SPR can also be employed to set up an evanescent field for exciting fluorescent probes near the interface layer. This is normally done by coating the cover slip with a thin layer of metal such as gold. The advantage of SPR over TIRF is that the evanescent field set up with SPR is enhanced many times over that of TIRF and this contributes to more efficient excitation of the fluorophores for the same excitation power. Furthermore, together with the wavelength dependency of SPR that tends to suppress background noise due to autofluorescence, these characteristics result in an improvement in the signal-to-noise ratio of SPR imaging.

The criteria for supporting surface plasmons can be obtained by considering the transverse magnetic (TM) solution to a semi-infinite metal and dielectric half-space as shown in the illustration in Figure 1-5. It is also worthwhile to note that the transverse electric (TE) equations do not yield any solution, implying that surface plasmon modes are only supported for a *p*-polarized incident beam and not an *s*-polarized beam. For $z < 0$, the fields are described by the following equations,

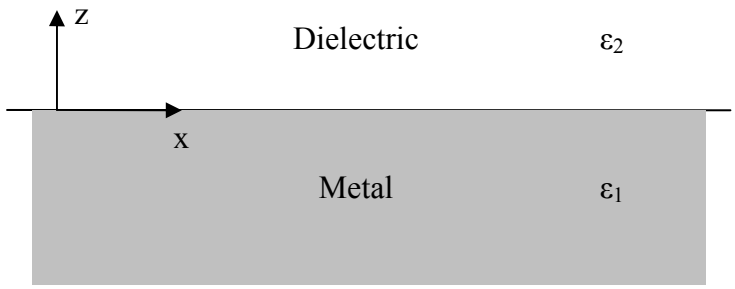

Figure 1-5. A metal and dielectric half-space supporting excitation of surface plasmons.

$$
\begin{aligned}
H_y(z) &= A_1 e^{ik_x x} e^{k_{1z} z} \\
E_x(z) &= -\frac{iA_1 k_{1z}}{\omega \varepsilon_0 \varepsilon_1} e^{ik_x x} e^{k_{1z} z} \\
E_z(z) &= -\frac{A_1 k_x}{\omega \varepsilon_0 \varepsilon_1} e^{ik_x x} e^{k_{1z} z}
\end{aligned}
\tag{1.11}
$$

and for $z > 0$,

$$
\begin{aligned}
H_y(z) &= A_2 e^{ik_x x} e^{-k_{2z} z} \\
E_x(z) &= \frac{iA_2 k_{2z}}{\omega \varepsilon_0 \varepsilon_2} e^{ik_x x} e^{-k_{2z} z} \\
E_z(z) &= -\frac{A_2 k_x}{\omega \varepsilon_0 \varepsilon_2} e^{ik_x x} e^{-k_{2z} z}
\end{aligned}
\tag{1.12}
$$

where k_x is the surface wave vector and A_1, A_2 are field amplitudes. k_{1z}, k_{2z} are the wave vectors normal to the interface and $\varepsilon_1, \varepsilon_2$ are the permittivity of each medium respectively. Considering boundary conditions at the interface $z = 0$ results in the following conditions

$$
\begin{aligned}
A_1 &= A_2, \\
\frac{k_{2z}}{k_{1z}} &= -\frac{\varepsilon_2}{\varepsilon_1}.
\end{aligned}
\tag{1.13}
$$

Combining these equations with the relations

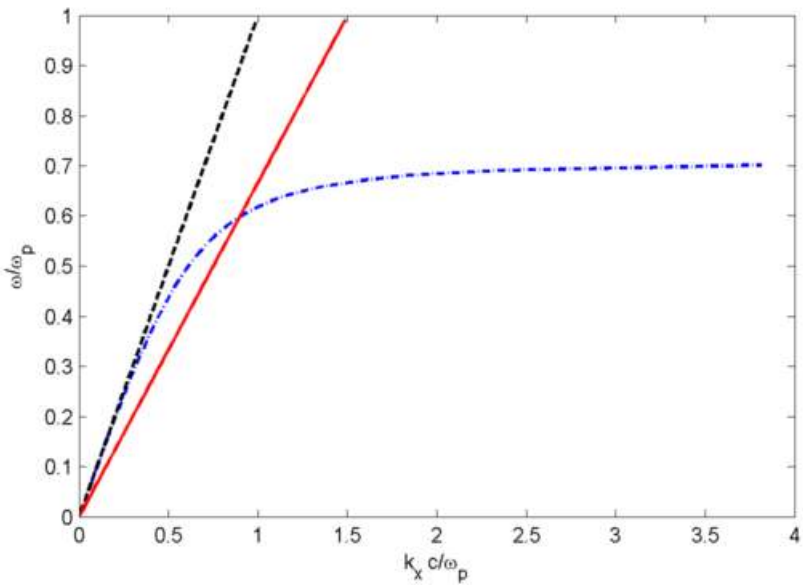

Figure 1-6. Dispersion relation of surface plasmon (dash-dotted line), light line (dashed line) and with ATR coupling method (solid line).

$$\begin{aligned} k_x^2 &= k_0^2\varepsilon_1 - k_{1z}^2 \\ k_x^2 &= k_0^2\varepsilon_2 - k_{2z}^2, \end{aligned} \tag{1.14}$$

one can then obtain the dispersion relation for surface plasmons as

$$k_x = \frac{\omega}{c}\sqrt{\frac{\varepsilon_1\varepsilon_2}{\varepsilon_1+\varepsilon_2}}. \tag{1.15}$$

The dispersion relation for surface plasmons is plotted in Figure 1-6 where it is normalized to the plasma frequency ω_p. The Drude model is assumed for the metal layer. It can be seen from the graph that the light line lies to the left and does not intersect the dispersion curve of surface plasmons. Because of this, the surface plasmon mode does not occur naturally. In order to excite surface plasmons by photons, it is necessary to match the phase of the impinging photons to that of the surface plasmons. This can be done via different methods such as excitation by attenuated total reflection (ATR) or by coupling with a grating coupler. For the ATR

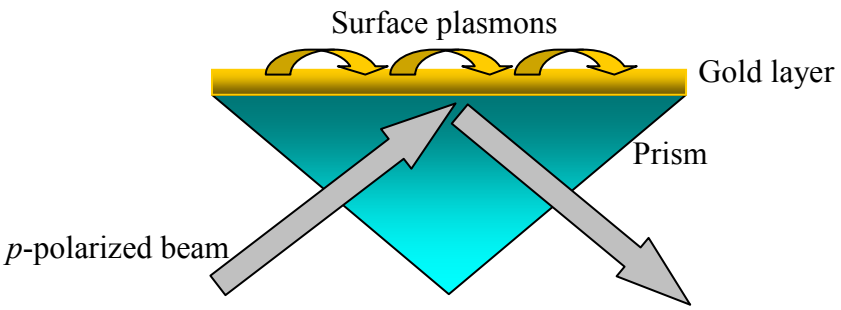

Figure 1-7. Geometry of the Krestchmann-Raether configuration for exciting surface plasmons.

method, there exist two methods – the Otto configuration and the Kretschmann-Raether configuration, of which the Kretschmann-Raether configuration is the most commonly used. The solid line in the figure shows the effect of exciting surface plasmons using the ATR method. In terms of configuration, the ATR coupler makes use of a prism geometry similar to prism-TIRF except with an additional metal layer coated on top of the glass prism as shown in Figure 1-7. Owing to the higher refractive index of the ATR coupler, the gradient of the light line is modified so that it is gently sloping and intersects with the SPR dispersion curve, implying that surface plasmons can be excited. Factors that affect the generation of SPR include the type of metal layer used, the thickness of the metal layer, the angle of incidence of the *p*-polarized incident beam and the refractive index of the dielectric medium (Raether 1988).

With the induced surface plasmons, one can employ them for exciting fluorescent probes placed at the metal-dielectric interface. Alternatively, because of the sensitivity of the SPR effect to changes in the refractive index of the dielectric environment, SPR can also be used in bioaffinity measurements where binding events

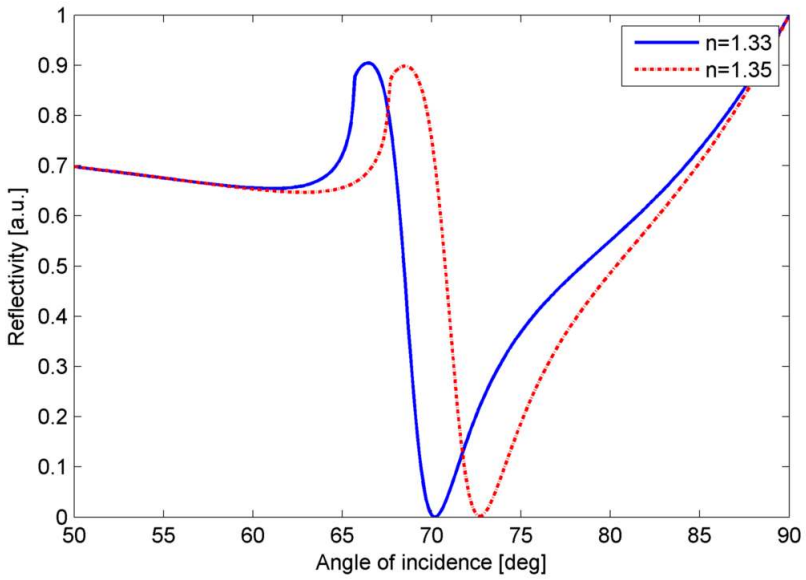

Figure 1-8. A right shift in the SPR reflectivity curve due to a small change in the refractive index of the environment from *n*=1.33 (solid line) to *n*=1.35 (dashed line).

resulting in changes to the refractive index may be detected. For example, by employing the Kretschmann-Raether configuration of Figure 1-7, the reflective curve of SPR can be plotted for three layers of glass-silver-water for an excitation wavelength of 520 nm as shown in Figure 1-8. In the plot, when the refractive index of the environment changes from 1.33 to 1.35, the reflectivity curve shifts to the right by about 3 degrees. Detection of this shift can allow for quantitative measurement of the refractive index change.

Instruments based on this principle which makes use of SPR reflectivity shifts for measuring interaction between biomolecules are commercially available. Furthermore, in the area of two dimensional imaging, the reflectivity characteristics of surface plasmons have been used in microscopy (Rothenhäusler and Knoll 1988; Yeatman and Ash 1987). Examples where application of surface plasmon microscopy

(SPM) have been demonstrated include imaging of liquid crystals (Evans et al. 1997), real-time imaging of birefringent samples (Tanaka and Kawata 2005) and imaging of cell-substrate contacts of living cells (Giebel et al. 1999).

1.4 An overview

The rest of the thesis focuses on analyzing the characteristics of combining Surface Plasmon Resonance with the configuration of a TIRF microscope into a form of surface plasmon fluorescence microscopy also known as surface plasmon-coupled emission microscopy (SPCEM) for bioimaging. Chapter two describes surface plasmon-coupled emission microscopy and derives the imaging theory as well as the point spread function. In chapter three, experimental results are compared with simulation based on the derived theory. The characteristics of the microscope are also reviewed. In particular, the distorted point spread function characteristics are pointed out. Chapter four analyzes the resolution of the microscope in terms of the optical transfer function. Deconvolution methods that compensate for the distortion are analyzed. Chapter five discusses optical methods to compensate for the aberrations to the point spread function. Experimental results are also presented. Chapter six introduces a technique to improve the resolution of the microscope based on standing-wave excitation. In chapter seven, the scanning surface plasmon microscope is introduced and studied in detail. Finally, chapter eight concludes the thesis.

CHAPTER 2: MODELING SURFACE PLASMON-COUPLED EMISSION MICROSCOPY

Both total internal reflection (TIR) and surface plasmon resonance (SPR) share similarities in terms of their set-up. In addition, their evanescent fields can be used to excite fluorescent molecules. In this chapter, the effect of combining SPR with the TIR set-up and detection of the emission light is discussed. Furthermore, this is applied to microscopy using an objective-launched set-up and is called the SPCE microscope (SPCEM). The image formation and point spread function are then derived for the SPCE microscope.

2.1 Surface Plasmon-Coupled Emission

The effect of surface plasmon-coupled emission (SPCE) was studied both theoretically and experimentally by a few investigators, where it was initially proposed as a high sensitivity detection measurement technique for fluorescence (Gryczynski et al. 2004a; Lakowicz 2004; Lakowicz et al. 2003). In SPCE, the set-up typically uses the Kretschmann-Raether configuration, which is similar to the TIRF

configuration. Introduction of the metal layer on top of the prism allows excitation of the fluorescent molecules by surface plasmon resonance. Such a combination allows more efficient energy transfer from photons to the fluorescent molecules than normal TIRF due to the coupling via surface plasmons. The fluorescence emission is then detected on the same side as the excitation optics after the outcoupling of the emission light via surface plasmons. SPCE has been used in many applications in biotechnology and biological measurements. For example, the use of SPCE was demonstrated in DNA hybridization measurements (Malicka et al. 2003), and in immunoassays (Matveeva, Z. Gryczynski, I. Gryczynski, and Lakowicz 2004; Matveeva, Z. Gryczynski, I. Gryczynski, Malicka, and Lakowicz 2004) where sensitive detection of myoglobin was demonstrated. It was also used to extend fluorescence correlation spectroscopy to improve its signal-to-noise ratio (Borejdo,

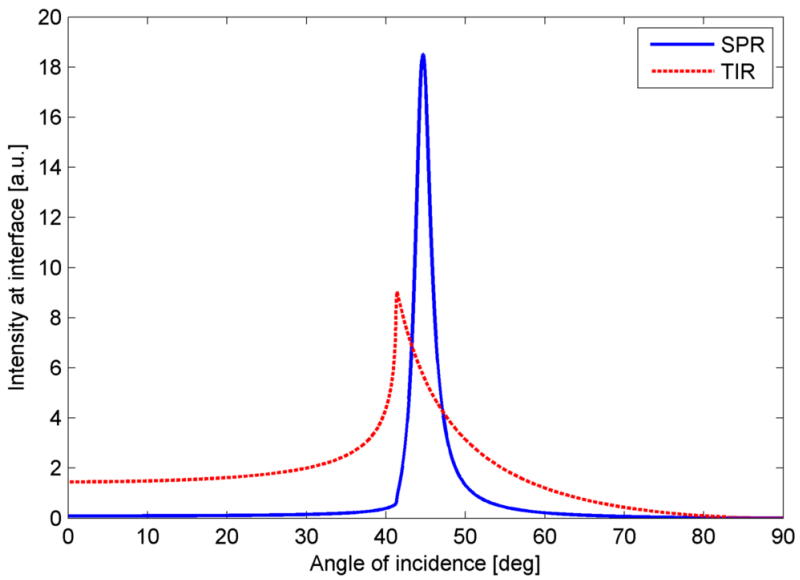

Figure 2-1. Comparison of intensity enhancement at the interface between TIR (dashed line) and SPR (solid line).

Calander, et al. 2006). One advantage of SPCE in exciting fluorescent molecules is that the evanescent field strength is typically stronger than normal TIRF at the surface plasmon resonance angle, where reflectivity is minimum and photons are efficiently coupled to the plasmons. For example, Figure 2-1 compares the intensity enhancement at the metal interface for TIR and SPR excitation, assuming that gold is used and that the incident beam is *p*-polarized. The excitation wavelength is assumed to be 532 nm, giving rise to a surface plasmon resonance angle of about 45 degrees. At this SPR angle, the enhancement is more than three times that of the TIR excitation with the same excitation angle. This implies that for the same excitation power, SPCE gives rise to more efficient excitation of the fluorescent molecules than TIRF. Other advantages of SPCE include small detection volume leading to less background signal, and reduction in photobleaching due to decreased fluorescence lifetime (Chance et al. 1974; Drexhage 1970; Z. Gryczynski et al. 2006; Lukosz and Kuhn 1977; Vasilev et al. 2004).

Apart from spectroscopic uses, SPCE can be used for 2D imaging by employing an objective-launched microscope set-up as shown in Figure 2-2. In this configuration, the sample is deposited on a cover slip coated with a thin layer of metal such as gold which is commonly used as the metal layer due to its biocompatibility with cells and tissues. This is then placed over a high numerical aperture (NA) TIRF objective lens. Light from the excitation laser is focused at the back-focal plane of the objective and is emitted as a plane wave at an angle to the substrate. By positioning the beam such that the incident angle is at the surface plasmon resonance angle, a strong evanescent plasmon field is set up to excite the fluorophores in the sample. The

fluorescence emission is then outcoupled through via surface plasmons and is collected by the same high NA objective lens. The image is finally captured by a CCD camera via an imaging lens. This microscopy method is termed surface plasmon-coupled emission microscopy (SPCEM) and recently has been used to image muscle fibrils (Borejdo, Gryczynski, et al. 2006; Burghardt et al. 2006). An advantage of using SPCEM for surface imaging is the increased excitation efficiency due to the plasmon enhanced electric field at the dielectric interface. Another advantage is the thinner detection volume, which is a result of the distance-dependent coupling of fluorophores to surface plasmons, and improved background rejection, both of which give rise to a better signal-to-noise ratio and higher image contrast (Z. Gryczynski et al. 2006). In addition, another advantage is that the set-up allows simultaneous imaging of the fluorescence emission and measurement of the cell-substrate contacts at the same time (Giebel et al. 1999). This information can also be used to quantify

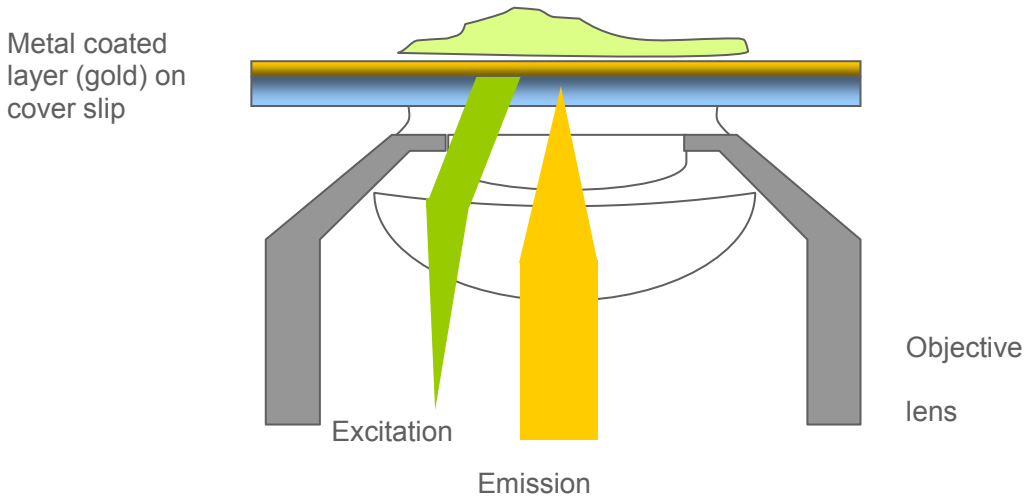

Figure 2-2. An objective-launched set-up for SPCE imaging.

ligand-receptor interactions. However, SPCEM has not been fully understood in terms of its emission out-coupling characteristics and one distinct disadvantage is that it makes multi-modal imaging with phase or DIC methods difficult. More importantly, imaging characteristics of the set-up have not been fully described to-date. In the subsequent sections, the full SPCEM imaging model and its point spread function is derived based on an angular spectrum representation. This model provides a foundation for understanding the imaging characteristics of SPCEM and is important for quantitative or point spread function engineering applications.

2.2 Description of Angular Spectrum Representation

Briefly, the angular spectrum of plane waves is a method based on an integral representation that is useful for studying the properties of wave fields. In many wave-propagation problems, the analysis of diffraction at an aperture typically deals with wave fields in a half space and can be represented in the form (Born and Wolf 1999)

$$U(x,y,z) = \iint_{-\infty}^{\infty} a(p,q)\mathrm{e}^{ik_0(px+qy+mz)}\mathrm{d}p\mathrm{d}q, \tag{2.1}$$

where

$$m = \begin{cases} \left(1-p^2-q^2\right)^{1/2} & \text{when } p^2+q^2 \le 1 \\ i\left(p^2+q^2-1\right) & \text{when } p^2+q^2 > 1 \end{cases} \tag{2.2}$$

for $z \ge 0$. In addition, for dealing with the angular spectrum representation of a point source in free space, the Weyl representation was derived (Weyl 1919) and is given by

$$U(x,y,z)=\frac{ik_0}{2\pi}\iint_{-\infty}^{\infty}\frac{1}{m}\mathrm{e}^{ik_0(px+qy+m|z|)}\mathrm{d}p\mathrm{d}q, \tag{2.3}$$

where this representation encompasses both homogenous and inhomogenous waves. It is noted that the above representations are in scalar terms. The angular spectrum can be generalized for the vector case and can be used to obtain an expression for the radiation of a dipole which is then used to derive a model for SPCEM.

2.3 A Model for SPCEM

To understand the point spread function characteristics of SPCEM, a theoretical model can be developed by considering a fluorescent molecule placed on the gold-coated cover slip which is then imaged by the CCD camera. The molecule is treated as a point dipole that is excited by the incident light which then radiates at the emission wavelength; the angular spectrum of an emitting dipole can be determined. The model is constructed in two steps. First, the excitation of the dipole in the object space by a *p*-polarized plane wave is considered. Then, the dipole emission and the subsequent propagation of the emission light through a 4f microscope system is modeled. Finally, the intensity point spread function in the image space can be calculated. These steps are shown in the following sections.

2.3.1 Excitation of dipole in the object space

In SPCEM, dipoles on the metal-coated glass slide are excited by a *p*-polarized incident plane wave as shown in Figure 2-3. n_1 denotes the refractive index of the object space, n_2 is the refractive index of the metal layer and n_3 is the refractive index

of the glass slide and immersion medium. The dipole is placed at a distance d from the metal surface. $k_{3,inc}$ is the wave number of the incident plane wave in medium 3 intersecting the interface at an angle of θ_i from the surface normal, and is given as $k_{3,inc} = 2\pi n_3 / \lambda_{inc}$, where λ_{inc} is the wavelength of the incident light in free space.

As shown in the figure, the optical system used in SPCEM to excite the fluorophores by surface plasmons is similar to a TIRF microscope (D. Axelrod 2003). The excitation field $\mathbf{E_i}$ of SPCEM is simply given by

$$\begin{aligned}\mathbf{E_i} = -\frac{n_3}{n_1}\tau_{p,inc}(i\sqrt{sin^2\theta_i - (n_1/n_3)^2}\,\mathbf{e_x} + \sin\theta_i \mathbf{e_z}) \\ \times \exp(ik_{3,inc}x\sin\theta_i)\exp(k_{3,inc}z\sqrt{sin^2\theta_i - (n_1/n_3)^2})\end{aligned} \tag{2.4}$$

where $\mathbf{e_x}$ and $\mathbf{e_z}$ denote the unit vectors in the x and z directions, and $\tau_{p,inc}$ is the three-layer Fresnel coefficient (Raether 1988) for p-polarized light given by

$$\tau_{p,inc} = \frac{t_p^{32} t_p^{21} \exp(ik_2 t\cos\theta_2)}{1 + r_p^{32} r_p^{21} \exp(2ik_2 t\cos\theta_2)} \tag{2.5}$$

where t_p^{32} and t_p^{12} are the Fresnel coefficients for each of the respective two-layer interfaces, θ_2 is the angle in the metal layer given by Snell's law and t is the thickness of the metal layer.

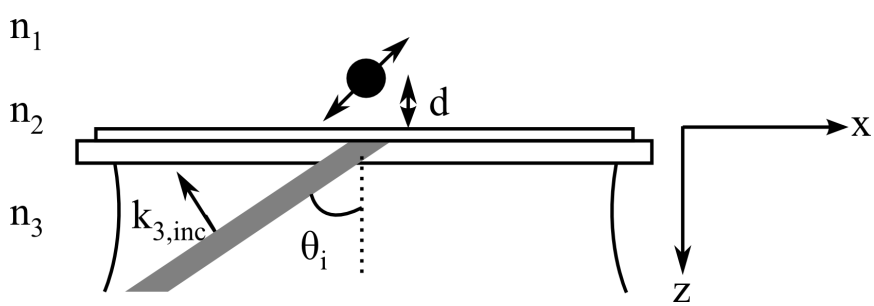

Figure 2-3. Excitation of dipole by a p-polarized incident plane wave.

2.3.2 Electric field in the image space

Figure 2-4 shows the typical set-up of a 4f system for SPCEM imaging. The point dipole $\mathbf{p} = \vec{\mu}\exp(i\omega t)$ at a distance d away from the first interface is excited by the field calculated in Equation (2.4) and emits light at a different wavelength λ from the excitation wavelength λ_{inc}. Region 2 is a thin metal layer of thickness t with an index of refraction n_2. A high NA objective is placed in medium 3 and the tube lens in medium 4.

Due to the highly polarized emission of SPCE and the high NA objective used, a full vectorial formulation is derived for the model shown in Figure 2-4, since a scalar treatment of the model does not take into account these effects and is inadequate. Using the vectorial Debye integral of Richards and Wolf (Richards and Wolf 1959; Wolf 1959), the field in the image space of the tube lens is given by

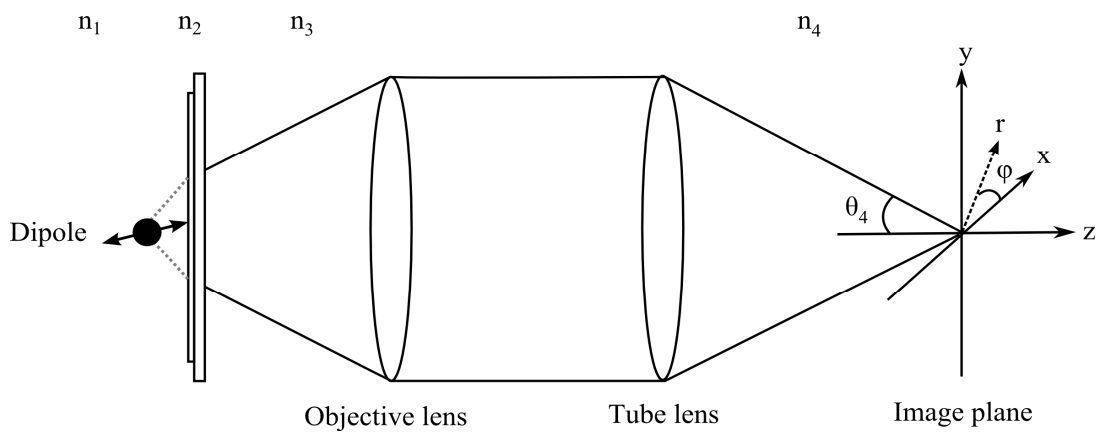

Figure 2-4. A schematic view of the SPCEM imaging process within a 4f optical system.

$$\mathbf{E}_4(r,\varphi,z) = -\frac{ik_4}{2\pi}\int\int_\Omega \mathbf{E}_4' \sin\theta_4 \exp(ik_4 r \sin\theta_4 \cos(\phi-\varphi)) \times \exp(ik_4 z\cos\theta_4)\exp(i\Phi)\mathrm{d}\theta_4\mathrm{d}\phi \tag{2.6}$$

where the coordinates of a point in the image space are given by (r,φ,z), k_4 is the wave number in medium 4, θ_4 is the polar angle of the wave vector in medium 4 and ϕ is the azimuthal angle of the wave vector. It is assumed that as the wave propagates through the lenses, the meridional plane of the propagation remains constant. Φ denotes the wave front aberration function which is a measure of the path difference between the wave front at the exit aperture of the tube lens and the wave front of an ideal spherical wave (Wolf 1959).

To obtain the electric strength vector $\mathbf{E}_4'$ in Equation (2.6), we first obtain the field emitted by the dipole in medium 1 which is subsequently transmitted into medium 3, and then propagated through the 4f system into medium 4. When considering SPCEM, it is important to note that the fluorophores are close to the

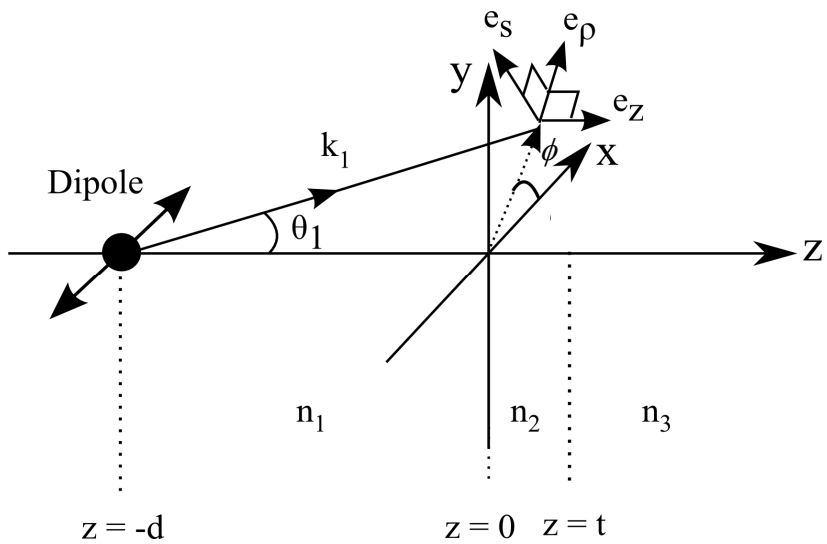

Figure 2-5. Axis convention used in the derivation of the field in medium 3.

metal surface, in the order of nanometers scale, which implies that the near-field emission cannot be ignored. The procedure to obtain the field in medium 3 given below follows in part that given by Arnoldus and Foley (Arnoldus and Foley 2004) and takes into account the evanescent components. It is noted that the field in medium 3 had also been derived by Hellen and Axelrod (Hellen and Axelrod 1987) in a similar way.

Figure 2-5 shows the axis convention that is used for obtaining the expression for the dipole radiation in medium 3. The complex amplitude of the dipole source field in an infinite medium with index of refraction n_1 is given by the equivalent vectorial form of the Weyl expansion for a dipole (Ford and Weber 1984)

$$\mathbf{E_1}(\mathbf{r}) = -\frac{i}{2\pi n_1^2}\int \mathrm{d}^2\mathbf{k}_{\|}\frac{1}{k_0\nu_1}[k_1^2\mathbf{p}-(\mathbf{p}\cdot\mathbf{k_1})\mathbf{k_1}]\exp[i\mathbf{k_1}\cdot(\mathbf{r}+d\mathbf{e_z})] \tag{2.7}$$

where $\nu_i = (n_i^2 - \alpha^2)^{1/2}$ and $\alpha = k_{\|}/k_0$, and

$$\mathbf{k_1} = \begin{cases} \mathbf{k}_{\|} + k_0\nu_1\mathbf{e_z} & \text{for } z > -d \\ \mathbf{k}_{\|} - k_0\nu_1\mathbf{e_z} & \text{for } z < -d \end{cases}$$

where $\mathbf{k}_{\|}$ denotes the surface wave vector. In Equation (2.7), the field in medium 1 is effectively represented by an angular spectrum of plane waves, where the limits of integration take into consideration both evanescent waves and travelling waves.

To obtain the field in medium 3, it is then necessary to decompose plane waves which are propagating in the positive z direction into their p and s components, so that it is possible to make use of the Fresnel transmission coefficient for the three-layer system. First, the unit vectors for a cylindrical coordinate system whose radial

and axial components are contained in both the plane of incidence of a particular plane wave and the meridional plane as the waves propagates through the system are

$$\mathbf{e}_\rho = \mathbf{k}_\parallel / k_\parallel, \quad \mathbf{e_s} = \mathbf{e_z} \times \mathbf{e}_\rho, \quad \mathbf{e_z} = \mathbf{e}_\rho \times \mathbf{e_s} \tag{2.8}$$

Then, the unit vector for the p component in medium 1 and medium 3 are,

$$\mathbf{e_{1,p}} = \frac{\mathbf{k_1}}{k_1} \times \mathbf{e_s}, \quad \mathbf{e_{3,p}} = \frac{\mathbf{k_3}}{k_3} \times \mathbf{e_s} \tag{2.9}$$

respectively, and $\mathbf{k_3}$ is the wave vector of the transmitted waves in medium 3 given by $\mathbf{k_3} = \mathbf{k}_\parallel + k_0 \nu_3 \mathbf{e_z}$.

Decomposing the plane waves in Equation (2.7) into their p and s components and using the Fresnel transmission coefficient for the three-layer system, the complex amplitude of the field in medium 3 ($z > t$) can be expressed in terms of these unit vectors and thus

$$\mathbf{E_3}(\mathbf{r}) = -\frac{ik_0}{2\pi} \int \mathrm{d}^2\mathbf{k}_\parallel \frac{1}{\nu_1} \mathbf{E}_3^{'} \exp[i\mathbf{k_3} \cdot (\mathbf{r} - t\mathbf{e_z})] \exp(ik_0 \nu_1 d), \tag{2.10}$$

where

$$\mathbf{E}_3^{'} = \begin{bmatrix} E_{3,\rho}^{'} \\ E_{3,s}^{'} \\ E_{3,z}^{'} \end{bmatrix} = \begin{bmatrix} \frac{-\nu_3}{n_1 n_3} \tau_p (-\nu_1 \mathbf{p} \cdot \mathbf{e}_\rho + \alpha \mathbf{p} \cdot \mathbf{e_z}) \\ \tau_s \mathbf{p} \cdot \mathbf{e_s} \\ \frac{\alpha}{n_1 n_3} \tau_p (-\nu_1 \mathbf{p} \cdot \mathbf{e}_\rho + \alpha \mathbf{p} \cdot \mathbf{e_z}) \end{bmatrix} \tag{2.11}$$

denotes the electric field strength vector of the plane waves in medium 3 and the Fresnel transmission coefficients have a similar form to Equation (2.5)

$$\tau_q = \frac{t_q^{12} t_q^{23} \exp(ik_2 t \cos\theta_2)}{1 + r_q^{12} r_q^{23} \exp(2ik_2 t \cos\theta_2)}, \quad q = p, s. \tag{2.12}$$

Equation (2.10) describes the field in medium 3 due to the radiating dipole in medium 1. As the waves propagate to the objective lens, the wave front aberration function that is incident at the entrance pupil of the objective lens relative to its Gaussian focus can be obtained as

$$\Phi = k_0 \nu_1 d - k_0 \nu_3 (d + t). \tag{2.13}$$

Next, in order to propagate these plane waves to medium 4, it is necessary to make use of the generalized Jones matrix which was introduced by Török *et al* (Török et al. 1998; Török and Sheppard 2002; Török and Varga 1997) to express $\mathbf{E}_4^{'}$ in terms of $\mathbf{E}_3^{'}$. It is noted that the reflection and transmission coefficients of the lenses are not taken into account as they are irrelevant here and complicate the equations unnecessarily. Hence,

$$\mathbf{E}_4^{'} = \begin{bmatrix} E_{4,r}^{'} \\ E_{4,\varphi}^{'} \\ E_{4,z}^{'} \end{bmatrix} = A(\theta_3, \theta_4)\mathbf{M}\mathbf{L}_4\mathbf{L}_3\mathbf{E}_3^{'}, \tag{2.14}$$

where $A(\theta_3, \theta_4)$ is the apodization factor for a system that satisfies Abbe's sine condition (Richards and Wolf 1959), and is given by

$$A(\theta_3, \theta_4) = \sqrt{\frac{\cos\theta_4}{\cos\theta_3}}, \tag{2.15}$$

$\mathbf{L}_3$ and $\mathbf{L}_4$ is a rotation matrix that rotates about the axis defined by $\mathbf{e}_s$,

$$\mathbf{L}_n = \begin{bmatrix} \cos\theta_n & 0 & -\sin\theta_n \\ 0 & 1 & 0 \\ \sin\theta_n & 0 & \cos\theta_n \end{bmatrix}, \tag{2.16}$$

and $\mathbf{M}$ is a transformation matrix that transforms the (ρ, s, z) coordinate system to the (r, φ, z) coordinate system, and is given by

$$\mathbf{M} = \begin{bmatrix} \cos(\varphi-\phi) & \sin(\varphi-\phi) & 0 \\ -\sin(\varphi-\phi) & \cos(\varphi-\phi) & 0 \\ 0 & 0 & 1 \end{bmatrix}, \tag{2.17}$$

where φ is the azimuthal observation angle and ϕ is the azimuthal angle of the wave vector.

Finally, substituting Equation (2.14) into Equation (2.6), and replacing the dipole orientation vector $\mathbf{p}$ with $(\mu \sin\theta_d \cos\phi_d, \mu \sin\theta_d \sin\phi_d, \mu\cos\theta_d)$, thus

$$\mathbf{E_4}(r,\varphi,z) = \begin{bmatrix} E_{4,r} \\ E_{4,\varphi} \\ E_{4,z} \end{bmatrix},$$

with

$$\begin{aligned} E_{4,r} &= -\frac{ik_4}{2}\{\mu\sin\theta_d\cos(\phi_d-\varphi)[K_0^I + K_2^I] - \mu\cos\theta_d[2iK_1^I]\} \\ E_{4,\varphi} &= -\frac{ik_4}{2}\{\mu\sin\theta_d\sin(\phi_d-\varphi)[K_0^I - K_2^I]\} \\ E_{4,z} &= -\frac{ik_4}{2}\{\mu\sin\theta_d\cos(\phi_d-\varphi)[2iK_1^{II}] - \mu\cos\theta_d[2K_0^{II}]\} \end{aligned} \tag{2.18}$$

where

$$\begin{aligned} K_0^I &= \int_0^\sigma \sqrt{\frac{\cos\theta_4}{\cos\theta_3}}\sin\theta_4(\tau_s + \tau_p\cos\theta_1\cos\theta_4)J_0(k_4 r\sin\theta_4) \\ &\quad \times \exp(ik_4 z\cos\theta_4)\exp(i\Phi)\mathrm{d}\theta_4 \\ K_1^I &= \int_0^\sigma \sqrt{\frac{\cos\theta_4}{\cos\theta_3}}\sin\theta_4\tau_p\sin\theta_1\cos\theta_4 J_1(k_4 r\sin\theta_4) \\ &\quad \times \exp(ik_4 z\cos\theta_4)\exp(i\Phi)\mathrm{d}\theta_4 \end{aligned}$$

$$
\begin{aligned}
K_2^I &= \int_0^\sigma \sqrt{\frac{\cos\theta_4}{\cos\theta_3}} \sin\theta_4 (\tau_s - \tau_p \cos\theta_1 \cos\theta_4) J_2(k_4 r \sin\theta_4) \\
&\quad \times \exp(ik_4 z \cos\theta_4) \exp(i\Phi) \mathrm{d}\theta_4 \\
K_0^{II} &= \int_0^\sigma \sqrt{\frac{\cos\theta_4}{\cos\theta_3}} \sin\theta_4 \tau_p \sin\theta_1 \sin\theta_4 J_0(k_4 r \sin\theta_4) \\
&\quad \times \exp(ik_4 z \cos\theta_4) \exp(i\Phi) \mathrm{d}\theta_4 \\
K_1^{II} &= \int_0^\sigma \sqrt{\frac{\cos\theta_4}{\cos\theta_3}} \sin\theta_4 \tau_p \cos\theta_1 \sin\theta_4 J_1(k_4 r \sin\theta_4) \\
&\quad \times \exp(ik_4 z \cos\theta_4) \exp(i\Phi) \mathrm{d}\theta_4
\end{aligned}
\tag{2.19}
$$

and $J_n(\bullet)$ denotes the Bessel function of the first kind of order n. The wave front aberration function Φ is given in Equation (2.13). The collection semi-angle σ is obtained by using the sine condition for an aplanatic system

$$
\frac{\text{NA of objective}}{n_4 \sin\sigma} = mag,
$$

where *mag* is the overall magnification of the 4f system.

Equations (2.18) and (2.19) describe the electric field in the image space (see Figure 2-4). It is interesting to see that these expressions resemble the expressions derived by Török *et al* (Török et al. 1998; Török and Varga 1997) which are for the case of imaging a dielectric scatterer in a 4f system placed in a homogenous medium. The main difference for these expressions is the presence of the Fresnel transmission coefficients as well as the non-zero wave aberration function that is caused by the refractive index mismatch as the dipole waves traverse across the metal interface. In fact, if the dipole is placed at the origin and the metal interface is removed by setting d and t to zero, and setting n_3 to be equal to n_4, the expressions in Equations (2.18)

and (2.19) reduce to the same form as the expressions in (Török et al. 1998; Török and Varga 1997).

2.3.3 Addition of a linear polarizer in the detection path

For the purpose of verification of the model by comparison of the simulation results to the experimental results, linear polarizers can be added to the model. This is done for example by placing them between the objective lens and the tube lens and can be accomplished by modifying Equation (2.14) into

$$\mathbf{E}_4' = A(\theta_3, \theta_4)\mathbf{M}\mathbf{L}_4\mathbf{R}^{-1}\mathbf{P}\mathbf{R}\mathbf{L}_3\mathbf{E}_3', \tag{2.20}$$

where

$$\mathbf{R} = \begin{bmatrix} \cos\phi & -\sin\phi & 0 \\ \sin\phi & \cos\phi & 0 \\ 0 & 0 & 1 \end{bmatrix} \tag{2.21}$$

transforms from the (ρ, s, z) coordinate system into cartesian coordinates, and $\mathbf{P}$ is the polarization matrix. For a linear polarizer in the x and y directions, their polarization matrices are given respectively by

$$\mathbf{P}_\mathbf{x} = \begin{bmatrix} 1 & 0 & 0 \\ 0 & 0 & 0 \\ 0 & 0 & 1 \end{bmatrix}, \quad \mathbf{P}_\mathbf{y} = \begin{bmatrix} 0 & 0 & 0 \\ 0 & 1 & 0 \\ 0 & 0 & 1 \end{bmatrix}. \tag{2.22}$$

For both of these cases, the expressions for the field and intensity in the image space are derived by first substituting Equation (2.20) into Equation (2.6), and then simplifying the results. This process is similar to the derivation of Equations (2.18), (2.19), (2.23), (2.26) above. It is of interest to note that other types of optical elements can also be inserted in between the objective lens and tube lens.

2.3.4 Intensity in image space

The intensity that is detected in the image space is given by

$$I \propto (|E_{4,r}|^2 + |E_{4,\varphi}|^2 + |E_{4,z}|^2)/P_T \tag{2.23}$$

where the normalization factor P_T is the total power emitted by the dipole in the presence of a metal interface (Enderlein and Bohmer 2003; Hellen and Axelrod 1987). For a dipole which is perpendicularly oriented to the metal interface, $\theta_d = 0^\circ$, the intensity is rotationally symmetric

$$I_\perp \propto 4(|K_1^I|^2 + |K_0^{II}|^2)/P_T. \tag{2.24}$$

On the other hand, the image of a dipole which has an orientation parallel to the metal interface along the x direction is not rotationally symmetric, that is, it has a dependency on φ

$$I_\parallel \propto (|K_0^I|^2 + |K_2^I|^2 + 4\cos^2\varphi\,|K_1^{II}|^2 + 2\cos 2\varphi \mathrm{Re}[K_0^I K_2^{I*}])/P_T. \tag{2.25}$$

In practice, since an ensemble of fluorophores is imaged in a given sample, it is more meaningful to find an expression for the average intensity distribution for an ensemble of dipole orientations. Consider that the dipole that is excited by the full incident field and the electric dipole moment of the emission is randomly oriented, since the fluorophore can assume many different orientations during its emission lifetime, Equation (2.23) is integrated over all polar and azimuthal angles, and thus the intensity in the image space is given by

$$I_{PSF} \propto \int_0^\pi \int_0^{2\pi} |\mathbf{E_i}|^2\, I \sin\theta_d \mathrm{d}\phi_d \mathrm{d}\theta_d. \tag{2.26}$$

I_{PSF} corresponds to the case where the dipole rotates and aligns with the incident field and gets excited by the full incident field. The emission dipole moment, however, is uniformly distributed over all polar and azimuthal angles because the dipole may rotate arbitrarily during emission.

In the next chapter, these expressions which are derived for the SPCEM model are used to simulate the point spread function characteristics. The simulations are then compared with experimental results to verify the validity of this model.

CHAPTER 3: EXPERIMENTAL RESULTS OF SPCEM

In an imaging system, the point spread function defines the response of the system to a point object, or as its name implies, the definition of how the image of a point "spreads" out and what it looks like. This is important because under the condition of linear spatial invariance, a more complex object can be considered as a sum of many point objects. Therefore if the point spread function of a system is known, then it is possible to determine the image of the object by composing it in terms of the image of each individual point. This idea is expressed more concisely in mathematical terms as the convolution operation

$$i(x, y) = \int\int o(x', y')h(x - x', y - y')\mathrm{d}x'\mathrm{d}y', \tag{3.1}$$

where o is the object, h denotes the system point spread function, and i is the final image. Based on the model developed in the previous chapter, the characteristics of SPCEM are elucidated in this chapter. The point spread function characteristics are also described and compared with experimental results.

3.1 Simulation Parameters

Equations in chapter two are evaluated numerically with values chosen to reflect the experimental conditions. For the excitation beam, the wavelength of 532 nm corresponds to the solid state CW green laser that is used to excite surface plasmons. Gold, which has a complex refractive index of $0.32 + 2.83i$ (Palik 1997), is used as the metal layer which is coated on a glass cover slip. Apart from the wavelength and the requirement of *p*-polarization, the excitation of surface plasmons is also dependent on the thickness of the metal layer as well as the angle of incidence. For our configuration, Figure 3-1 presents the reflectivity at the interface as a function of these two variables in the form of a contour plot while Figure 3-2 shows a sampling of a family of reflectivity curves with different metal thickness. The surface plasmon

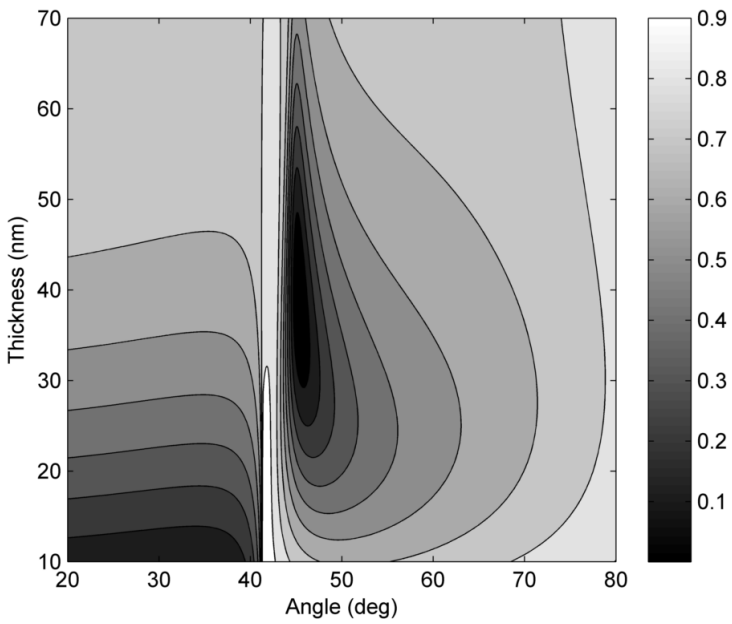

Figure 3-1. Contour plot of reflectivity with respect to thickness of gold layer and angle of incidence of excitation light.

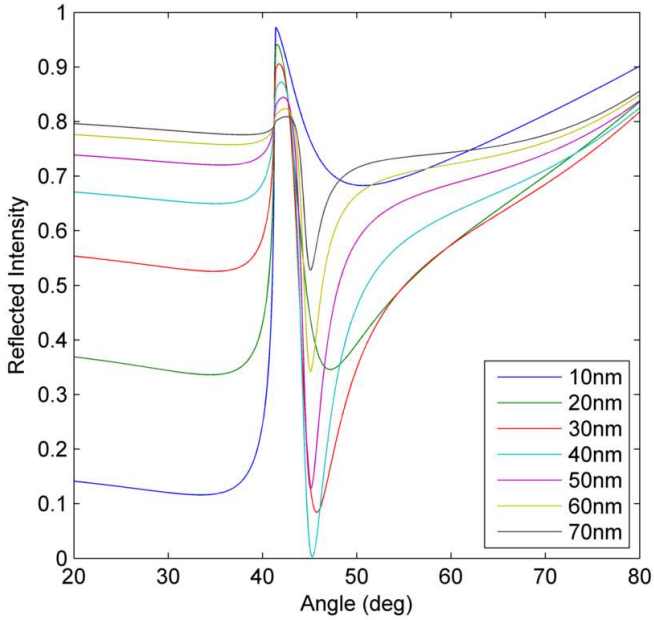

Figure 3-2. Family of reflectivity curves for different thickness of metal layer as a function of the angle of incidence of excitation light. The thickness ranges from 10nm to 70nm in steps of 10nm. Surface plasmon resonance occurs for a thickness of 40nm and an incident angle of 45 degrees for gold at the incident wavelength.

resonance effect corresponds to the lowest reflectivity obtained from the plots. This can be obtained either by sampling a grid and reading off the minimum or by using a gradient descent type optimization method. From the plots, the surface plasmon resonance effect can be achieved with a gold interface layer of 40 nm and an incident angle (surface plasmon resonance angle) of 45° with the incident wavelength of 532nm. The incident light that is coupled into surface plasmons excites the dipole and results in emission at a wavelength of 560 nm. The emitted light is collected by a high NA objective with NA1.45 and 60X magnification. Table 3-1 shows the values used for the simulation. These values were chosen to match the actual experimental conditions as described.

Table 3-1. Values used for numerical simulation.

Symbol	Value
λ_{inc}	532 nm
λ	560 nm
n_1	1
n_2	0.32+2.83i
n_3	1.515
n_4	1
d	20 nm
t	40 nm
NA	1.45
mag	60X
θ_i	45º

3.2 Radiation Characteristics of SPCEM

3.2.1 *P*-polarized emission and fluorescence quenching

The presence of a thin gold layer coated on the glass cover slip changes the radiation characteristics of a fluorescent molecule placed on top of the layer. Firstly, a dipole that is placed on the metal radiates mainly in a directional manner as shown in Figure 3-3, which plots the emitted intensity as a function of the polar observation angle based on Equation (2.10). Secondly, due to coupling to surface plasmons, the radiation through the metal layer is predominantly *p*-polarized with respect to the

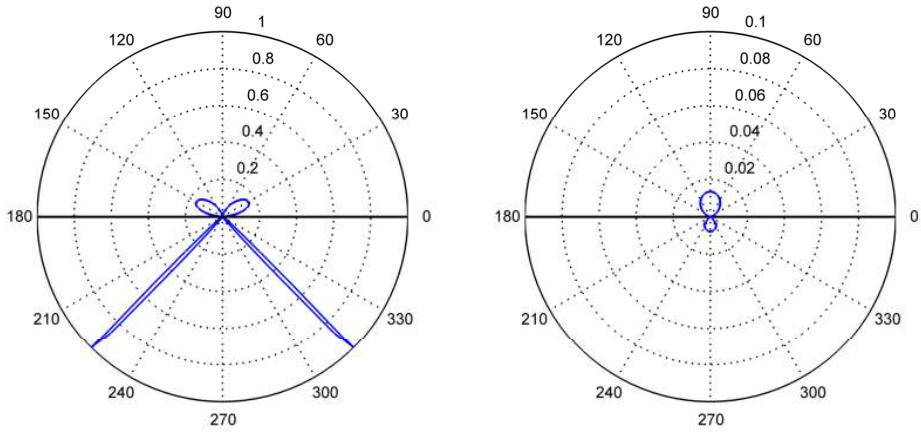

Figure 3-3. Polar plot of the emission intensity of SPCEM as a function of observation angle shows that the radiation is highly directional. Plots are normalized to the peak intensity of *p*-polarized emission. Left: *p*-polarized emission, Right: *s*-polarized emission.

transverse interface layer; approximately 98% of the radiation is *p*-polarized while the rest is *s*-polarized. As can be seen in the figure, the forward emission of the *p*-polarized light has a peak intensity that is more than 70 times stronger than the *s*-polarized emission. The peak occurs at about 45 degrees corresponding to the surface plasmon resonance angle. Another important characteristic of a fluorescent molecule on metal is the distance dependent coupling between the radiation and the metal layer. Generally, when a fluorophore molecule is excited to a higher energy state via absorption of photons, it can relax to the ground state through radiative or non-radiative transitions. Under normal conditions when the relaxation is through the radiative channel, longer wavelength photons are emitted and this is known as Stokes shift. However in SPCEM, if the fluorescent molecule is close to the metal surface, it encounters quenching where the relaxation of the molecule to the ground state is due

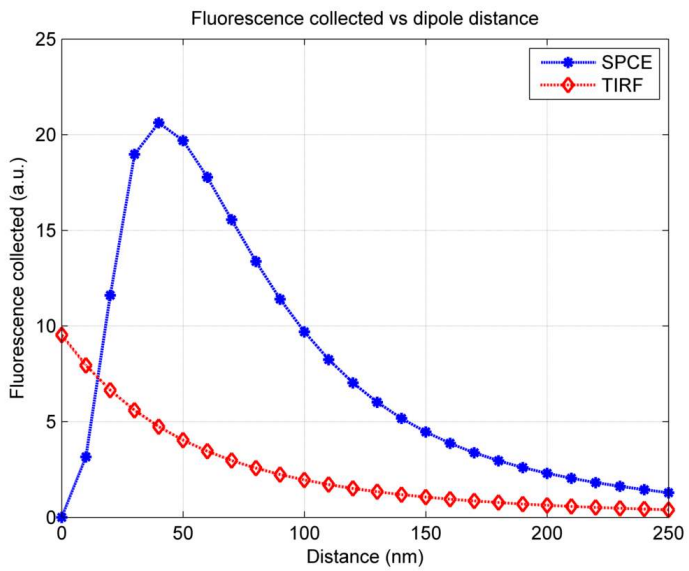

Figure 3-4. Plot of fluorescence collected by objective lens as a function of the dipole distance from the interface for SPCE and TIRF.

to non-radiative decay. The quenching effect can be seen in Figure 3-4 which compares the fluorescence collected by an objective lens for an oscillating dipole placed at various distances away from the substrate. The plot is calculated by integrating Equation (2.10) over the objective numerical aperture. In the figure, it is seen that quenching is prominent for distances less than 10 nm from the surface and becomes less of a problem when the dipole is placed more than 20 nm away from the surface where the fluorescence energy collected exceeds 75% of the peak energy. A result of quenching is that the lifetime of fluorophores becomes reduced leading to less photobleaching which is advantageous for bioimaging (Amos and Barnes 1997; Drexhage 1970; Lakowicz 2005).

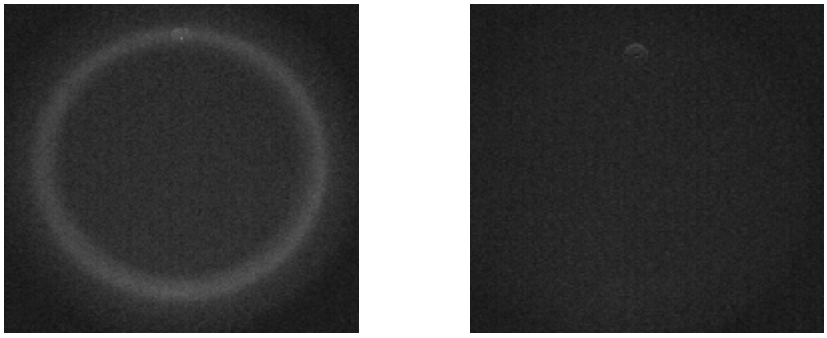

Figure 3-5. Comparison of back-focal plane emission pattern of SPCEM for *p*-polarized (left) and *s*-polarized (right) incident light at the surface plasmon resonance angle.

3.2.2 Back-focal plane image of SPCEM

The directional nature of the radiation pattern of SPCEM can be observed by capturing the fluorescence emission at the back-focal plane of the objective. Figure 3-5 shows the experimental back-focal plane images of a fluorescent bead for *p*-polarized as well as for *s*-polarized incident light. It is observed that with the *s*-polarized incident light, the image does not display any observable pattern, which is in line with the known fact that surface plasmons are not excited by *s*-polarized light (the bright spot near the top of the image is due to reflection of the fibre tip). On the other hand, excitation of surface plasmons with *p*-polarized light is possible and this leads to an observable ring which shows the directional emission pattern of SPCEM as shown in the left panel of Figure 3-5.

3.3 Point Spread Function Characteristics of SPCEM

3.3.1 Electric field distributions

In order to understand the imaging characteristics of SPCEM, it is also important to study the point spread function characteristics of the set-up. From the model derived in the previous chapter, the electric field distribution and the intensity point spread function of SPCEM can be calculated based on the simulation parameters defined in Section 3.1.

Figure 3-6 shows the distribution of the electric field components on the image plane for a dipole oriented perpendicular to the metal interface, while Figure 3-7 shows the distribution for a dipole parallel to the interface in the x direction. Comparing Figure 3-6(c) to Figure 3-6(a),(b) and Figure 3-7 (c) to Figure 3-7(a),(b) for both the perpendicular and parallel oriented dipoles, it can be seen that the E_z component of the field is negligible relative to the E_x and E_y components. This is a consequence of the low numerical aperture tube lens placed in the imaging system. Furthermore for a perpendicular dipole in Figure 3-6, there exists 90 degrees rotation symmetry in the distribution of the E_x and E_y field components. Furthermore, both of the components have the same peak amplitudes. Such a symmetry can be expected for a perpendicular dipole. In fact, one can easily visualize the effect where a dipole placed along the longitudinal axis results in axially symmetric field patterns, which will be radial in nature when projected onto the image plane.

For a dipole placed parallel to the metal interface and aligned in the x direction, the E_z component of the field is also negligible relative to the E_x and E_y components as seen in Figure 3-7. However, the lateral E_x component dominates over

the E_y component as expected for a dipole placed along the x direction. Furthermore unlike the perpendicular dipole, symmetry does not exist in this case between the E_x and E_y components. Comparing both of Figure 3-6 and Figure 3-7, it can also be seen that the field on the image plane due to a perpendicular dipole has peak field magnitude that is almost two times stronger than that of a parallel dipole.

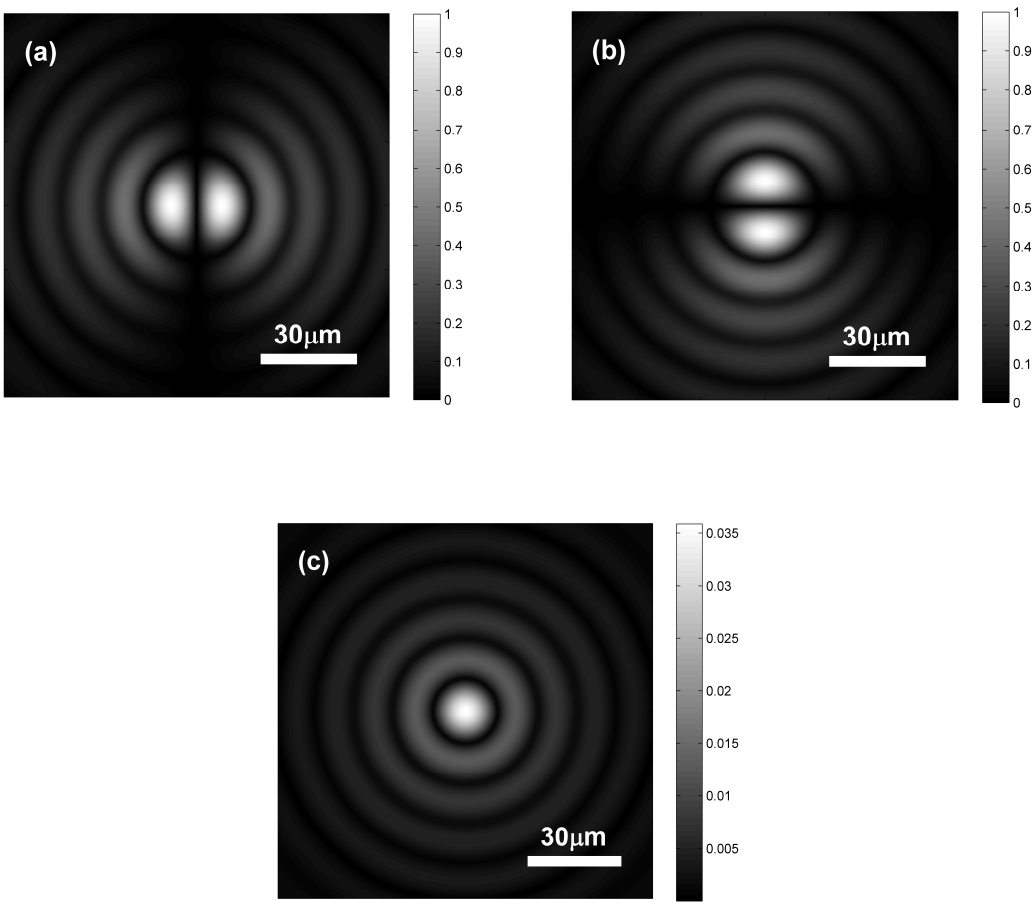

Figure 3-6. Absolute value of the electric field components on the image plane for a dipole which is oriented perpendicular to the metal interface. (a) E_x component (b) E_y component (c) E_z component

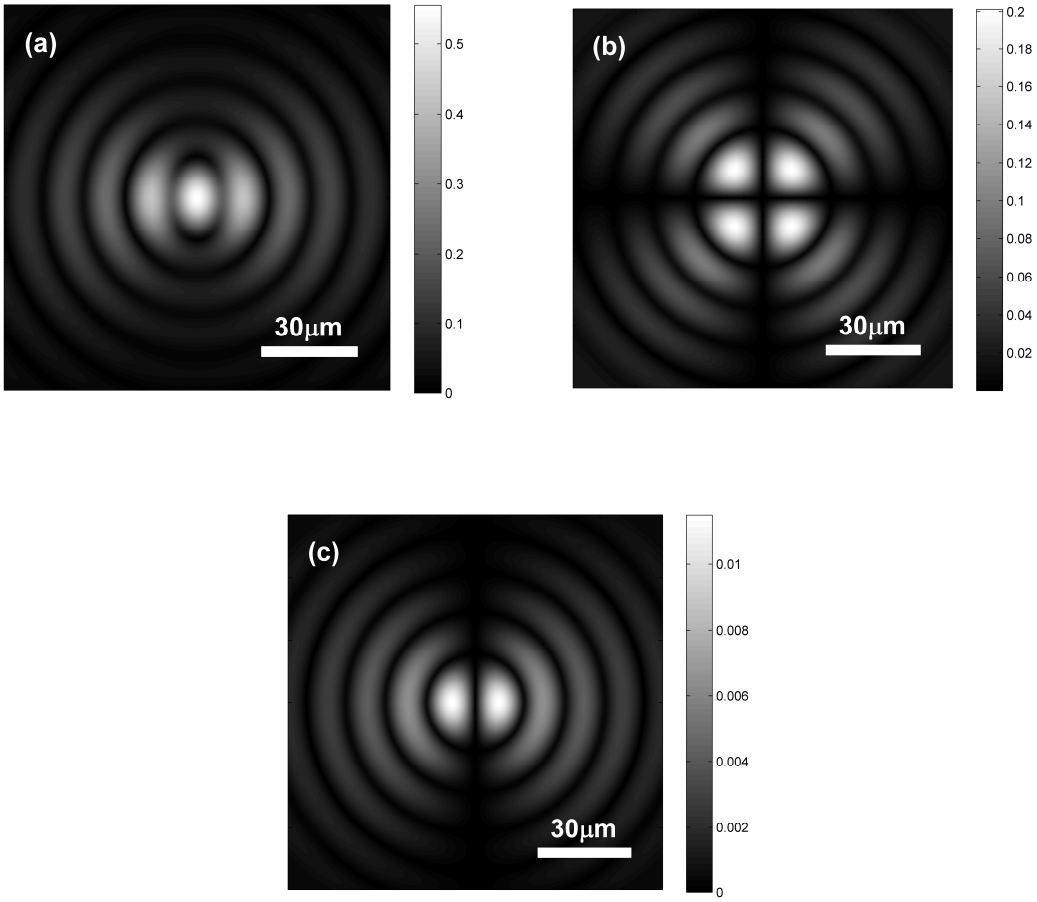

Figure 3-7. Absolute value of the electric field components on the image plane for a dipole which is oriented parallel to the metal interface in the x direction. (a) E_x component (b) E_y component (c) E_z component

3.3.2 Calculated intensity point spread function

The intensity point spread function of SPCEM is calculated and shown in Figure 3-8. It can be noted that the donut-shaped morphology observed in the image is distinctly different from the typical Airy-disk type point spread function of many imaging systems. In order to validate the model and the peculiar looking point spread function, it is thus necessary to obtain experimental data on the imaging system and to make a comparison between the theoretical data and the actual experimental data.

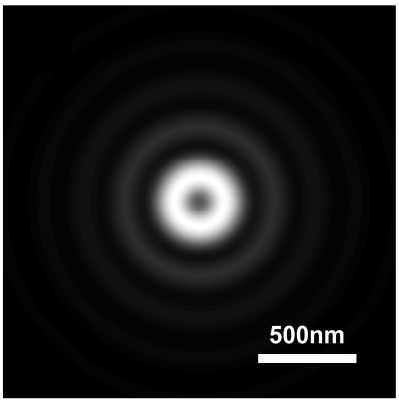

Figure 3-8. Intensity point spread function of SPCEM shows a donut-shaped morphology.

3.3.3 Experimental set-up of SPCEM

Experiments were carried out to obtain the experimental point spread function of SPCEM in order to compare with the theoretical results. Figure 3-9 shows the experimental set-up that was used. A continuous wave laser source with a wavelength of 532 nm (Verdi-10, Coherent) was used to excite subdiffraction-limited 40 nm

fluorescent beads (Molecular Probes, OR) that were placed on a cover slip coated with a 40 nm gold layer. The excitation angle was tuned to the surface plasmon resonance angle of 45º, so that the fluorescent beads were efficiently excited by the surface plasmons induced on the metal surface. A high NA objective lens (Olympus PlanApo NA1.45 60X) was used to collect the emission from the excited fluorophores with a peak emission wavelength of 560 nm. A barrier filter (HQ545LP, Chroma, Rockingham, VT) was used to block the scattered excitation light. The emission light exiting from the tube lens was then magnified 16 times and the image was captured on an intensified CCD (Pentamax, Princeton Instrument, Trenton, NJ). The same image was captured 10 times and averaged to reduce the background noise.

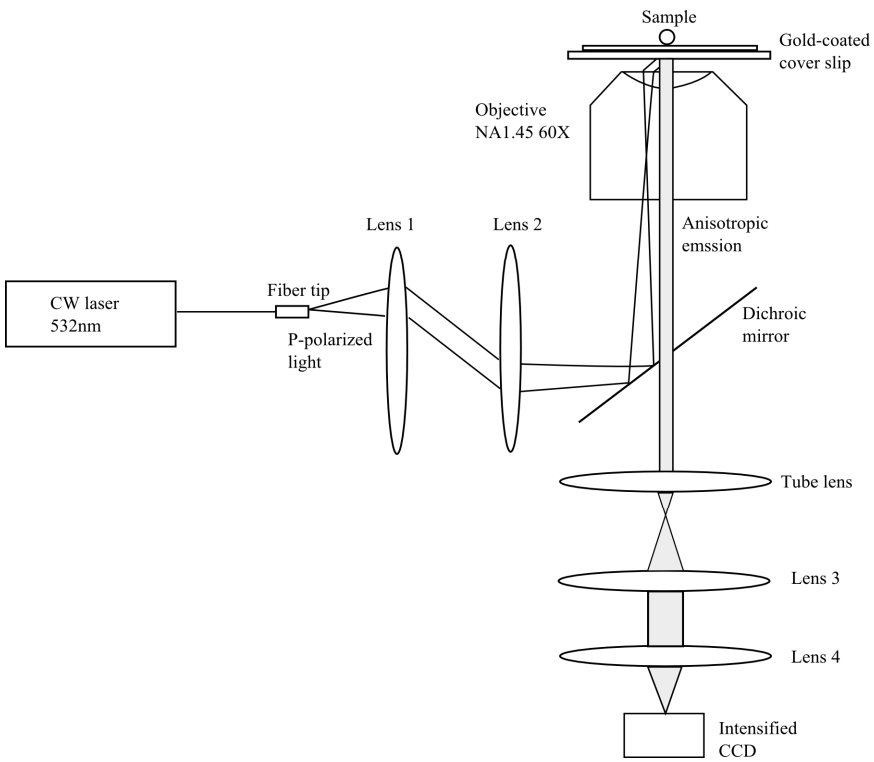

Figure 3-9. Experimental set-up used to obtain the point spread function of SPCEM by imaging fluorescent beads of diameter below the diffraction limit.

Figure 3-10(a) and Figure 3-10(b) compare the simulated images of the calculated point spread function of SPCEM with the actual point spread function obtained from the experiments. A comparison of the two figures shows a high degree of similarity between the calculated and the experimental point spread function in terms of their donut-shaped morphology. The figure also shows that the point spread function of SPCEM has a rotationally symmetric and annular-like characteristics, with multiple rings extending out with decreasing intensity. Interestingly, it has a "valley" near the center which is not seen in the point spread functions of conventional wide-field microscopy and confocal microscopy. It is also noted that the experimental image has rings which are slightly more spread out and wider than in the theoretical case. This is likely to be due to the fact that the fluorescent bead has a finite diameter, whereas in the theoretical model a point dipole was assumed.

To further validate the theoretical model, the experimental and theoretical results are also compared for the case when a linear polarizer was introduced into the system. Using the same experimental set-up as in Figure 3-9, a linear polarizer (LP-VIS100, Thorlabs) was added between lenses 3 and 4, and the image was captured on the intensified CCD. For the theoretical model, the polarizer was added between the objective lens and the tube lens. Figure 3-10(c) and Figure 3-10(d) show the theoretical and experimental point spread functions when a linear polarizer oriented in the y direction was added (the image for a x oriented linear polarizer is not shown since it is symmetrical to that of a y oriented linear polarizer). Both the theoretical and experimental point spread functions are similar in terms of their morphology. As in

the previous case, the experimental results show that the lobes are slightly wider than the theoretical results.

A more quantitative comparison is shown in Figure 3-11, which plots the cross-sectional profiles of the theoretical and experimental point spread functions. In Figure 3-11(a) where there is no linear polarizer added, the locations of the first peaks for both the theoretical and experimental results differ by approximately 20 nm, while the second peaks for the experimental point spread function are located further away from those of the calculated results by roughly 60 nm. The widths of the peaks for the experimental results are also wider than those of the theoretical results. In Figure 3-11(b) where a linear polarizer was added to the emission path, the first peaks for the experimental results are separated by 35 nm away from the first peaks of the calculated point spread function while their second peaks are located approximately 80 nm away. For both of the cases in Figure 3-11, these differences between the calculated and experimental point spread functions could be attributed to a few reasons. Firstly, as mentioned earlier, the actual beads have a finite diameter of 40 nm whereas the model assumed an infinitesimally small point dipole. Secondly, the effective numerical aperture of the high NA objective may actually be lower than its nominal value of NA 1.45 due to strong attenuation of the marginal rays. According to calculations for an effective numerical aperture of NA 1.2, the difference between the locations of the first peaks would differ by 15 nm and the second peaks by 30 nm, which is roughly a two-fold reduction in the errors. Other reasons for the differences could be due to aberrations of the relay optics and misalignment of the optical set-up.

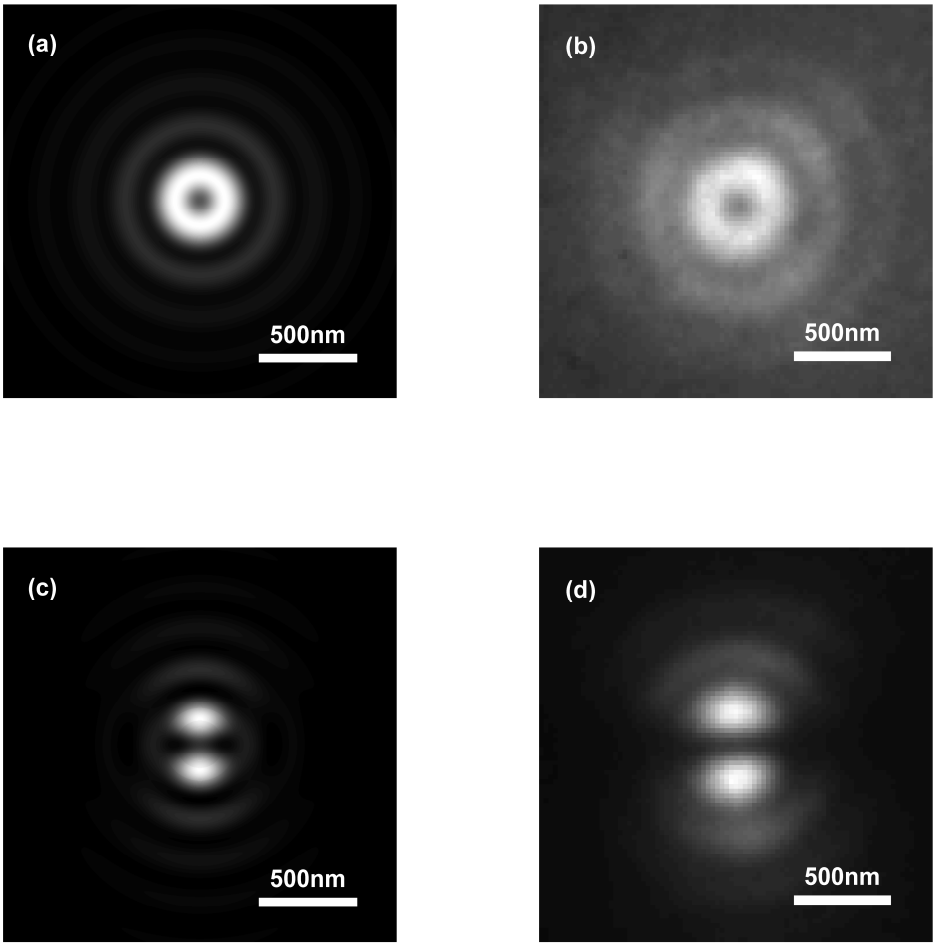

Figure 3-10. A comparison of the theoretical and experimental point spread function. (a) Calculated point spread function of SPCEM (b) Actual point spread function of SPCEM obtained from experiments (c) Theoretical point spread function after adding a linear polarizer between the objective and the tube lens (d) Experimental point spread function after adding a linear polarizer to the relay optics.

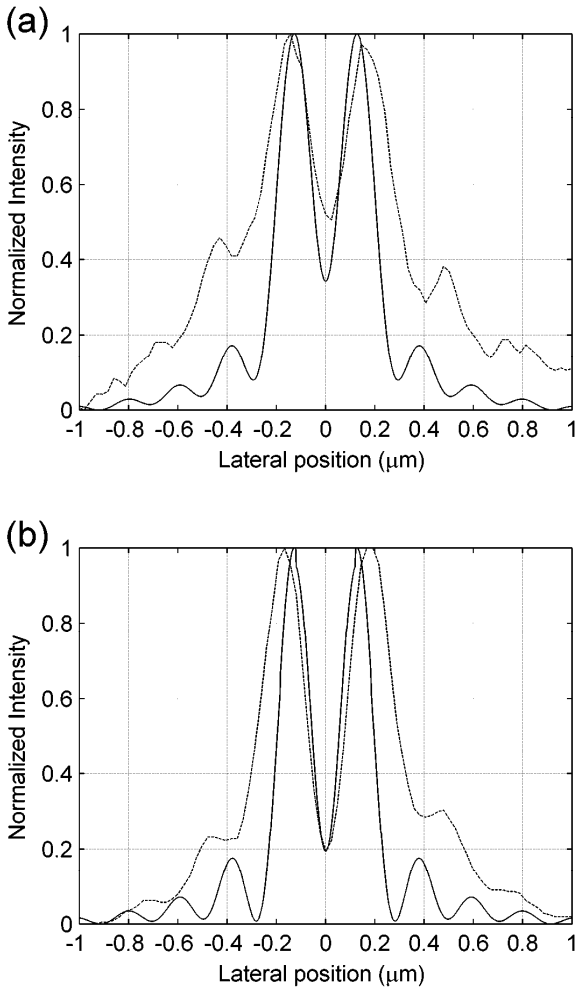

Figure 3-11. A comparison of the cross-sectional profile of the theoretical and experimental results. The calculated point spread functions are shown in smooth lines and the experimental results are shown as dashed lines. (a) Without linear polarizer (b) with linear polarizer.

3.4 Discussion

In summary, SPCEM has many unique characteristics such as the directional radiation pattern of the emission, the near-field quenching effect and its donut-shaped point spread function. From the experimental results, it can be seen that in general, the theoretical results are in agreement with the experimental data, which suggest that the theoretical model is applicable for SPCEM. It has been shown that the point spread function of SPCEM departs from the familiar Airy-disk-like point spread functions of conventional wide-field microscopy and confocal microscopy. Instead, the point spread function of SPCEM resembles a rotationally symmetric annular-like structure with multiple rings. This has a few implications. Firstly, compared with conventional wide-field microscopy where the point spread function typically assumes an Airy-disk structure and the resolution of a microscope is defined using the Rayleigh criterion, it is not so clear in this case how the resolution should be defined and what is its relation to wavelength and numerical aperture. An intuitive way would be to define the resolution of SPCEM by disregarding the "valley" and considering the full-width at half-maximum of the resulting structure. Another way is to calculate the optical transfer function of this optical system. This enables us to compare the resolution of SPCEM in the frequency domain. Furthermore, the irregular point spread function of SPCEM suggests that it is necessary to proceed with caution when interpreting images captured using this method. It is entirely possible the annular-like point spread function may introduce artifacts in images that ultimately lead to misinterpretation. Therefore, it is desirable to compensate for the irregular point spread function prior to

imaging. This could be done via point spread function engineering approaches, or through designing specific deconvolution algorithms for SPCEM.

In this chapter, a model for SPCEM has been derived and its point spread function within a 4f optical system is obtained. It was also shown that the point spread function has a rotationally symmetric annular-like structure and a "valley" in the central region. In addition, the theoretical results were supported with experimental data, both with and without the addition of a linear polarizer. With insight into the point spread function characteristic of SPCEM, further investigation on the optical transfer function characteristics as well as compensation for this irregular point spread function with the central "valley" to improve image resolution are presented in the next two chapters.

CHAPTER 4: OPTICAL TRANSFER FUNCTION OF SURFACE PLASMON-COUPLED EMISSION MICROSCOPY

The point spread function of SPCEM has been shown to be different from normal – a donut shaped structure with rings extending outwards. This is rather unusual compared to many other imaging methods. In this chapter, further insight about SPCEM imaging is obtained by studying the vectorial optical transfer function (OTF) of SPCEM. The vectorial OTF characteristics are also discussed in comparison with that of TIRFM. Section 4.1 derives the vectorial OTF for SPCEM, while section 4.2 compares the results. Section 4.3 presents deconvolution as a correction technique for SPCEM and discusses different deconvolution methods.

4.1 Vectorial Optical Transfer Function

Apart from the point spread function, an imaging system can also be described in the frequency domain by its optical transfer function. The OTF of a system describes how each spatial frequency or angular plane wave is modulated by the system in terms of its amplitude and phase, and can be derived by taking the Fourier Transform of its

intensity point spread function. In three dimensions, the 3D OTF is expressed using the 3D Fourier Transform as

$$H(\mathbf{q}) = \int_{-\infty}^{\infty} \left|h(\mathbf{r})\right|^2 \exp(-2\pi i \mathbf{r}\bullet\mathbf{q})\mathrm{d}\mathbf{q}, \tag{4.1}$$

where h and H respectively denote the amplitude point spread function and optical transfer function of the system, while $\mathbf{r}$ and $\mathbf{q}$ are the spatial (x, y, z) and frequency (m, n, s) coordinates respectively. The above expression applies to the scalar regime where the system point spread function is derived using the scalar wave approximation. However, the calculation of the OTF of an imaging system with a large numerical aperture is difficult because of the vectorial nature of light which breaks the cylindrical symmetry of the pupil function. In order to deal with the polarized nature of light, the scalar OTF has been extended to the more general vectorial case by taking into account all three polarization components and is commonly termed the vectorial optical transfer function (Arnison 2002; Sheppard and Larkin 1997). The vectorial OTF has been used to analyze wide-field fluorescence imaging with large-aperture systems as well as for a 4Pi type system (Schönle and Hell 2002; Bewersdorf et al. 2006).

For a given amplitude point spread function with the three polarization components $\mathbf{h}(\mathbf{r})$, the vectorial OTF is analogously given by

$$H(\mathbf{q}) = \int_{-\infty}^{\infty} \left|\mathbf{h}(\mathbf{r})\right|^2 \exp(-2\pi i \mathbf{r}\bullet\mathbf{q})\mathrm{d}\mathbf{q}. \tag{4.2}$$

Unlike microscopes with low numerical aperture objectives, the use of a high NA objective in TIRFM and SPCEM necessitates the use of the vectorial OTF in its analysis. While in general the three-dimensional vectorial OTF can be derived, for

TIRFM and SPCEM, only the relevant 2D vectorial OTF need to be considered due to their intrinsic sectioning effect by only exciting fluorophores close to the substrate. This is achieved by taking the 2D Fourier Transform of the SPCEM point spread function. From chapter two, the field in the image space is given by

$$\begin{aligned}\mathbf{E_4}(r,\varphi,z) = -\frac{ik_4}{2\pi}\int\int_{\Omega}\mathbf{E_4'}\sin\theta_4\exp(ik_4 r\sin\theta_4\cos(\phi-\varphi)) \\ \times\exp(ik_4 z\cos\theta_4)\exp(i\Phi)\mathrm{d}\theta_4\mathrm{d}\phi\end{aligned} \tag{4.3}$$

and the intensity point spread function is expressed as

$$I_{PSF} = \int_0^{\pi}\int_0^{2\pi}|\mathbf{E_i}|^2\frac{|\mathbf{E_i}|^2}{P_T}\sin\theta_d\mathrm{d}\phi_d\mathrm{d}\theta_d. \tag{4.4}$$

At the image plane where $z = 0$, Equation (4.3) simplifies to

$$\mathbf{E_4}(r,\varphi) = -\frac{ik_4}{2\pi}\int\int_{\Omega}\mathbf{E_4'}\sin\theta_4\exp(ik_4 r\sin\theta_4\cos(\phi-\varphi))\exp(i\Phi)\mathrm{d}\theta_4\mathrm{d}\phi \tag{4.5}$$

By applying the following substitutions

$$m = \frac{\beta\sin\theta_4\cos\phi}{\lambda_4}, n = \frac{\beta\sin\theta_4\sin\phi}{\lambda_4},$$
$$x = \frac{r\cos\varphi}{\beta}, y = \frac{r\sin\varphi}{\beta},$$

Equation (4.5) can be expressed (ignoring a constant factor) as

$$\mathbf{E_4}(x,y) = \int_{-\infty}^{\infty}\int_{-\infty}^{\infty}\mathbf{P}(m,n)e^{2\pi i(mx+ny)}\mathrm{d}m\mathrm{d}n \tag{4.6}$$

where **P** is the vectorial pupil function with components $(P_x, P_y, P_z)^T$. The vectorial OTF of SPCEM is thus given by the 2D Fourier Transform of the intensity point spread function,

$$
\begin{aligned}
H(m,n) &= \mathbf{FT}_{2D}\left[I_{PSF}\right] \\
&= \frac{w_1}{2}\left[\mathbf{P_a}(m,n)\otimes_3 \mathbf{P_a^*}(m,n)+\mathbf{P_b}(m,n)\otimes_3 \mathbf{P_b^*}(m,n)\right] \\
&\quad + w_2\mathbf{P_c}(m,n)\otimes_3 \mathbf{P_c^*}(m,n) \\
&= \frac{w_1}{2}\left[OTF_a + OTF_b\right] + w_2 OTF_c
\end{aligned}
\tag{4.7}
$$

where $\otimes_3$ denotes the autocorrelation operator defined as

$$
\begin{aligned}
\mathbf{P_a}\otimes_3 \mathbf{P_a^*} &= P_{ax}\otimes P_{ax}^* + P_{ay}\otimes P_{ay}^* + P_{az}\otimes P_{az}^* \\
\mathbf{P_b}\otimes_3 \mathbf{P_b^*} &= P_{bx}\otimes P_{bx}^* + P_{by}\otimes P_{by}^* + P_{bz}\otimes P_{bz}^* \\
\mathbf{P_c}\otimes_3 \mathbf{P_c^*} &= P_{ax}\otimes P_{ax}^* + P_{cy}\otimes P_{cy}^* + P_{cz}\otimes P_{cz}^*
\end{aligned}
\tag{4.8}
$$

and

$$
w_1 = \int_0^{\pi} \frac{\sin^3\theta_d}{P_T}\,\mathrm{d}\theta_d,\ w_2 = \int_0^{\pi} \frac{\cos^2\theta_d \sin\theta_d}{P_T}\,\mathrm{d}\theta_d. \tag{4.9}
$$

The pupil functions $\mathbf{P_a}, \mathbf{P_b}, \mathbf{P_c}$ are given by

$$
\mathbf{P_a}(m,n) = \begin{bmatrix} \frac{m^2}{l^2}\left(\tau_p c_1 c_4 - \tau_s\right) + \tau_s \\ \frac{mn}{l^2}\left(\tau_p c_1 c_4 - \tau_s\right) \\ \frac{m}{l}\tau_p c_1 \sqrt{1-c_4^2} \end{bmatrix} \frac{e^{i\Phi}}{\sqrt{c_3 c_4}}
$$

$$
\mathbf{P_b}(m,n) = \begin{bmatrix} \frac{mn}{l^2}\left(\tau_p c_1 c_4 - \tau_s\right) \\ \frac{n^2}{l^2}\left(\tau_p c_1 c_4 - \tau_s\right) + \tau_s \\ \frac{n}{l}\tau_p c_1 \sqrt{1-c_4^2} \end{bmatrix} \frac{e^{i\Phi}}{\sqrt{c_3 c_4}}
$$

$$\mathbf{P_c}(m,n) = \begin{bmatrix} -\frac{m}{l}\tau_p\sqrt{1-c_1^2}c_4 \\ -\frac{n}{l}\tau_p\sqrt{1-c_1^2}c_4 \\ -\tau_p\sqrt{1-c_1^2}\sqrt{1-c_4^2} \end{bmatrix} \frac{e^{i\Phi}}{\sqrt{c_3 c_4}}, \tag{4.10}$$

where $c_1 = \sqrt{1-\frac{NA^2}{n_1^{\,2}}l^2}$, $c_3 = \sqrt{1-\frac{NA^2}{n_3^{\,2}}l^2}$ and $c_4 = \sqrt{1-\frac{NA^2}{\beta^2 n_4^{\,2}}l^2}$. NA and β denote the numerical aperture and magnification of the objective lens, m and n are normalized spatial frequency coordinates and l is the normalized radial coordinate given by $l = \sqrt{m^2+n^2}$. τ_p and τ_s are the three layer Fresnel coefficients and n_1, n_2 and n_3 are the refractive indices of each layer.

4.2 Comparison between TIRFM and SPCEM

For a high NA objective of 1.45 with 60X magnification, a comparison of the vectorial OTF between TIRFM and SPCEM is shown in Figure 4-1. It can be seen that both OTFs are highly similar. However, the vectorial OTF of SPCEM has an "outer ring" that has negative values. For a more detailed examination, the cross section of the transfer function of the surface plasmon microscope can be plotted together with that of a normal TIRF microscope since their vectorial OTFs are axially symmetric. This is depicted in Figure 4-2. Both linear and log-log plots are shown for clarity. In the plot, the horizontal axis represents the normalized spatial frequency passable by the system and varies from a value of 0 to a maximum normalized value of 2. For a TIRF microscope, it can be observed that the optical transfer function is

smoothly varying and is always positive. It decays to zero at the maximum spatial frequency of 2. However, for the surface plasmon microscope, the optical transfer function reaches zero at half the maximum spatial frequency of TIRF with a radial coordinate of 1 and becomes negative for values between 1 and 2. This is clearly shown in the log-log plot where the zero-crossing occurs at m=1. Furthermore, the OTF of SPCEM decays slightly faster than that of TIRF for m<1. For practical

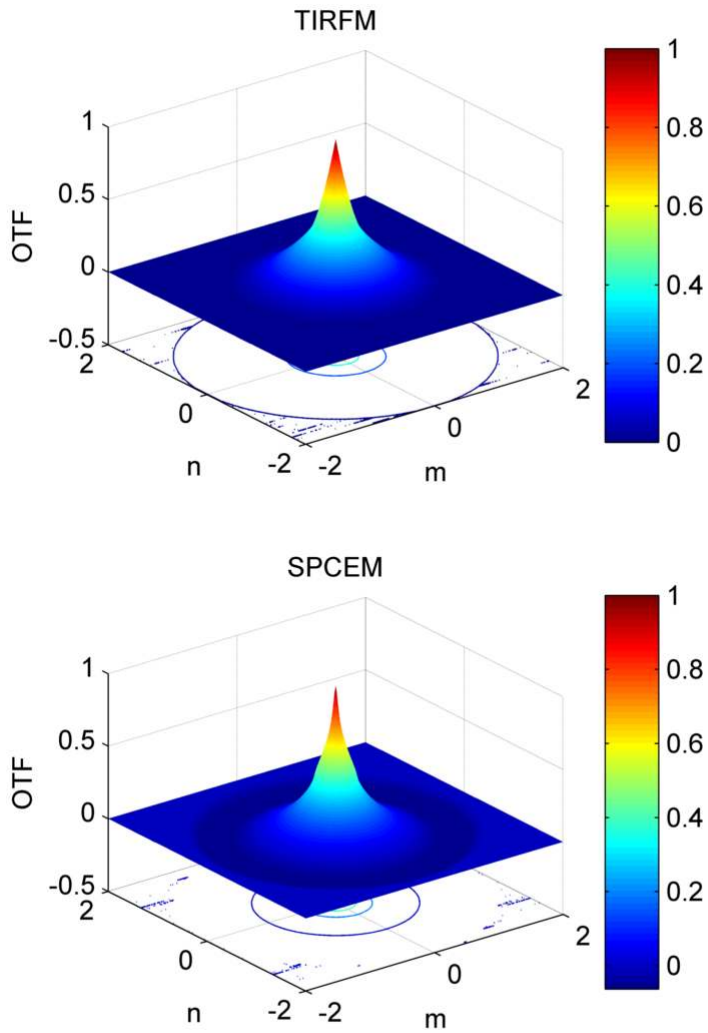

Figure 4-1. Comparison of the 2D Vectorial OTF of TIRFM and SPCEM.

purposes, it can be said that effective spatial frequency passband for SPCEM is half of the passband of TIRFM, and as such the FWHM of SPCEM is roughly two times that of TIRFM. This is evident from chapter three where the resolution of SPCEM was measured experimentally to be about 480 nm as compared to the diffraction limit. Furthermore, the central dip in the point spread function of SPCEM can be attributed

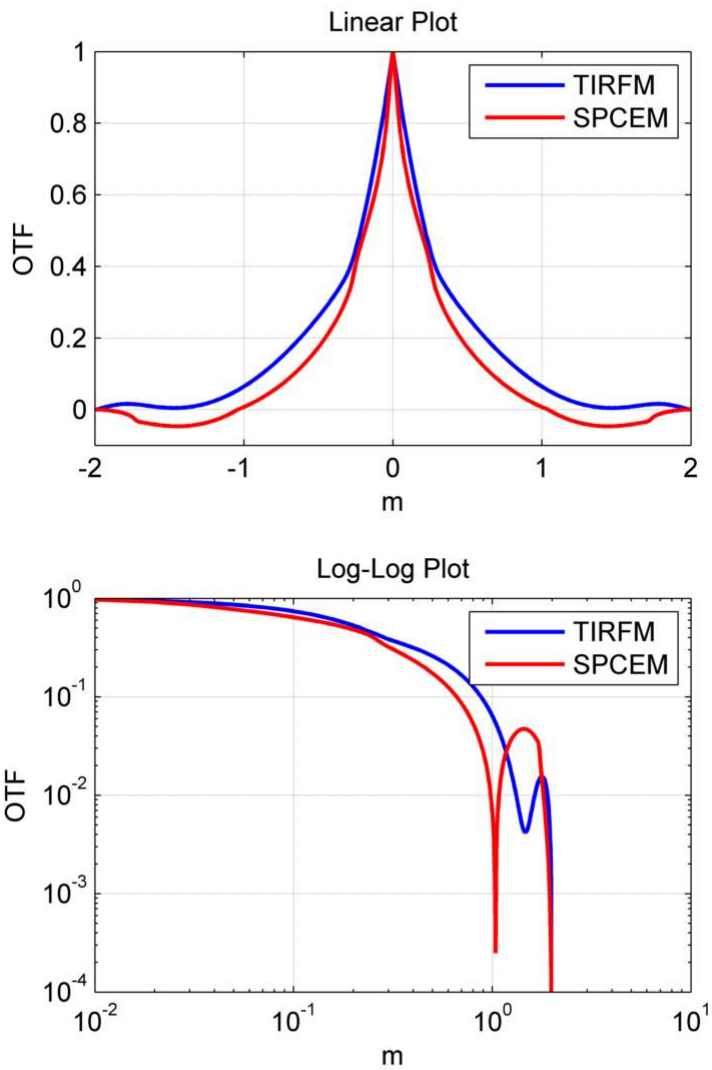

Figure 4-2. Cross-sectional profile of the vectorial OTFs of TIRFM and SPCEM in linear and log-log plots. For the log-log plot, the magnitudes of the OTFs are compared.

to the zero-crossing in its OTF. In practical microscopy when enhancement of the images is desired, the deconvolution technique can be used to restore sharpness to the images and improve their resolution. However, it is pointed out that the zero-crossing in the OTF of SPCEM has implications for applying the deconvolution algorithms in surface plasmon microscopes. In particular, the use of simple inverse filtering techniques is not optimal due to presence of the zeros in the OTF which can affect and boost the high spatial frequency content of noise which is undesirable. Therefore in the next section, different deconvolution methods such as Wiener filtering and Richardson-Lucy deconvolution are applied to SPCEM and their results are compared and discussed in the context of improving the resolution of SPCEM and more importantly, to correct for the donut-shaped point spread function of SPCEM.

4.3 Deconvolution for SPCEM

Deconvolution is a commonly used process that is performed on microscopy images, the main motivation of which is to improve and enhance the images so that they have better contrast, as well as improved resolution for better discrimination of the image details. In general, deconvolution can be classified according to whether the method is linear or non-linear, or alternatively whether it is iterative or non-iterative in nature. Whichever method is used, the primary goal of deconvolution is to determine as far as possible based on certain assumptions, the original object that gave rise to the final acquired images. Mathematically, since the final image $i(x,y)$ is essentially obtained from the convolution between an object $o(x,y)$ and the point spread function of the imaging system $h(x,y)$,

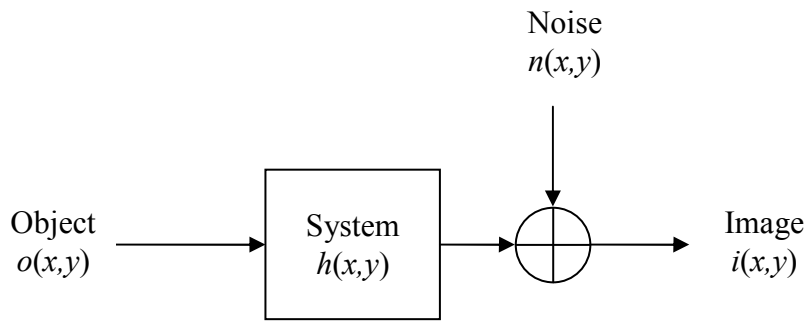

Figure 4-3. Image acquisition model where in general additive noise is also present.

$$i(x,y) = \int\int o(x',y')h(x-x',y-y')\mathrm{d}x'\mathrm{d}y', \tag{4.11}$$

the process of deconvolution can be understood as a mathematical operation which aims to reverse the convolution operation in order to recover the object $o(x,y)$. In general, this problem is ill-posed because of the presence of noise in the image acquisition process as well as due to the zeros in the optical transfer function. Therefore, a simplistic inverse filtering applied in the frequency domain to estimate the object spectrum such as $\hat{O} = H^{-1}I$ cannot be applied owing to these problems due to the non-existence of the inverse, and the tendency to amplify noise. Hence other more sophisticated techniques are thus required.

One well known restoration method which is a linear and non-iterative technique is the Wiener filter. Given an image acquisition process shown in Figure 4-3, or equivalently

$$i(x,y) = \int\int o(x',y')h(x-x',y-y')\mathrm{d}x'\mathrm{d}y' + n(x,y), \tag{4.12}$$

where the additive noise $n(x,y)$ is also taken into account, the Wiener filter aims to estimate the object function $\hat{o}(x,y)$ such that $\hat{o}(x,y) \otimes h(x,y)$ approximates $i(x,y)$ in the least squares sense. In other words, the Wiener filter minimizes the mean squared error between the observation and the estimate, i.e. min $e = \left\| i - \hat{o} \otimes h \right\|^2$. The noise is taken to be statistical and random in nature; if the noise has Gaussian statistics then the Wiener filter is the optimal filter in the least squares sense. The deconvolved image is given in the frequency domain as (Gonzalez 2002)

$$\hat{O}(m,n) = \left[\frac{H^*(m,n)}{\left|H(m,n)\right|^2 + S_n(m,n) / S_o(m,n)} \right] I(m,n), \tag{4.13}$$

where S_n is the power spectrum of the noise and S_o is the power spectrum of the object.

Another method which is iterative and non-linear is Richardson-Lucy deconvolution (Richardson 1972; Lucy 1974; Boutet de Monvel et al. 2001). This method has its foundation in Bayesian statistics and estimates the true image under the assumption of a Poisson process which is appropriate for modeling photon noise. In this restoration method, knowledge of the point spread function of the blurring process is assumed and used in the iteration process. The restoration procedure is shown in Figure 4-4. An initial estimate of the object is used to convolve with the known point spread function and the result together with the observed image $i(x,y)$ is used to update the estimate $\hat{o}(x,y)$ for the next iteration. These steps are then repeated until the termination condition is met. In mathematical terms, the update step in the Richardson-Lucy iterative algorithm is expressed as

$$\hat{o}_{k+1}(x,y) = \hat{o}_k(x,y)\left\{h^*(x,y) \otimes \left[\frac{i(x,y)}{\hat{o}_k(x,y) \otimes h(x,y)}\right]\right\} \tag{4.14}$$

where * denotes the adjoint operator. This algorithm has the property that automatically satisfies the non-negativity constraint since if the initial estimate is non-negative, then subsequent estimated images are also non-negative.

In this section, we apply both Wiener and Richardson-Lucy deconvolution to images simulated with the point spread functions of SPCEM and compare the results of the two deconvolution methods. For this study, we make use of a segment of the EIA 1956 resolution chart as shown in Figure 4-5 as a test image. The specified test image is blurred by the point spread function of SPCEM, and the blurred image is

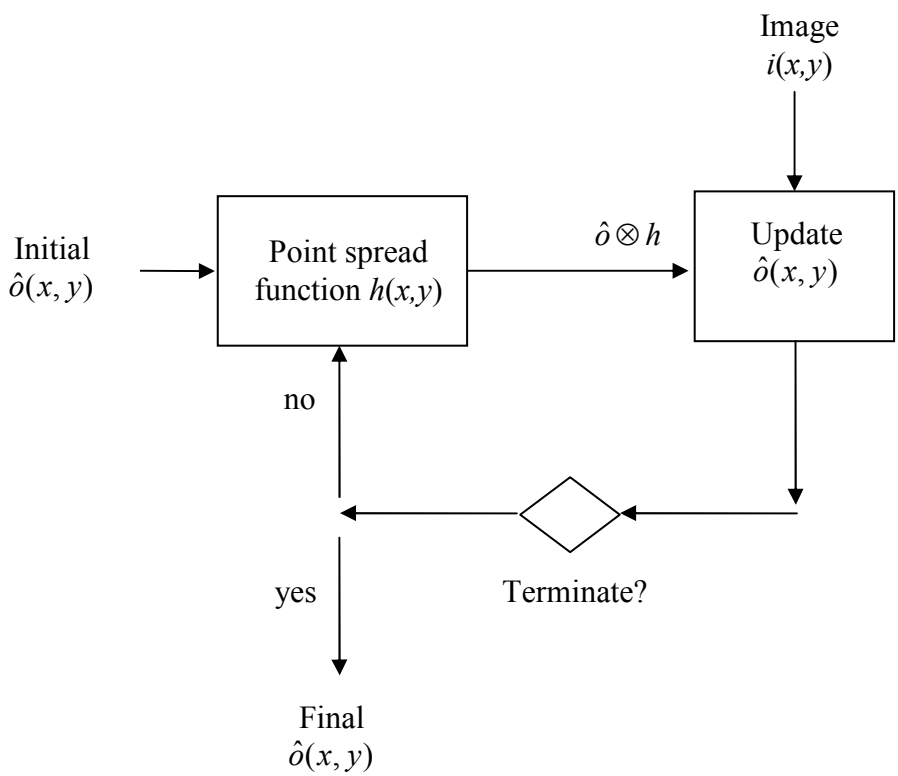

Figure 4-4. Flow chart depicting the Richardson-Lucy deconvolution algorithm.

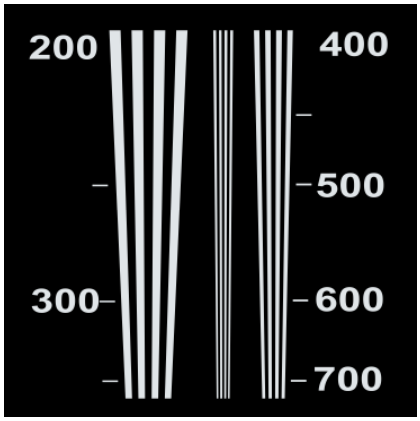

Figure 4-5. Segment of the EIA 1956 resolution test chart used in simulations.

then degraded by adding additive white Gaussian noise with zero mean and different standard deviations of 2% and 20%, respectively, to simulate two cases where the noise level is low and high, respectively. Figure 4-6 shows the test images. For the purpose of control, the test image is also blurred and degraded in the same way but by using the Airy-disk like point spread function of TIRFM. In all the subsequent figures, the left panels display simulation results for TIRFM and right panels are for SPCEM.

Figure 4-6(a) and (b) show the test images being blurred by the respective point spread functions. It is observed that for the case of SPCEM, the images are more blurred and have a “halo”-like appearance owing to the widened donut point spread function. Figure 4-6(c) and (d) show the images after adding a small amount of Gaussian noise with a standard deviation of 2%, while Figure 4-6(e) and (f) show the images with a high level of Gaussian noise with the standard deviation set at 20%. First, the degraded images in Figure 4-6 are restored by applying a simple inverse filter as shown in Figure 4-7. In this demonstration, it can be seen that when no noise is present, simple inverse filtering results in a good restoration that is close to the

original unblurred image. However when noise is present, the simple inverse filtering method causes the noise to be over-amplified due to the zeros in the transfer function as can be seen from Figure 4-7(d) to (f), resulting in very poor reconstruction of the images. For the case of low noise, the image details can still be discerned amidst the amplified noise, whereas for the case of high noise, the restored image is almost beyond recognition.

In contrast, Wiener filtering takes into account the noise and suppresses the noise as far as possible in the restoration shown in Figure 4-8. When there is no noise, Wiener filtering also gives good results (see Figure 4-8(a) and (b)). For the case where the noise level is low, a reasonably good reconstruction is achieved as shown in Figure 4-8(c) and (d) except for the presence of some "ringing". However, when the image is considerably noisier in Figure 4-8(e) and (f), the restoration becomes poorer especially for the SPCEM case in Figure 4-8(f) where the image has a grainy looking appearance.

In Figure 4-9, the results after applying the Richardson-Lucy deconvolution are shown. As before, Figure 4-9(a) and (b) show that when no noise is present, the deconvolution results in a good restoration which closely resembles the original test image. When the noise level is low, Richardson-Lucy deconvolution also gives reasonably good results (see Figure 4-9(c) and (d)) comparable to the no-noise case, and which look better than Wiener filtering due to the absence of "ringing". When the noise level is much higher in Figure 4-9(e) and (f), Richardson-Lucy deconvolution still gives a qualitatively better restoration than Wiener filtering because it does not have a grainy appearance. In summary, the simulations show that deconvolution can

be used to improve an image acquired by SPCEM. Simple inverse filtering does not give good restoration results due to amplification of noise and therefore one must resort to better deconvolution techniques. Wiener filtering and Richardson-Lucy deconvolution are methods which account for the presence of noise and give reasonably good results. However, Richarson-Lucy deconvolution gives qualitatively better results in our simulations as compared to Wiener filtering which tends to cause "ringing" and graininess in the restored images especially for the case of SPCEM. In the next chapter, optical methods are introduced which can compensate for the distorted point spread function of SPCEM. Optical methods can have an advantage over deconvolution because of the fact that since photon and Gaussian noise are mostly generated due to the final image acquisition stage, optical methods tend not to affect the final results as compared to deconvolution which operates on the final captured image as a whole.

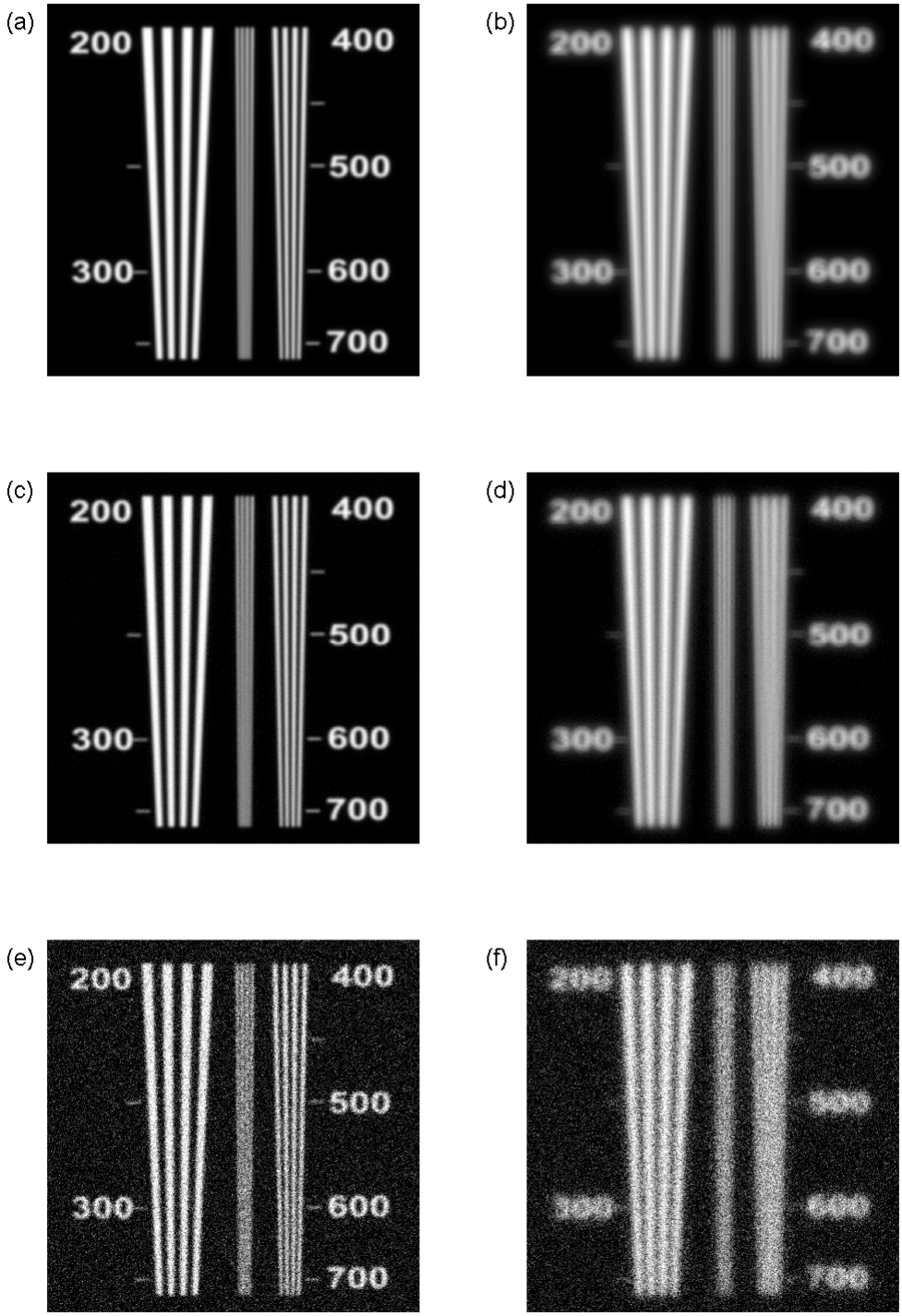

Figure 4-6. Test images are blurred and degraded by noise. Left: TIRFM, right: SPCEM. (a),(b) Blurred image (c),(d) with Gaussian noise (standard deviation 2%) (e),(f) with Gaussian noise (standard deviation 20%).

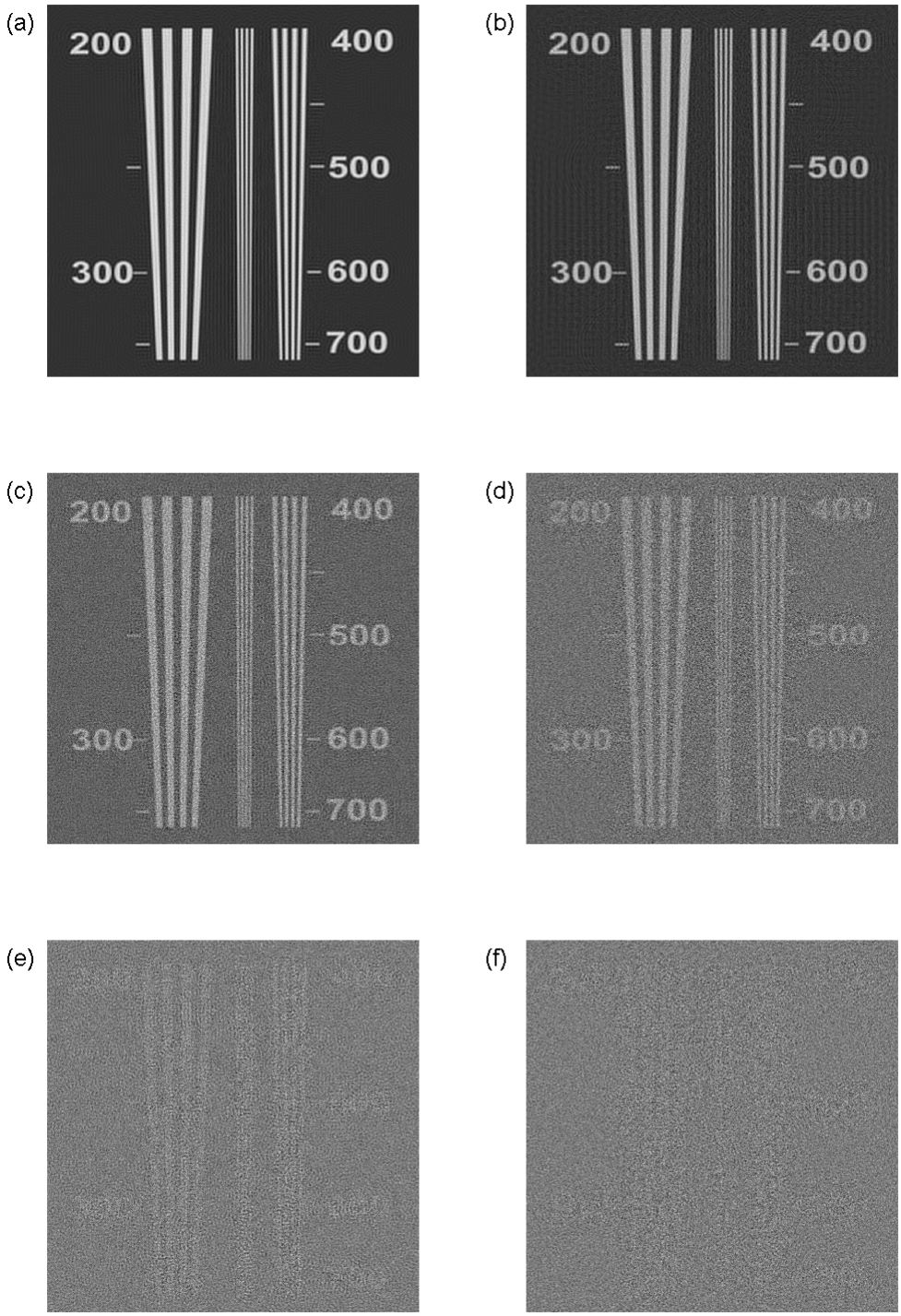

Figure 4-7. Simple inverse filtering. Left: TIRFM, right: SPCEM. (a),(b) Without noise (c),(d) with Gaussian noise (standard deviation 2%) (e),(f) with Gaussian noise (standard deviation 20%).

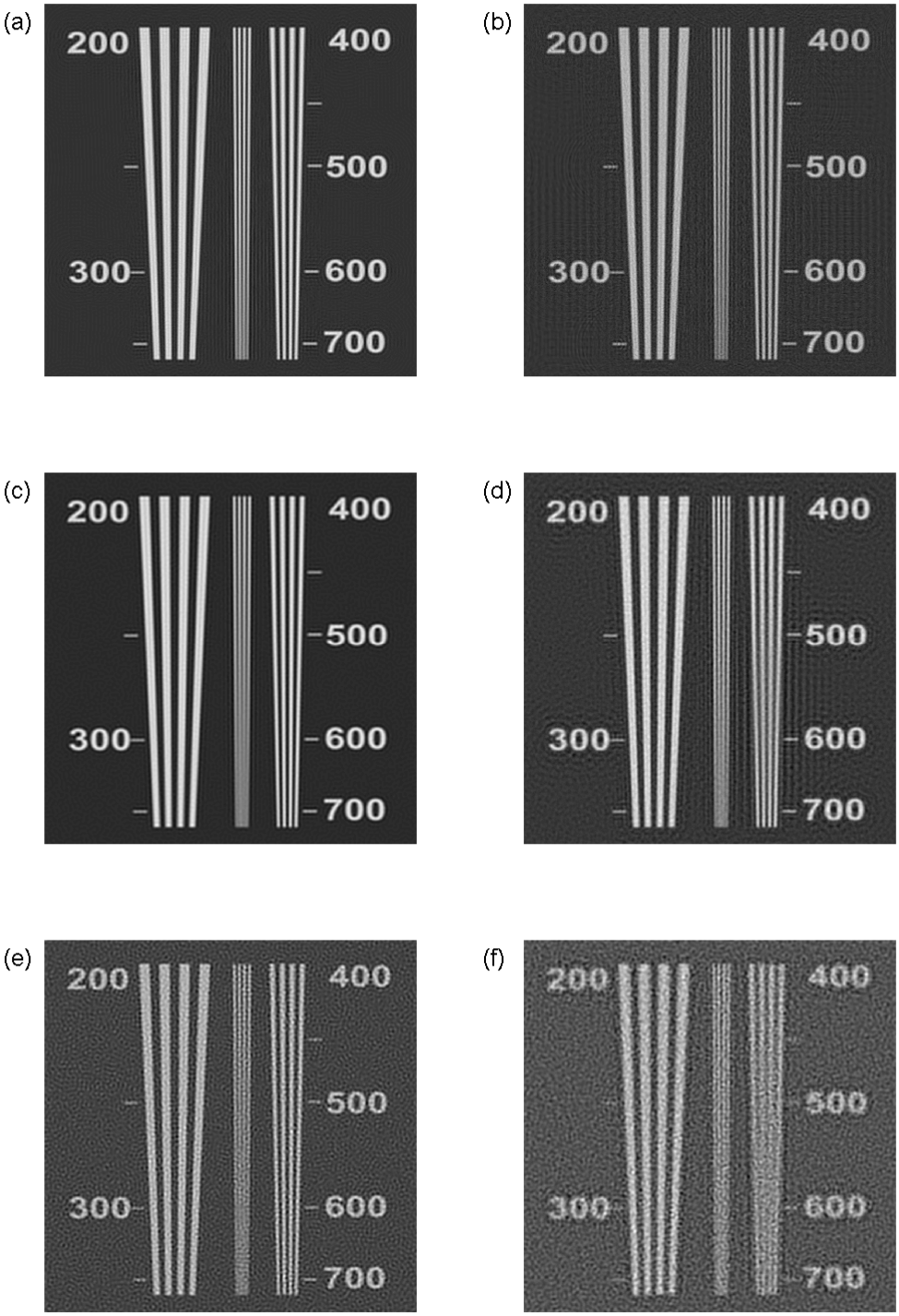

Figure 4-8. Wiener deconvolution. Left: TIRFM, right: SPCEM. (a),(b) Without noise (c),(d) with Gaussian noise (standard deviation 5%) (e),(f) with Gaussian noise (standard deviation 20%).

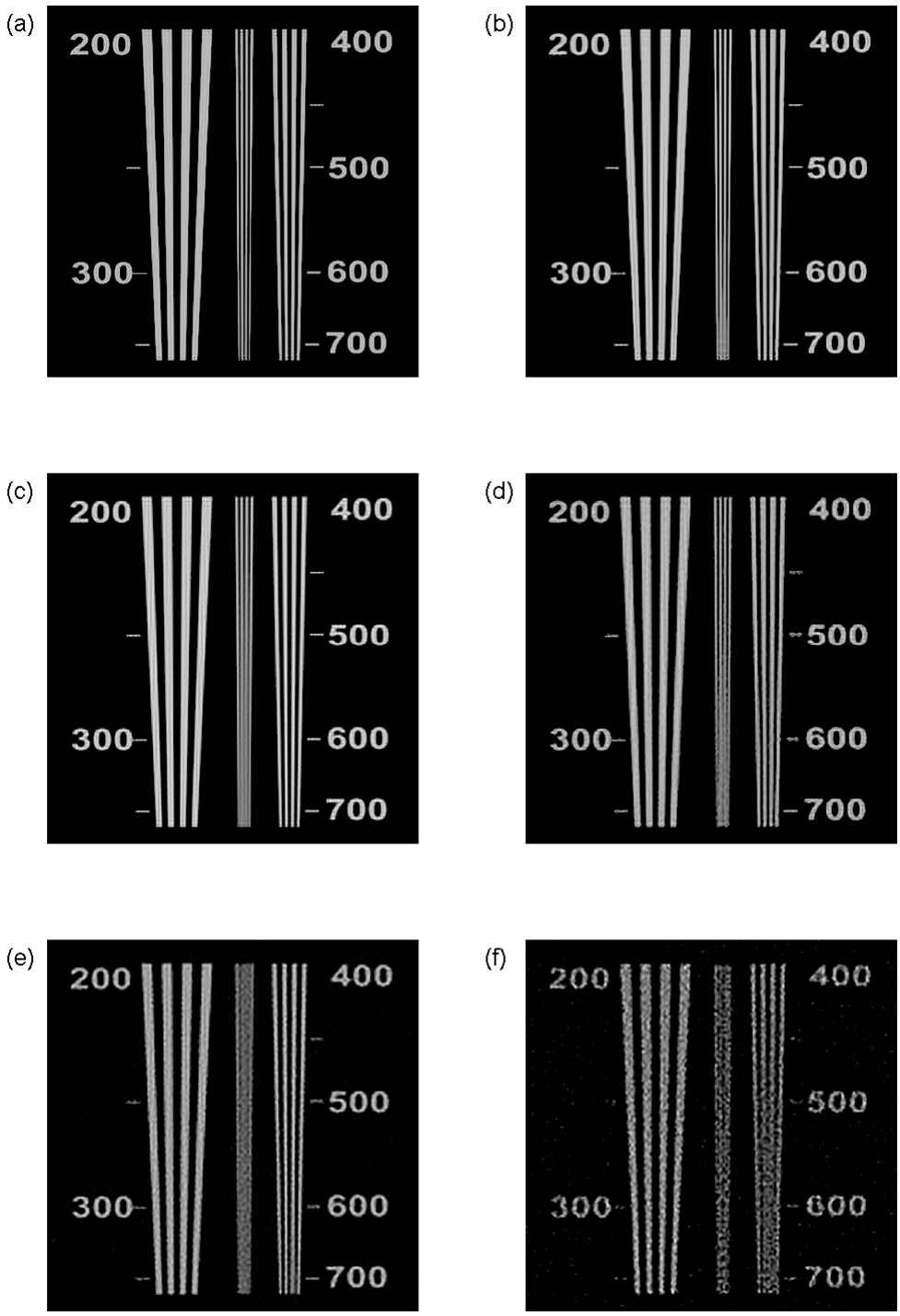

Figure 4-9. Richardson-Lucy deconvolution. Left: TIRFM, right: SPCEM. (a),(b) Without noise (c),(d) with Gaussian noise (standard deviation 5%) (e),(f) with Gaussian noise (standard deviation 20%).

CHAPTER 5: OPTICAL COMPENSATION FOR SURFACE PLASMON-COUPLED EMISSION MICROSCOPY

Although the surface plasmon-coupled emission microscope provides high sensitivity for surface imaging, it was shown that it suffers from a distorted donut shape point spread function and has a FWHM that is two times worse than the diffraction limit. Thus for proper imaging it is necessary to correct for the distortion by converting the donut shape into the circularly symmetric and single lobe which is more preferable. The previous chapter analyzed the vectorial OTF of SPCEM and studied numerical deconvolution techniques as a means for correction of the point spread function. Although numerical deconvolution can be used to mitigate the distortions in the point spread function, it can suffer from several limitations, such as the inadvertent enhancement of noise artifacts. More importantly, it requires prior measurement of the system point spread function and this has practical difficulties especially in biological experiments where measurements can be dynamic. In this chapter, we develop optical methods which can convert the donut point spread function to an

Airy-disk like shape and analyze the methods. Experimental results are also demonstrated to show the feasibility of the proposed methods.

5.1 Theoretical Basis

The donut point spread function of SPCEM has a dark spot in the center which can be understood in two perspectives – in terms of the emission polarization profile and in the Fourier domain using the vectorial optical transfer function. First, the polarization pattern of the electric field at the back focal plane of the objective at a time instant t=0 is calculated and plotted in Figure 5-1. Here, the objective NA is assumed to be 1.45 and the spatial frequencies, k_x and k_y, have been normalized to the free space wave number. From the figure, it can be seen that polarization direction is predominantly radial in direction which is due to the coupled surface plasmons having a preferred p-polarized emission. Such an emission pattern causes the field to interfere

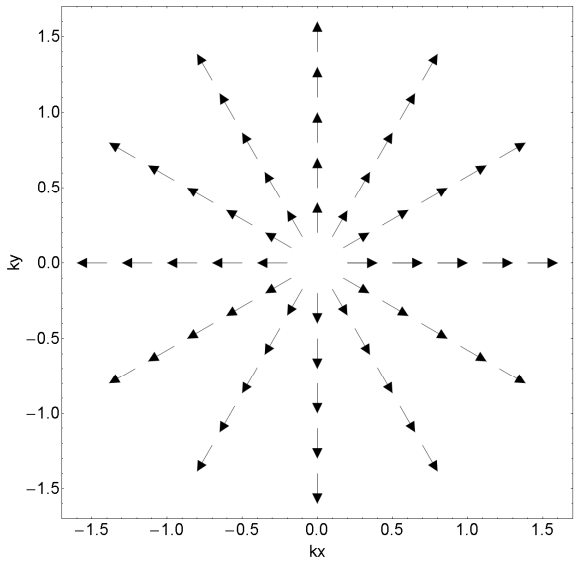

Figure 5-1. Polarization pattern of the electric field at the back focal plane of the objective at time instant t=0.

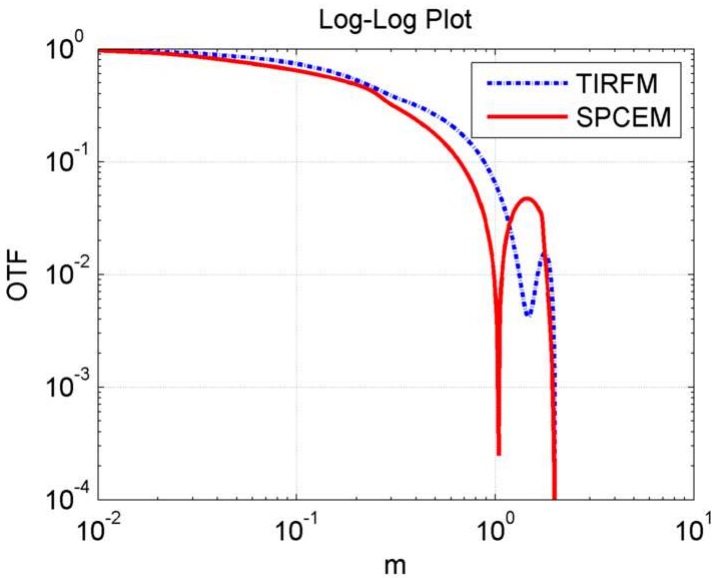

Figure 5-2. A log-log plot comparing the magnitudes of the vectorial OTFs of SPCEM (solid line) and TIRFM (dashed line).

destructively on-axis when refocused on to the CCD with a low NA imaging lens thereby resulting in the dip at the centre of the point spread function which causes the donut shape that is evident in SPCEM.

Second, in the frequency domain, the magnitude of the vectorial OTF which takes into account the depolarization effects in each field component caused by the high NA 1.45 objective is plotted in Figure 5-2 using logarithmic scale in both axes. The OTF for TIRFM is included for the purpose of comparison. The vectorial OTFs are rotationally symmetric and their spatial frequencies have been normalized with a maximum value of 2. m denotes the spatial frequency within a cross-section of the OTF. As can be seen in Figure 5-2, for both SPCEM and TIRFM, the OTFs are largely similar for spatial frequencies $m < 1$. However, the OTF of SPCEM results in values which turn negative for spatial frequencies greater than one. This implies that for spatial frequencies $m > 1$, there is a phase change of π which results in a reversal

of contrast for those high spatial frequencies. The donut point spread function of SPCEM and the dip in its center can be attributed to the contrast reversal present for $m > 1$ where the OTF turns negative. Therefore by modifying the set-up of SPCEM such that the vectorial OTF is always positive for all spatial frequencies, one can convert the donut shape point spread function into a single lobe.

It can be shown that for the central dip in the donut point spread function to exist, a necessary condition is that the vectorial OTF must turn negative for some spatial frequencies. It is analogous to the scenario that if the center of the point spread function has a value of zero, then the OTF must necessarily contain negative values by virtue of the fact that its integration over all frequencies must be equal to zero. The following applies to the case where the center dip need not be zero. Let the rotationally symmetric point spread function be denoted by $h(r)$ and its vectorial OTF be denoted by $H(l)$, where r is the spatial coordinate and l is the spatial frequency. They are related by the Hankel Transform

$$h(r) = \int_0^\infty H(l) J_0(rl) \mathrm{d}l. \tag{5.1}$$

The point spread function derivatives are given by

$$\begin{aligned} \frac{\partial h}{\partial r} &= -\int_0^\infty H(l) J_1(rl) l \mathrm{d}l \\ \frac{\partial^2 h}{\partial r^2} &= -\frac{1}{2}\int_0^\infty H(l)\left[J_0(rl) - J_2(rl)\right] l^3 \mathrm{d}l. \end{aligned} \tag{5.2}$$

Thus it can be seen that if $H(l)$ is always positive, then the second derivative $\frac{\partial^2 h}{\partial r^2}$ at the origin $r = 0$ is negative, implying that the origin is a local maximum. Hence, it is

necessary that the vectorial OTF be negative for some l for $\frac{\partial^2 h}{\partial r^2}$ to be positive at the origin to result in a local minimum. Alternatively, one can also consider the following expression

$$h(0)-h(r)=\int_0^\infty H(l)\left(1-J_0(rl)\right)l\mathrm{d}l. \tag{5.3}$$

Since $\left(1-J_0(rl)\right)\geq 0$ for all $r,l\geq 0$, it follows that if $H(l)$ is non-negative, then it is evident that

$$h(0)-h(r)\geq 0,\ \text{for}\ \forall r\ \text{where}\ r\geq 0, \tag{5.4}$$

implying that $h(0)$ is the global maximum. Thus it can be seen that for a dip to exist, $H(l)$ must necessarily contain negative values for some spatial frequencies.

5.2 Modification to SPCEM

In order to optically correct the distorted point spread function of SPCEM by converting it to a single lobe Airy disk-like morphology which is more appropriate for imaging, the proposed modification of the microscope is shown in the schematic in Figure 5-3. In the figure, an inverted total internal reflection fluorescence microscope with a high NA objective is used. In the set-up, fluorescent probes on the metal-coated cover slip are excited by surface plasmons which are in turn excited by the *p*-polarized plane wave incident at the surface plasmon resonance angle. Fluorescence emission is then collected by the same objective. Along the infinity corrected detection path at a point conjugate to the back focal plane, we place a conversion element before the CCD imaging lens. For the proposed modification, we find that

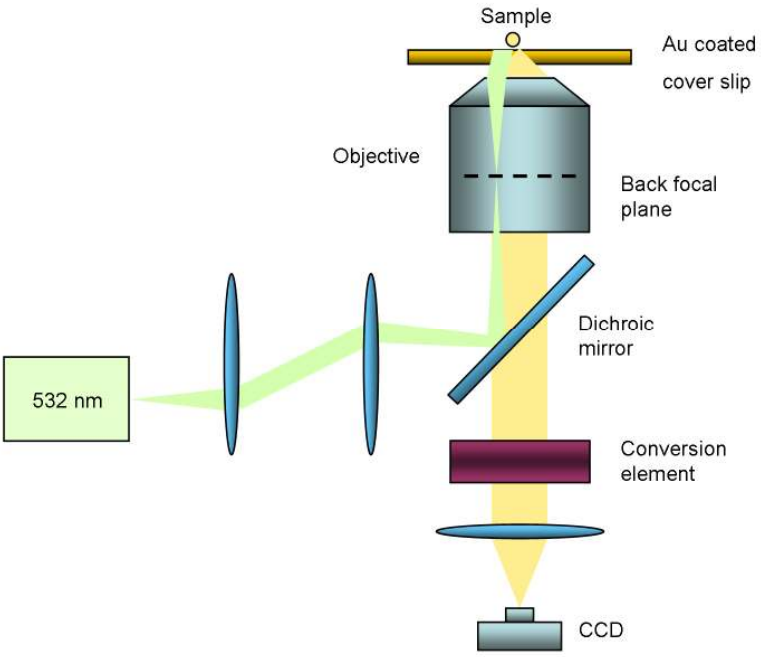

Figure 5-3. Proposed modified SPCEM imaging with the addition of a conversion element.

two possible choices for the conversion element are either a spiral phase plate or a polarization mode converter that can be used for converting the point spread function. These elements will be discussed next in more detail.

5.2.1 Spiral phase plate

A single order spiral phase plate (SPP) can be used to incorporate a spiral phase to the emission light prior to CCD imaging. The SPP is an optical element that has found many uses in various applications such as optical trapping, quantum computation, image processing and dark-field microscopy (Fuerhapter et al. 2005; Larkin et al. 2001; Mair et al. 2001; Simpson et al. 1996). It has a thickness which increases

linearly with the azimuthal angle. For an SPP with topological charge of one, its thickness is given by

$$d = d_0 + \frac{\lambda\varphi}{2\pi(n-1)}, \tag{5.5}$$

where d_0 is the base thickness of the plate, λ is the emission wavelength, n is the refractive index of the plate and φ denotes the azimuthal angle. The insertion of the SPP adds a phase delay of $\exp(i\varphi)$ to the wavefront of the emission light. Figure 5-4(a) shows the structure of an SPP.

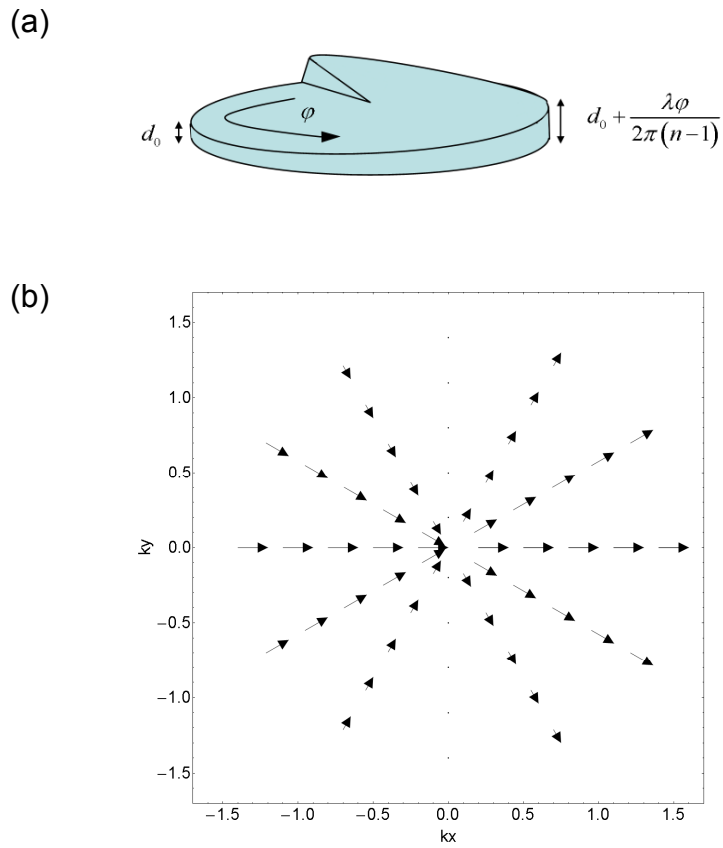

Figure 5-4. (a) A spiral phase plate made from material with refractive index n and designed for a wavelength of λ (b) polarization pattern of the field at the back focal plane of the objective after passing through the element.

The addition of the SPP into the optical path affects the polarization of the field at the back focal plane of the objective. The electric field is calculated and its polarization pattern is shown for a time instant t=0 in Figure 5-4(b). As discussed previously, without the SPP, the SPCE emission displays a radial polarization pattern which causes a dip in the point spread function when refocused with a low NA imaging lens. This is caused by the destructive interference on-axis. The effect of the SPP is that it causes polarization vectors within each meridional plane to be in phase and since in each plane the polarization vectors are always in phase, this causes the field to interfere constructively at the focus, hence yielding a single lobed PSF without the dip.

5.2.2 Polarization mode converter

Another optical element that can achieve the aim of point spread function compensation is a polarization mode converter (PMC). The PMC is an optical element that can convert one polarization mode to another. In the case of SPCEM, a radial to linear polarization mode conversion is required to convert from a donut shape point spread function to one with a single lobe. To achieve radial to linear polarization conversion, a polarization rotator can be used to rotate the polarization at each point in the back focal plane of the objective according to its azimuthal angle location. The Jones matrix of the polarization rotator device can be expressed in terms of the azimuthal angle as

$$P(\phi)=\begin{bmatrix}\cos\phi & \sin\phi & 0\\ -\sin\phi & \cos\phi & 0\\ 0 & 0 & 1\end{bmatrix}. \tag{5.6}$$

Therefore, for radially polarized light which has a polarization vector of the form $\left(\cos\phi,\sin\phi,0\right)^T$, the polarization after passing through the device becomes

$$\begin{aligned}P(\phi)\bullet\begin{bmatrix}\cos\phi\\ \sin\phi\\ 0\end{bmatrix}&=\begin{bmatrix}\cos\phi & \sin\phi & 0\\ -\sin\phi & \cos\phi & 0\\ 0 & 0 & 1\end{bmatrix}\bullet\begin{bmatrix}\cos\phi\\ \sin\phi\\ 0\end{bmatrix}\\ &=\begin{bmatrix}1\\ 0\\ 0\end{bmatrix},\end{aligned} \tag{5.7}$$

which is linearly polarized in the horizontal x direction. Thus, all the polarization states at every point now become aligned uniformly in the x direction. As it is known that focusing and imaging linearly polarized light by a low NA lens give rise to a single lobe (Gu 2000), it is clear that the polarization mode converter is able to remove the dip present in the donut point spread function of SPCEM.

In practice, the PMC can be realized by using a segmented wave-plate approach to approximate a polarization converter (Dorn et al. 2003; Nanophoton Corp. 2010). The wave-plate may contain either four or eight segments, where each segment is a half-wave plate with its optical axis oriented such that the field in the segment is rotated from the radially polarized direction to the horizontally polarized direction. This method, however, has the disadvantage that the field is not uniformly polarized in the desired direction due to the discrete and finite number of segments in the device. Another disadvantage is that this device is typically designed to work within a narrowband of frequencies about a center wavelength.

Another practical realization of the PMC consists of a liquid crystal device that contains a plate that is circularly rubbed on one face to align the liquid crystal molecules in a circular way, and linearly rubbed on the opposite face to align the molecules horizontally as shown in Figure 5-5(a). This device works by guiding and rotating the polarization of the propagating radially polarized wave to the horizontal orientation (Stalder and Schadt 1996). A π phase shifter plate is required to compensate for the $\lambda/2$ phase step on one half of the plate which is caused by the different rotation sense of the liquid crystal molecules on the two halves of the plate. As an aside, the device is also able to convert from azimuthal polarization to linear polarization as well. For our experiments, the liquid crystal PMC is chosen instead of the segmented wave-plate due to its versatility, its ability to operate over a large range of wavelengths as well as its lower cost compared to the segment wave-plate device. Figure 5-5(b) shows the back focal plane polarization pattern after the emission light has passed through the PMC element. In essence, the radially polarized field is rotated to become linearly polarized, and when focused onto the CCD, it results in a single lobe structure.

5.2.3 Comparison of SPP and PMC

Apart from the difference in the polarization patterns at the back focal plane for both SPP and PMC, a comparison can also be made in terms of improvement in their point spread functions and vectorial OTFs. The performance of the SPP and PMC elements are also compared. Expressions for the vectorial OTF of the SPP are similar to the OTF of SPCEM in the previous chapter, except for the introduction of a first order

spiral phase $\exp(i\phi)$ to the pupil functions. For the PMC, expressions for the

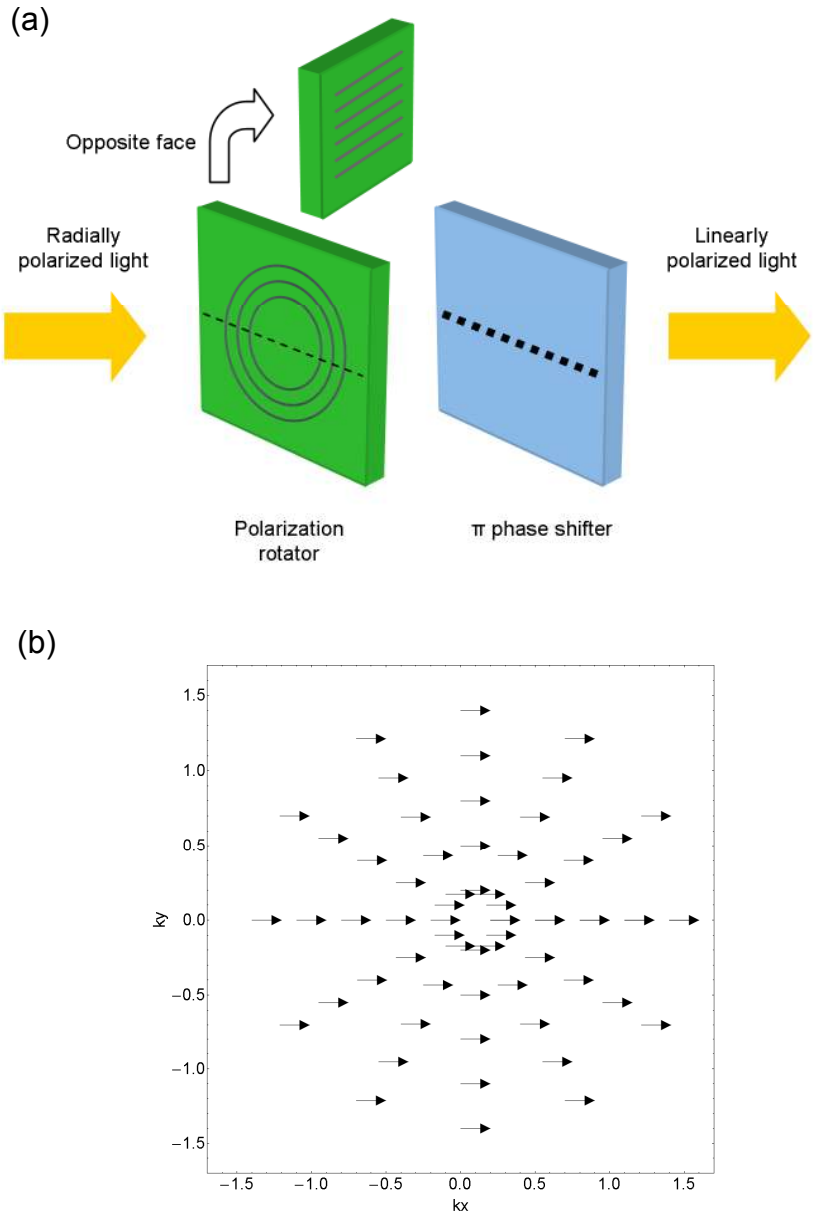

Figure 5-5. (a) A polarization mode converter consisting of a circularly rubbed plate and a π phase shifter. The back face of the plate is linearly rubbed. (b) polarization pattern of the field at the back focal plane of the objective after passing through the element.

vectorial OTF of PMC are different and are given by

$$
\begin{aligned}
H(m,n) &= \mathbf{FT}_{2D}\left[I_{PSF}\right] \\
&= \frac{w_1}{2}\left[\mathbf{P_a}(m,n)\otimes_3 \mathbf{P_a^*}(m,n)+\mathbf{P_b}(m,n)\otimes_3 \mathbf{P_b^*}(m,n)\right] \\
&\quad + w_2\mathbf{P_c}(m,n)\otimes_3 \mathbf{P_c^*}(m,n) \\
&= \frac{w_1}{2}\left[OTF_a + OTF_b\right] + w_2 OTF_c,
\end{aligned}
\tag{5.8}
$$

where $\otimes_3$ denotes the autocorrelation operator and

$$
\begin{aligned}
w_1 &= \int_0^{\pi} \frac{\sin^3\theta_d}{P_T}\,\mathrm{d}\theta_d, \\
w_2 &= \int_0^{\pi} \frac{\cos^2\theta_d \sin\theta_d}{P_T}\,\mathrm{d}\theta_d.
\end{aligned}
\tag{5.9}
$$

The pupil functions $\mathbf{P_a}, \mathbf{P_b}, \mathbf{P_c}$ are given by

$$
\mathbf{P_a}(m,n) = \begin{bmatrix} \frac{mn^2}{l^3}\left(\tau_p c_1 + \tau_s\right)\left(1-c_4\right) + \frac{m}{l}\tau_p c_1 c_4 \\ -\frac{m^2 n}{l^3}\left(\tau_p c_1 + \tau_s\right)\left(1-c_4\right) - \frac{n}{l}\tau_s c_4 \\ \frac{m^2}{l^2}\left(\tau_p c_1 + \tau_s\right)\sqrt{1-c_4^2} - \tau_s\sqrt{1-c_4^2} \end{bmatrix} \frac{e^{i\Phi}}{\sqrt{c_3 c_4}}
$$

$$
\mathbf{P_b}(m,n) = \begin{bmatrix} -\frac{m^2 n}{l^3}\left(\tau_p c_1 + \tau_s\right)\left(1-c_4\right) + \frac{n}{l}\tau_p c_1 \\ -\frac{mn^2}{l^3}\left(\tau_p c_1 + \tau_s\right)\left(1-c_4\right) + \tau_s \\ \frac{mn}{l^2}\left(\tau_p c_1 + \tau_s\right)\sqrt{1-c_4^2} \end{bmatrix} \frac{e^{i\Phi}}{\sqrt{c_3 c_4}}
$$

$$
\mathbf{P_c}(m,n) = \begin{bmatrix} -\frac{n^2}{l^2}\tau_p\sqrt{1-c_1^2}\left(1-c_4\right) - \tau_p\sqrt{1-c_1^2}\,c_4 \\ \frac{mn}{l^2}\tau_p\sqrt{1-c_1^2}\left(1-c_4\right) \\ -\frac{m}{l}\tau_p\sqrt{1-c_1^2}\sqrt{1-c_4^2} \end{bmatrix} \frac{e^{i\Phi}}{\sqrt{c_3 c_4}}
\tag{5.10}
$$

where $c_1 = \sqrt{1 - \frac{NA^2}{n_1^2} l^2}$, $c_3 = \sqrt{1 - \frac{NA^2}{n_3^2} l^2}$ and $c_4 = \sqrt{1 - \frac{NA^2}{\beta^2 n_4^2} l^2}$. NA and β denotes the numerical aperture and magnification of the objective lens, m and n are normalized spatial frequency coordinates and l is the normalized radial coordinate given by $l = \sqrt{m^2 + n^2}$. τ_p and τ_s are the three layer Fresnel coefficients and n_1, n_2

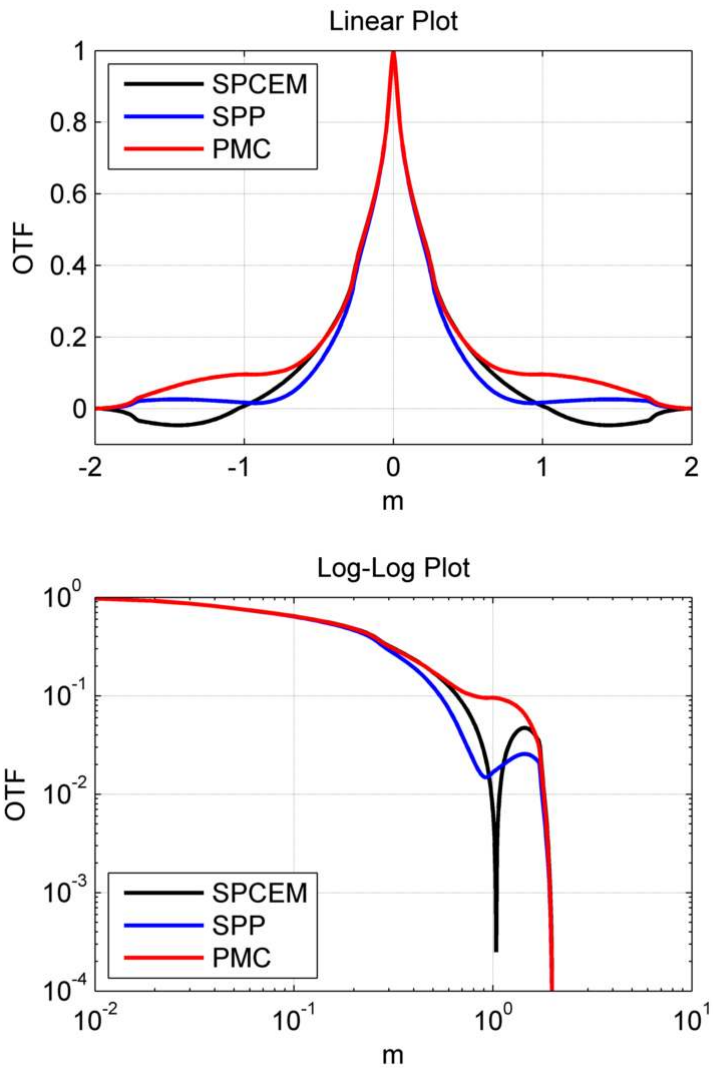

Figure 5-6. A comparison of the cross-sectional profile of the vectorial OTFs in linear and log-log plots with SPP and PMC. For the log-log plot, the magnitudes of the OTFs are compared.

and n_3 are the refractive indices of each layer.

Figure 5-6 shows the vectorial OTFs of adding the SPP or the PMC to the set-up, and compares them with the OTF when none of the conversion elements is used. As discussed, the SPCEM OTF contains negative values for $m > 1$ which causes the dip in the point spread function. In comparison, after the SPP or PMC element is added to the set-up, their vectorial OTFs become positive for the whole support of the spatial frequencies. This can be seen in the log-log plot of the OTF magnitudes in the figure in which the SPP and PMC graphs do not have a zero crossing. Another observation is that inserting the PMC element results in an OTF whose magnitude is consistently greater than the OTF of SPP. This is especially noticeable for normalized spatial frequencies greater than 0.8 where the difference is more pronounced. Because of the enhanced high frequencies of the PMC OTF compared to SPP, the point spread function FWHM of the PMC is slightly narrower at 177 nm than that of the SPP which is 193 nm as shown in Figure 5-7. Both of them also have narrower FWHM compared to SPCEM and are single-lobed structures unlike the donut shape structure of SPCEM.

Since alignment errors of the conversion element is likely to be present in the experimental set-up, the effects misalignment of the element has on the point spread function of the system are further investigated. As the system is rotationally invariant, only translational misalignment with respect to the back aperture of the objective is considered. Two metrics are defined: I_0 which measures the ratio of intensity at the origin to the peak intensity, as well as FWHM (normalized by the FWHM of a perfectly aligned element). These are then plotted as a function of translational

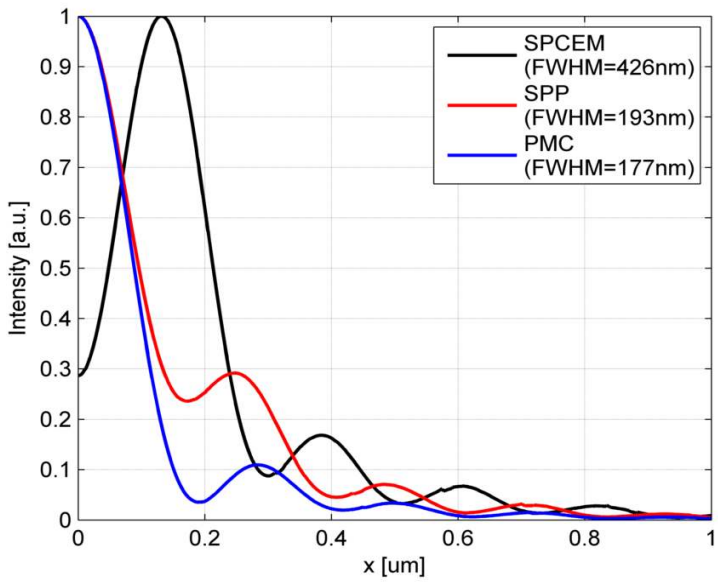

Figure 5-7. Point spread function comparison of SPCEM, with addition of SPP, and with PMC.

misalignment Δw (normalized by the back aperture radius). Results for the SPP and PMC are shown in Figure 5-8(a) and Figure 5-8(b) respectively. In general, translational misalignment breaks the cylindrical symmetry of the point spread function, therefore the worst case FWHMs are plotted in the figures. For the SPP, the graph shows relatively good robustness to misalignment up to a value of Δw = 0.5, with only a corresponding increase in FWHM of ~12% and a decrease of ~15% in I_0. The same metrics under the scenario where the target wavelength of the actual SPP deviates from the designed wavelength are also plotted in the same graph. This can happen, for example during fabrication due to errors inherent in the fabrication process. I_0 and FWHM metrics for wavelength mismatch Δλ/λ of ±10% are relatively flat, which indicates strong robustness to errors in the designed SPP wavelength.

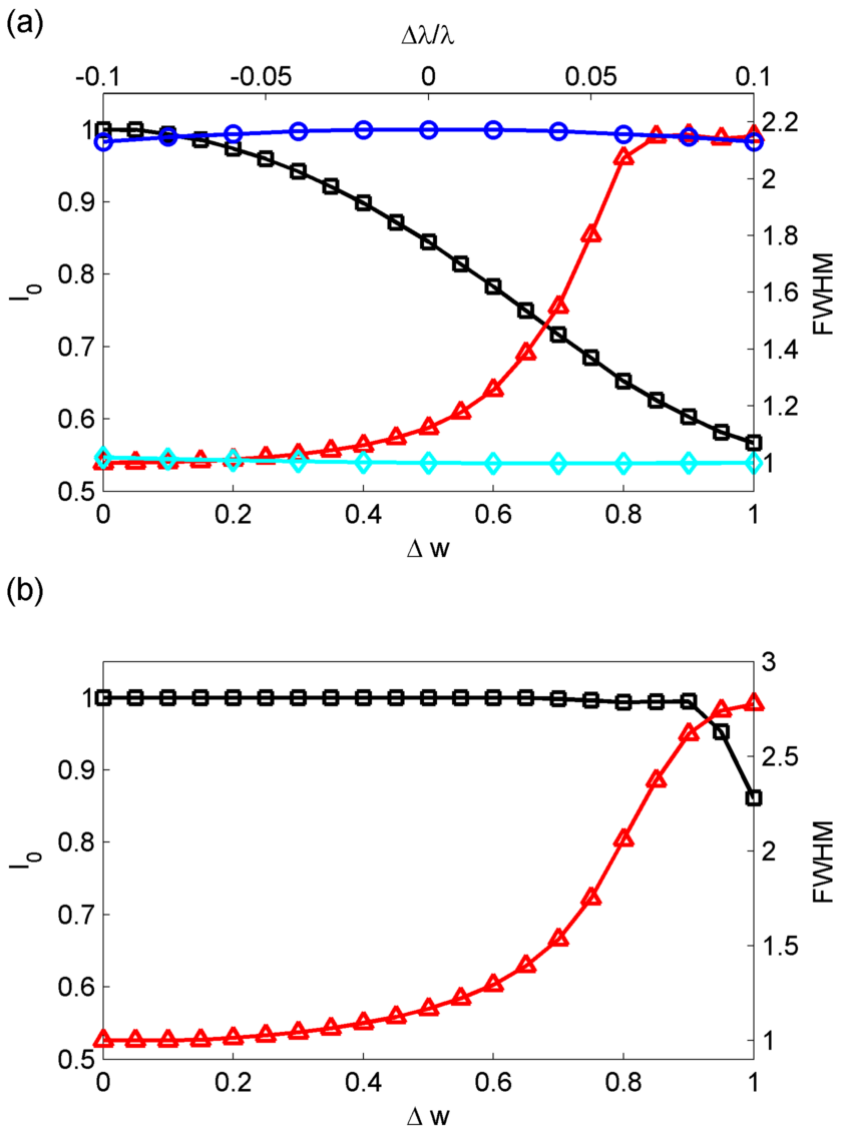

Figure 5-8. Characteristics of (a) SPP and (b) PMC errors – dip ratio I_0 ("□□□") and normalized FWHM ("ΔΔΔ") as a function of misalignment Δw. For the SPP, I_0 ("○○○") and FWHM ("◊◊◊") as a function of wavelength mismatch Δλ/λ is also plotted.

Similarly, for the PMC, the graph shows robustness to misalignment, with an increase in FWHM of 16% when Δw = 0.5 but only a decrease of less than 1% in I_0.

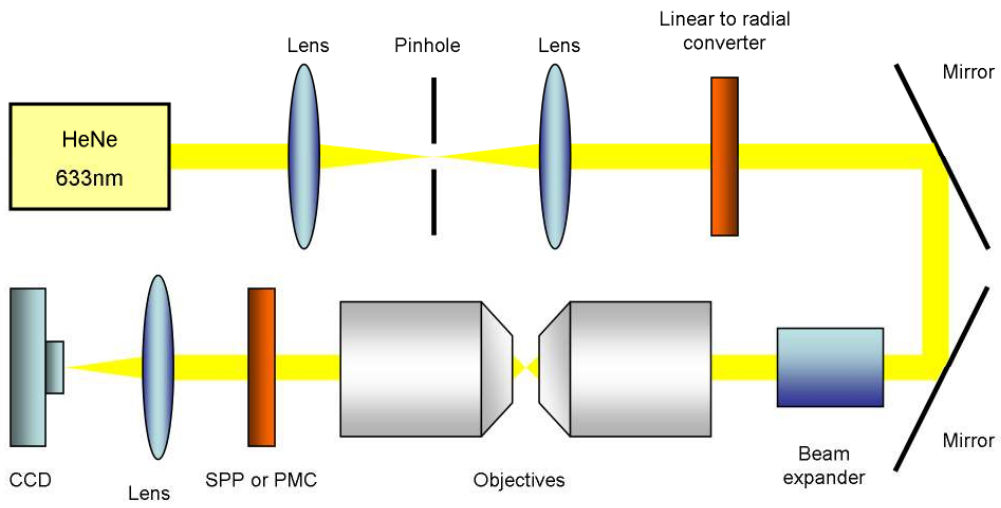

Figure 5-9. Experimental set-up to validate the effects of the spiral phase plate and the polarization mode converter.

5.3 Experimental Results

To verify that the proposed modification to SPCEM is workable and as a proof of concept, the following experiment was set-up in free space as shown in Figure 5-9. In this experimental set-up, a HeNe laser source with a wavelength of 632.8 nm was used as the excitation source. The TEM_{00} beam was passed through a linear polarizer and spatially filtered using a pinhole. Radially polarized light was subsequently obtained by passing the beam through a twisted nematic device consisting of a circularly rubbed plate and a π phase shifter (Arcoptix S.A, Switzerland) (Stalder and Schadt 1996) and then expanded 20 times with a beam expander to obtain a uniform illumination which fills up the back aperture of the objective lens. The objectives used in the set-up have a numerical aperture of 0.9 (UPlanSApo 40X 0.9NA, Olympus) and are infinity corrected. For the first test element, an SPP was placed

before the detector lens in the infinity corrected path in order to minimize aberrations. The SPP consists of a vortex microstructure patterned on a Polymethyl Methacrylate (PMMA) layer which was spin-coated on a glass substrate (RPC Photonics, Rochester). The transmission efficiency is greater than 80% and was designed with a center wavelength of 630 nm.

In this experiment, radially polarized was produced in order to replicate the effects of an axially oriented dipole. The results of passing the light through the SPP are shown in Figure 5-10. It is evident that without the SPP, the donut shape structure owing to the focusing of the radially polarized light onto the CCD is clearly seen in Figure 5-10(a). When an analyzer is placed in the light path in Figure 5-10(b)-(d), the resulting images display two lobes oriented in the direction of the analyzer (0º, 45º, 90º) as expected. With the addition of the SPP element, the result is a single lobe structure as predicted from theory (see Figure 5-10(e)). The analyzer images in Figure 5-10(f) to (h) show that the single lobe remains but is slightly elliptical in the direction of the analyzer axis. This is due to the fact that the field is still radially polarized in nature but has a helical wavefront superposed on it by the SPP element.

In another experiment, the PMC element was tested by utilizing a twisted nematic liquid crystal converter which converts from radial to linear polarization. This was placed in the infinity corrected path before the detector lens in order to minimize aberrations. Transmission efficiency of the device was about 70% in the visible range. The results are shown in Figure 5-11. As before, Figure 5-11(a) shows the donut structure and Figure 5-11(b)-(d) show the images when the analyzer is inserted. With the PMC element, Figure 5-11(e) shows that the result is a single lobe structure. The

cases with the inserted analyzer are shown in Figure 5-11(f)-(h). Because the PMC is oriented such that radially polarized light is converted to vertical polarization, it can be seen that Figure 5-11(f) has no discernible structure due to a horizontally oriented analyzer. In contrast, Figure 5-11(h) shows the same image as Figure 5-11(e) owing to the vertically oriented analyzer, while Figure 5-11(g) also shows a similar image but with a lower intensity as expected from a 45º analyzer.

It is verified that both the SPP and PMC elements are able to convert the donut shape structure to one with a single lobe. For the case of the SPP, the field is still radially polarized, but the superposed spiral phase enables constructive interference at the focus. In contrast, the PMC converts the radially polarized light to linearly polarized light which also results in constructive interference at the focus.

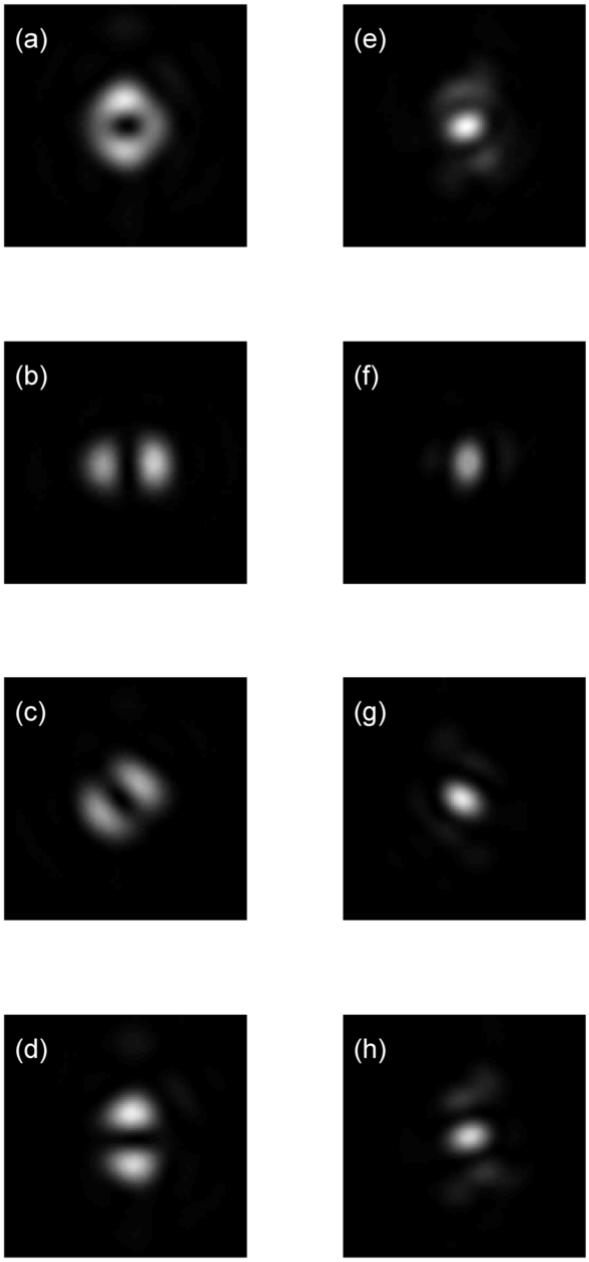

Figure 5-10. Experimental results for SPP: left panels - without spiral phase plate; right panels - with plate, (a),(e) images without analyzer, (b),(f) images with analyzer at 0º; (c),(g) at 45º and (d),(h) at 90º. Size of image is 3μm in both axes.

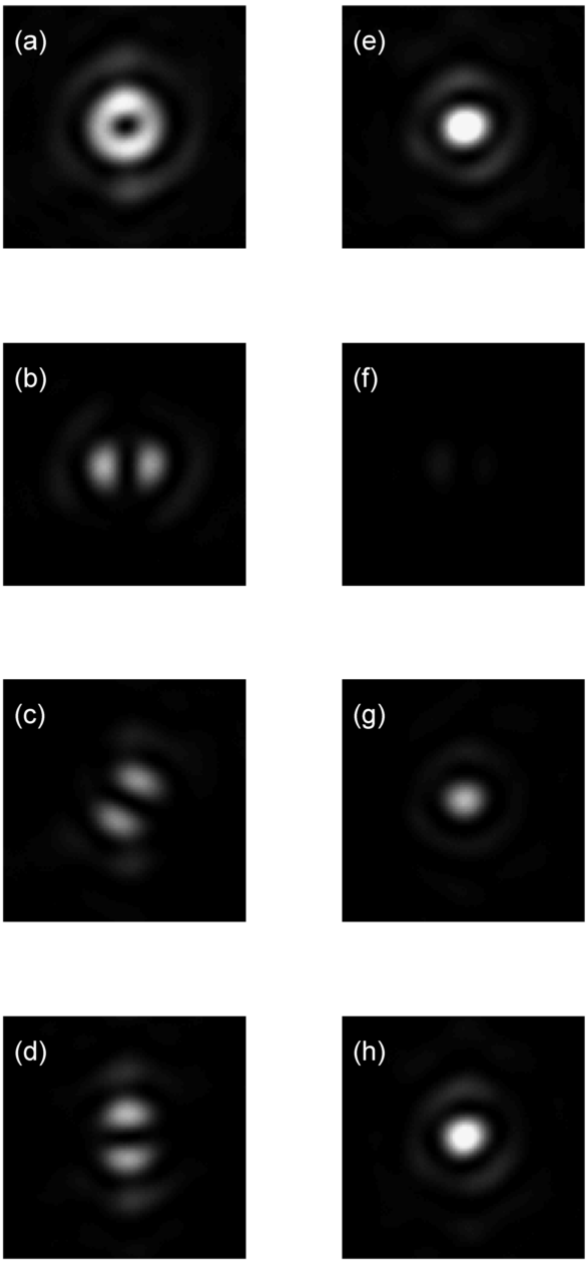

Figure 5-11. Experimental results for PMC: left panels - without polarization mode converter; right panels - with mode converter, (a),(e) images without analyzer, (b),(f) images with analyzer at 0º; (c),(g) at 45º and (d),(h) at 90º. Size of image is 3μm in both axes.

5.3.1 Modified SPCEM imaging

In this section, the proposed modification is applied to the actual SPCEM microscope and the effects are tested. In this experimental set-up, an inverted TIRF microscope (IX71, Olympus) was used with a high NA TIRF objective (Plan Apo 60X NA1.45). The excitation source was a solid state continuous-wave laser with a wavelength of 532 nm. For the first experiment, a transmission SPP with a designed center wavelength of 560 nm was inserted into the detection path before the imaging lens. Its transmission efficiency is greater than 80% and the wavelength design error is less than 10%. Fluorescent beads (F8792, Molecular Probes) with a nominal diameter of 40 nm were placed on a SiOx–Au (5 and 40 nm respectively) coated cover slip and imaged with a CCD (Retiga EXi, QImaging). Figure 5-12(a) and (c) show the simulated and experimental point spread functions of SPCEM without the SPP while Figure 5-12(b) and (d) show the point spread functions of the modified SPCEM with the SPP. Figure 5-12(e) and (f) plot the horizontal cross-sectional profiles of the point spread functions. In general, the experimental results show good agreement with the theoretical predictions. The morphology of the experimental point spread functions looks similar to the theoretical calculations. Furthermore, the simulations show a decrease in the FWHM from 437 nm to 193 nm, while the experimental point spread functions show a corresponding improvement from 456 nm to 217 nm, which translates to 2.1 times improvement in lateral resolution. The difference between simulation and experimental results can be attributed to the finite size of the fluorescent beads used in the experiments in contrast with the assumption of a point dipole in the theoretical model.

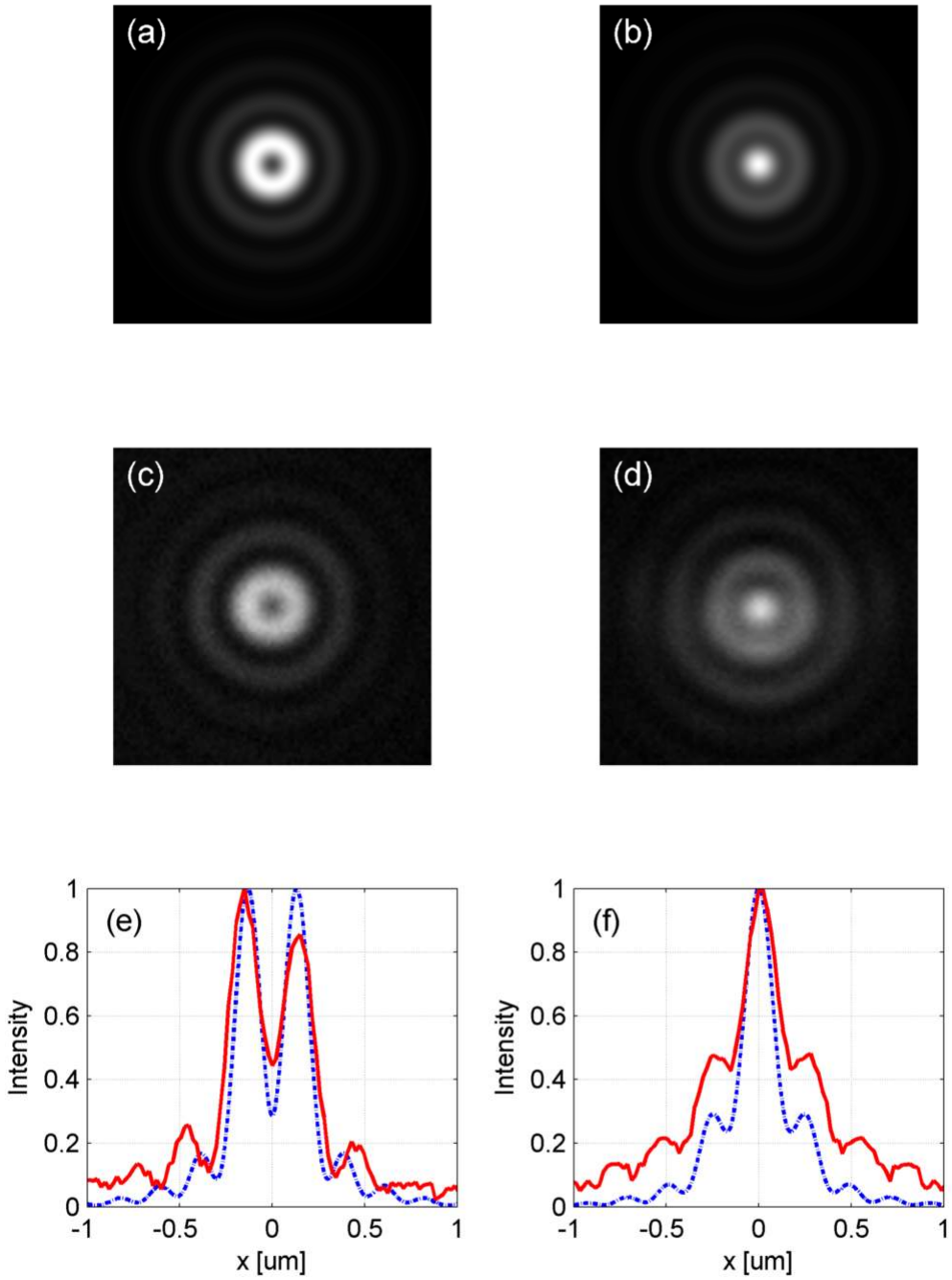

Figure 5-12. Comparison between simulation (dotted line) and experimental results (solid line). (a) Simulation without SPP (b) simulation with SPP (c) experimental result without SPP (d) experimental result with SPP (e) horizontal cross section without SPP (f) with SPP. Image scale is 2 μm by 2 μm.

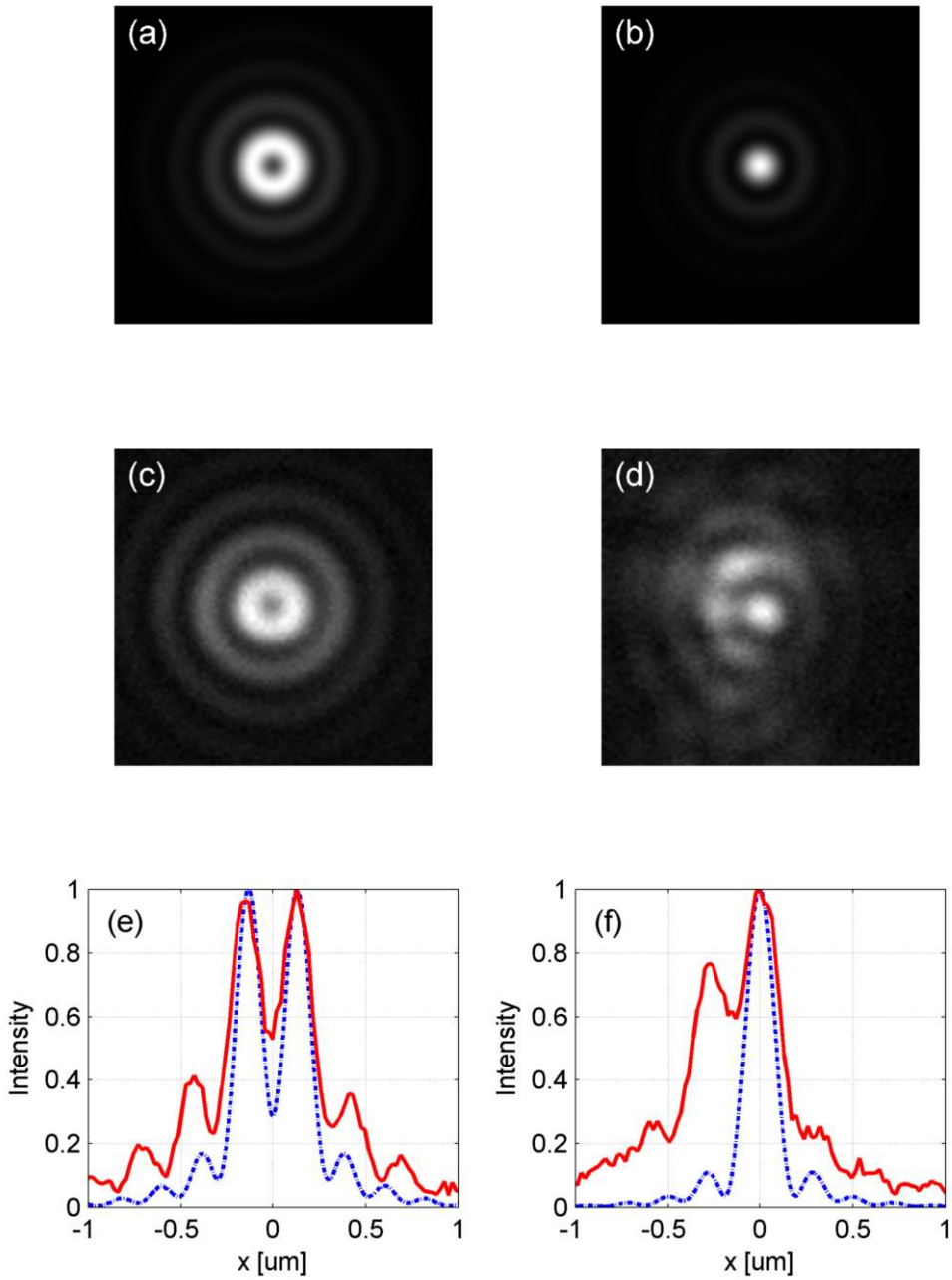

Figure 5-13. Comparison between simulation (dotted line) and experimental results (solid line). (a) Simulation without PMC (b) simulation with PMC (c) experimental result without PMC (d) experimental result with PMC (e) horizontal cross section without PMC (f) with PMC. Image scale is 2 μm by 2 μm.

For the second experiment, the SPP was replaced by a PMC element which was realized with a device consisting of a twisted nematic liquid crystal plate and a π phase shifter (Arcoptix, Switzerland). Figure 5-13(a) and (b) show the simulation results while Figure 5-13(c) and (d) show the experimental results. Figure 5-13(e) and (f) plot the horizontal profile of the point spread functions. In general after adding the PMC element, the morphology in Figure 5-13(d) resembles the simulation in Figure 5-13(b). However, the point spread function is still not as symmetric as the case where SPP was used. This is because the actual PMC device is made from two liquid crystal plates which are spaced a few millimeters apart. Diffraction between the two elements causes the 180 degrees phase compensation to be non-ideal, thus resulting in certain areas where the radial to linear polarization conversion becomes incomplete. This can be observed in Figure 5-13(d) where the second ring has some asymmetric bright areas. A PMC device based on segmented waveplates (Nanophoton Corp. 2010) is expected to give a better result. In general, while the PMC element should give smaller sidelobes compared to the SPP element, the SPP is usually a better choice in practice because it does not require handling of complicated polarization optics in the detection path and thus tends to give better results more easily than with the PMC. Furthermore, the cost of fabricating the SPP is considerably cheaper than the PMC.

In the next experiment, we image and compare the effects of the SPP element on HeLa cells. The HeLa cells were cultured on the Au-SiO_2 coated cover slips placed in 100 mm Petri dishes with the Dulbecco's modified Eagle's medium (DMEM) supplemented with 10% fetal bovine serum and penicillin-streptomycin (100 units of penicillin per ml media, and 100 μg streptomycin per ml media). The cells were

cultured at 37˚C in 5% CO_2.When the cell confluency reached ~60%, they were then

(a)

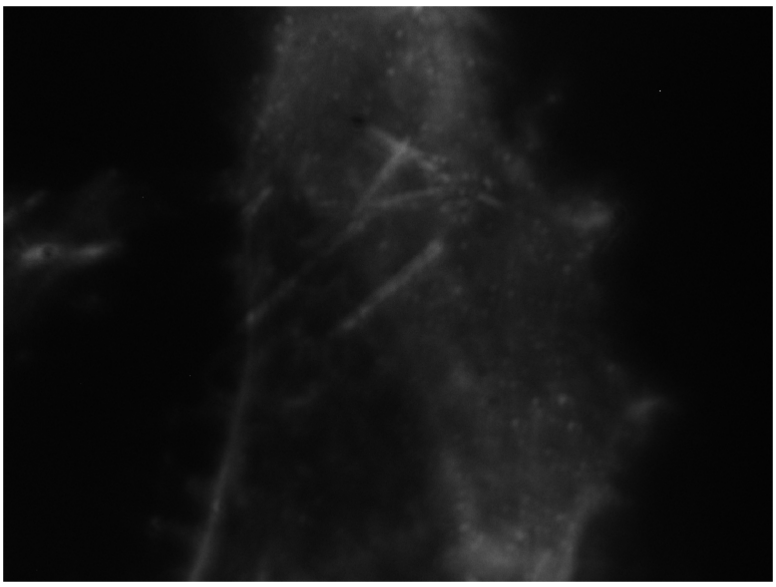

(b)

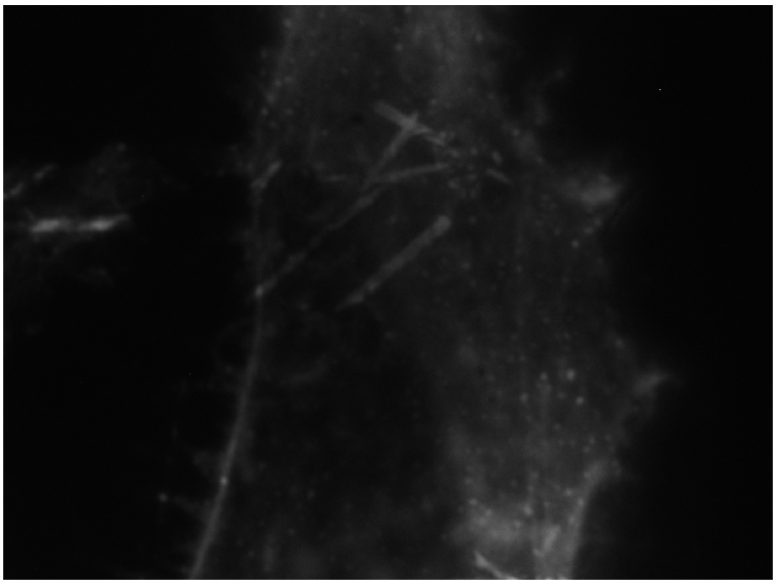

Figure 5-14. SPCEM images of AlexFluor 532 labeled HeLa cells (a) without SPP (b) with SPP. Size of image is 33 μm by 24 μm.

washed twice with phosphate buffered saline solution and fixed with 4% formaldehyde at room temperature. For F-actin labeling, the cells were then incubated with 165 nM AlexaFluor 532 phalloidin for 20 minutes and washed three times with distilled water. Finally the cover slip was sealed onto a glass slide after the cells were dried. Figure 5-14 shows the pictures of the cells imaged without the SPP and with the SPP. With the SPP element, it can be observed qualitatively in Figure 5-14(b) that the image resolution is improved as compared to that when the SPP is not used.

In summary, in any imaging system, it is important to ensure that the imaging point spread function has a proper form. To our knowledge, this is the first demonstration of optical conversion of the donut SPCEM point spread function into one which is single lobed with the use of either a spiral phase plate or a polarization mode converter. The vectorial OTF of the system was calculated and fully characterized for both cases, and the resolution is shown to improve by a factor of two. The SPP is preferred over the PMC due to simplicity and cheaper cost even though the sidelobes are stronger. In general, both methods are robust to misalignment as well as wavelength mismatch. It is envisaged that these methods will be beneficial to the application of SPCE imaging without requiring the use of imprecise numerical restoration techniques. In the next chapter, a high resolution method of SPCEM imaging is developed.

CHAPTER 6: STANDING-WAVE SURFACE PLASMON-COUPLED EMISSION MICROSCOPY

Surface plasmon-coupled emission microscopy suffers from poor resolution when compared to TIRF microscopy due to an enlarged point spread function. In addition to using numerical deconvolution as a method to enhance the images, or using optical means to compensate for the irregular point spread function, the resolution can also be increased beyond the diffraction limit by making use of two counter-propagating waves to form a standing wave pattern to illuminate the fluorescent sample. In this chapter, sub-diffraction imaging using standing-wave surface plasmon resonance for exciting fluorophores (SW-SPRF) is developed to provide better imaging resolution. SW-SPRF operates in wide-field and can provide a lateral resolution of $\lambda/4$.

6.1 Background

The concept of a perfect lens realized with negative refractive index materials was proposed by Pendry (Pendry 2000). It was shown that surface plasmon resonance which is a resonant energy transfer from incident photons to electron density

oscillations along a metal-dielectric interface can help to enhance the weak evanescent waves, which essentially carry the high spatial frequency information, thereby improving the imaging resolution. However, a limitation of this approach is that the detection must be done in the near-field (Fang et al. 2005). Nevertheless, recent work demonstrated that far-field detection is also possible with periodic corrugations in the metal layer (Fang et al. 2005), and that image magnification can similarly be achieved (Liu et al. 2007; Smolyaninov et al. 2007). While super-resolution on the order of $\lambda/4$ has been demonstrated with these methods, the disadvantage is that they all require the substrate to be specially fabricated and furthermore, the sample needs to be placed at specific locations of the substrate. For example to provide image magnification, thin gold sheets are arranged in semi-cylindrical layers and the sample is placed in the innermost layer (Liu et al. 2007).

Therefore, another sub-diffraction imaging method needs to be developed. By using the standing-wave of surface plasmon resonance, a fluorescence imaging method called SW-SPRF is developed that has the advantage of enhanced contrast. Furthermore, the SW-SPRF method operates in wide-field, without the need of complex substrate fabrication. As opposed to normal surface plasmon imaging as well as the compensated surface plasmon imaging, the SW-SPRF method is able to provide a lateral resolution approaching the sub-diffraction limit of $\lambda/4$.

6.2 Theory

SW-SPRF is based on the concept similar to that of standing-wave TIRF (SW-TIRF) (Chung et al. 2007; So et al. 2001). In one-dimensional SW-TIRF, an evanescent

standing wave pattern is used to illuminate the sample, and three images are captured each with a differing phase difference. Reconstruction with the SW-TIRF algorithm on the three captured images results in a single image with increased resolution in one dimension. It is noted that this method is similar to the structured illumination technique used in conventional microscopy (Lukosz 1966; Neil et al. 1997). While normal wide-field fluorescence microscopy gives a resolution of λ/2NA, SW-TIRF can provide an enhanced resolution of about λ/4NA, which is a two times improvement. Similarly in SW-SPRF, an evanescent standing surface plasmon wave can be set up to excite the fluorescent sample. Apart from increased resolution, advantages of this method are the improved excitation efficiency, better signal contrast and reduced photobleaching due to decreased fluorescence lifetime.

The concept of SW-SPRF can be understood mathematically. For simplicity, consider only one dimension. The image in a microscope can be expressed as a convolution between a fluorescent sample excited by a patterned illumination field and the system point spread function. If the excitation field $E(x)$ is assumed to contain high spatial frequencies and is translatable, the captured image takes the form

$$I(x,x') = \left[O(x)E(x-x')\right] \otimes P(x) \tag{6.1}$$

where x' denotes a translation shift of the excitation field, $O(x)$ is the fluorescent object and $P(x)$ is the system response. By synthesizing a new image as a weighted sum of images captured with differing translations, the final image is

$$I'(x) = \sum_{\{x'\}} f(x,x')I(x,x') \tag{6.2}$$

where $f(x,x')$ denotes the weights. Provided that the weights together with the excitation field satisfy the condition

$$\sum_{\{x'\}} f(x,x')E(x''-x') = E(x-x''), \tag{6.3}$$

then the synthesized image can be simplified into

$$I'(x) = O(x) \otimes \left[E(x)P(x)\right]. \tag{6.4}$$

The synthesized image is thus expressed as the convolution between the fluorescent object and an effective point spread function $E(x)P(x)$.

Conceptually, the standing wave technique can be understood pictorially as shown in Figure 6-1. Here when uniform illumination is used to excite the sample, the two objects which are spaced closely just below the diffraction limit cannot be discriminated due to the limited resolution. However, with the standing-wave illumination, the first object is "probed" by the standing-wave pattern. Subsequently, when the phase is sequentially changed to translate the illumination pattern, the second object can be detected in the third image. These three images are then synthesized together to give a final high resolution image which can discriminate the two closely spaced objects. In this way, the standing-wave technique gives an improvement in resolution over the conventional uniform illumination method.

The improvement in resolution can also be understood in the Fourier domain, where the OTF which is $\tilde{E}(f) \otimes \tilde{P}(f)$ implies that the support of the original point spread function $\tilde{P}(f)$ has been enlarged since the excitation field $\tilde{E}(f)$ has a finite bandwidth. It can also be realized from this expression that due to the diffraction-limited nature of light, the maximum improvement that can be made to the resolution

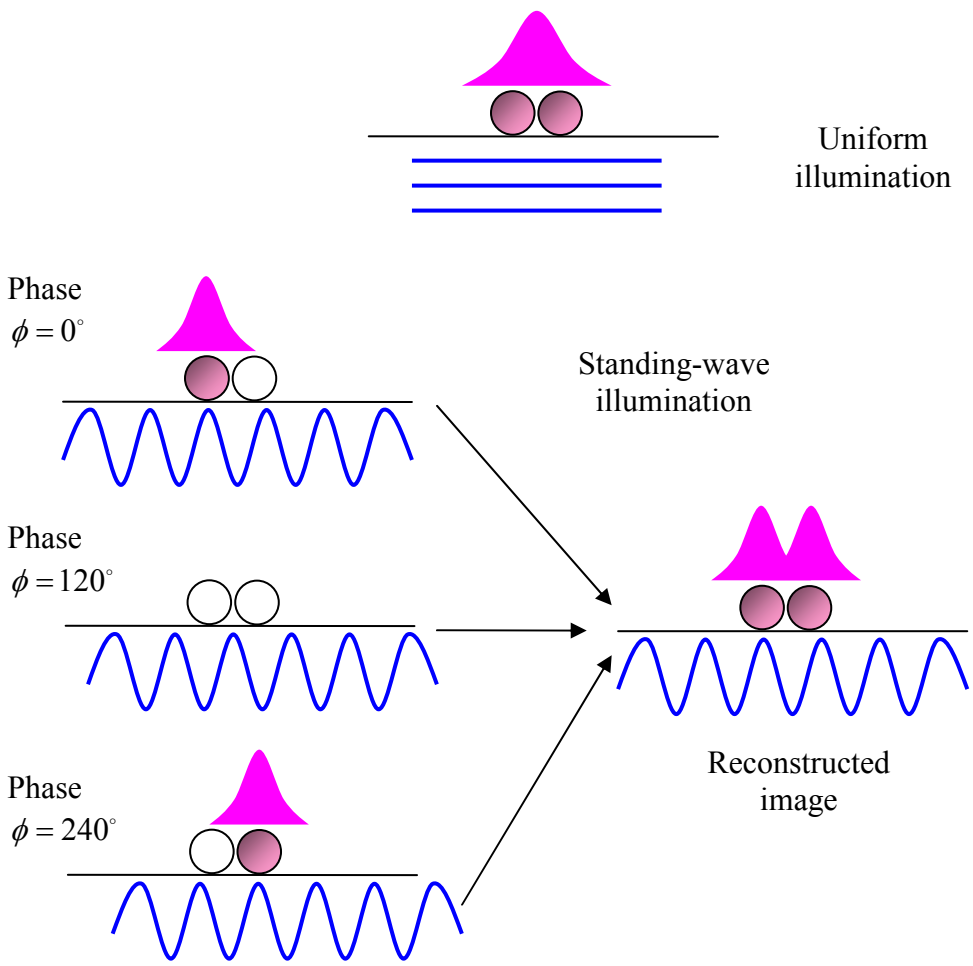

Figure 6-1. Schematic diagram of using standing-wave excitation with three different phases to reconstruct the high resolution image which is able to discriminate two objects spaced closely, unlike with uniform illumination which is unable to discriminate them.

of the system with a linear excitation field is a factor of two times increase over the conventional system. For the one-dimensional case, the excitation field for a standing wave takes the form of $E(x) = 1 + \cos(Kx)$ where K is the spatial wave number given by $K = 4\pi n \sin\theta / \lambda$, and n and θ denote the refractive index of the medium and the angle of incidence respectively. The minimum number of images required to

synthesize the high resolution image is three and correspondingly the set of translations or phase shifts used can be $\left\{0, \frac{2\pi}{3}, \frac{4\pi}{3}\right\}$ (So et al. 2001).

6.2.1 Creating standing wave with *p*-polarized light

Unlike SW-TIRF which uses *s*-polarized incident light, SW-SPRF uses *p*-polarized incident light because *p*-polarization is required to excite surface plasmons. A comparison can be made between the *s*- and *p*-polarized light used respectively by SW-TIRF and SW-SPRF. In TIRF, the *s*-polarized incident light is given by

$$\mathbf{E}_{\mathbf{s,i}} = \begin{bmatrix} 0 \\ 1 \\ 0 \end{bmatrix} \exp\left(ik_i x \sin\theta_i + ik_i z \cos\theta_i\right), \tag{6.5}$$

where k_i is the wave number and θ_i is the angle of incidence. The transmission field at the interface is expressed as

$$\mathbf{E}_{\mathbf{s,t}} = t_s \begin{bmatrix} 0 \\ 1 \\ 0 \end{bmatrix} \exp\left(ik_i x \sin\theta_i\right) \exp\left(-k_i z \sqrt{\sin^2\theta_i - \eta^2}\right), \tag{6.6}$$

where t_s denotes the Fresnel coefficient for *s*-polarized light and $\eta = n_t / n_i$. Therefore in SW-TIRF, with two counter-propagating beams at the same angle of incidence, the field at the interface becomes

$$\mathbf{E}_{\mathbf{s,t}}^{\mathbf{sw}} = t_s \begin{bmatrix} 0 \\ 1 \\ 0 \end{bmatrix} \left[\exp\left(ik_i x \sin\theta_i\right) + \exp\left(-ik_i x \sin\theta_i\right) \right] \exp\left(-k_i z \sqrt{\sin^2\theta_i - \eta^2}\right)$$
$$= 2t_s \begin{bmatrix} 0 \\ 1 \\ 0 \end{bmatrix} \cos\left(k_i x \sin\theta_i\right) \exp\left(-k_i z \sqrt{\sin^2\theta_i - \eta^2}\right). \tag{6.7}$$

The intensity is thus

$$I_{s,t}^{sw} == 2\left|t_s\right|^2 \left(1 + \cos\left(2k_i x \sin\theta_i\right)\right) \exp\left(-2k_i z \sqrt{\sin^2\theta_i - \eta^2}\right). \tag{6.8}$$

Similarly, for a *p*-polarized incident beam in SW-SPRF, its field is given as

$$\mathbf{E}_{\mathbf{p,i}} = \begin{bmatrix} -\cos\theta_i \\ 0 \\ \sin\theta_i \end{bmatrix} \exp\left(ik_i x \sin\theta_i + ik_i z \cos\theta_i\right), \tag{6.9}$$

and at the interface the transmitted field is

$$\mathbf{E}_{\mathbf{p,t}} = \frac{t_p}{\eta} \begin{bmatrix} -i\sqrt{\sin^2\theta_i - \eta^2} \\ 0 \\ \sin\theta_i \end{bmatrix} \exp\left(ik_i x \sin\theta_i\right) \exp\left(-k_i z \sqrt{\sin^2\theta_i - \eta^2}\right). \tag{6.10}$$

Hence for two counter-propagating *p*-polarized beams with the same angle of incidence, the field at the interface is

$$\mathbf{E}_{\mathbf{p,t}}^{\mathbf{sw}} = \frac{t_p}{\eta}\left\{\begin{array}{l}\begin{bmatrix} -i\sqrt{\sin^2\theta_i - \eta^2} \\ 0 \\ \sin\theta_i \end{bmatrix}\exp\left(ik_i x\sin\theta_i\right) \\ +\begin{bmatrix} i\sqrt{\sin^2\theta_i - \eta^2} \\ 0 \\ \sin\theta_i \end{bmatrix}\exp\left(-ik_i x\sin\theta_i\right)\end{array}\right\}\times\exp\left(-k_i z\sqrt{\sin^2\theta_i - \eta^2}\right)$$

$$= \frac{2t_p}{\eta}\begin{bmatrix} \sqrt{\sin^2\theta_i - \eta^2}\,\sin\left(k_i x\sin\theta_i\right) \\ 0 \\ \sin\theta_i\cos\left(k_i x\sin\theta_i\right) \end{bmatrix}\exp\left(-k_i z\sqrt{\sin^2\theta_i - \eta^2}\right) \tag{6.11}$$

and the intensity is therefore expressed as

$$I_{s,t}^{sw} = 2\left|\frac{t_p}{\eta}\right|^2\left(2\sin^2\theta_i - \eta^2\right)\left(1 + \frac{\eta^2}{2\sin^2\theta_i - \eta^2}\cos\left(2k_i x\sin\theta_i\right)\right) \times\exp\left(-2k_i z\sqrt{\sin^2\theta_i - \eta^2}\right). \tag{6.12}$$

Figure 6-2 shows the intensity of the standing wave pattern for *s*-polarized SW-TIRF and *p*-polarized SW-SPRF near the metal surface. For comparison purposes, both of the counter-propagating incident beams for the two cases are set at an angle of 45º to the normal at the interface. Both the SW-TIRF and SW-SPRF excitation fields show a sinusoidal standing wave pattern which decays exponentially with increasing distance away from the surface, but with the SW-SPRF case showing a higher intensity and whose peak is about three times more than that of SW-TIRF.

Another factor to note is that due to the use of *p*-polarized light by SW-SPRF in contrast to the *s*-polarized beam in SW-TIRF, the contrast of the standing wave pattern is not constant and can vary with the angle of incidence of the incoming light. This can be seen by comparing their intensity equations in Equation (6.8) and

Equation (6.12). For SW-TIRF, which uses *s*-polarized light, the contrast of the standing-wave is always equal to 1, meaning that the contrast is always maximum. However with SW-SPRF, due to the *p*-polarized beam, the contrast of the standing-wave which is given as $\eta^2 / \left(2\sin^2\theta_i - \eta^2\right)$, is a function of the angle of incidence and

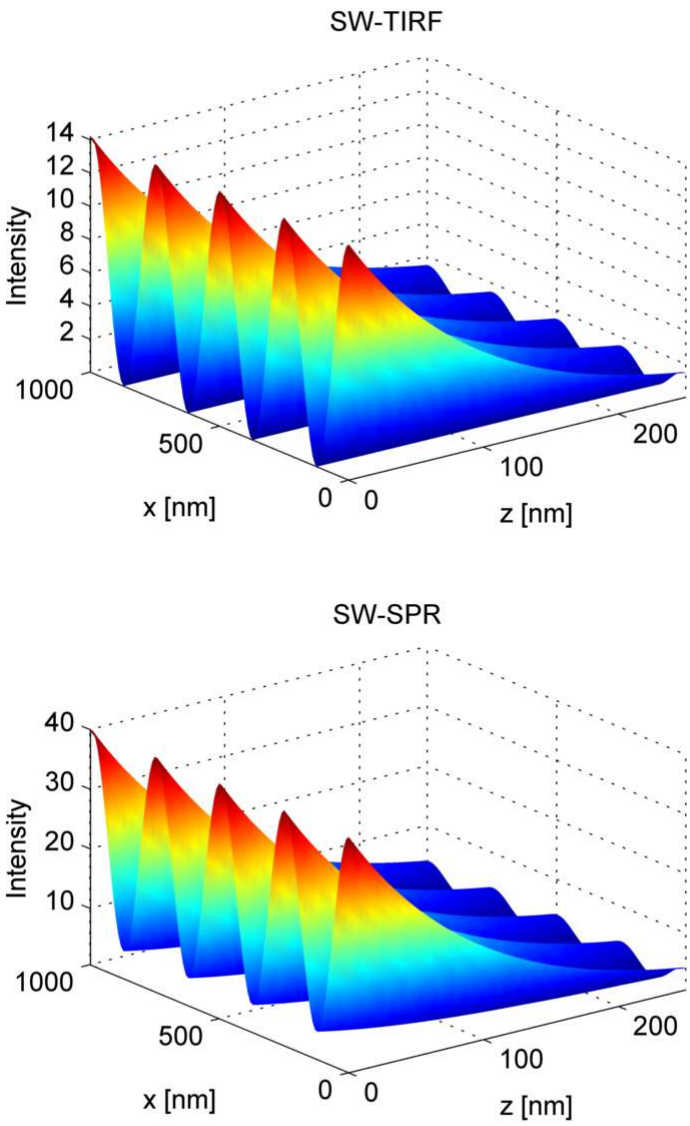

Figure 6-2. Standing wave pattern for SW-TIRF and SW-SPRF with incident beam set at 45º to the normal.

the refractive indices of the media. Figure 6-3 shows how the contrast ratio of the standing-wave varies when the angle of incidence is changed. Two plots are shown, one assuming that the immersion medium has a refractive index of 1.515 and the second assuming an index of 1.78. The sample is assumed to be placed in air or water.

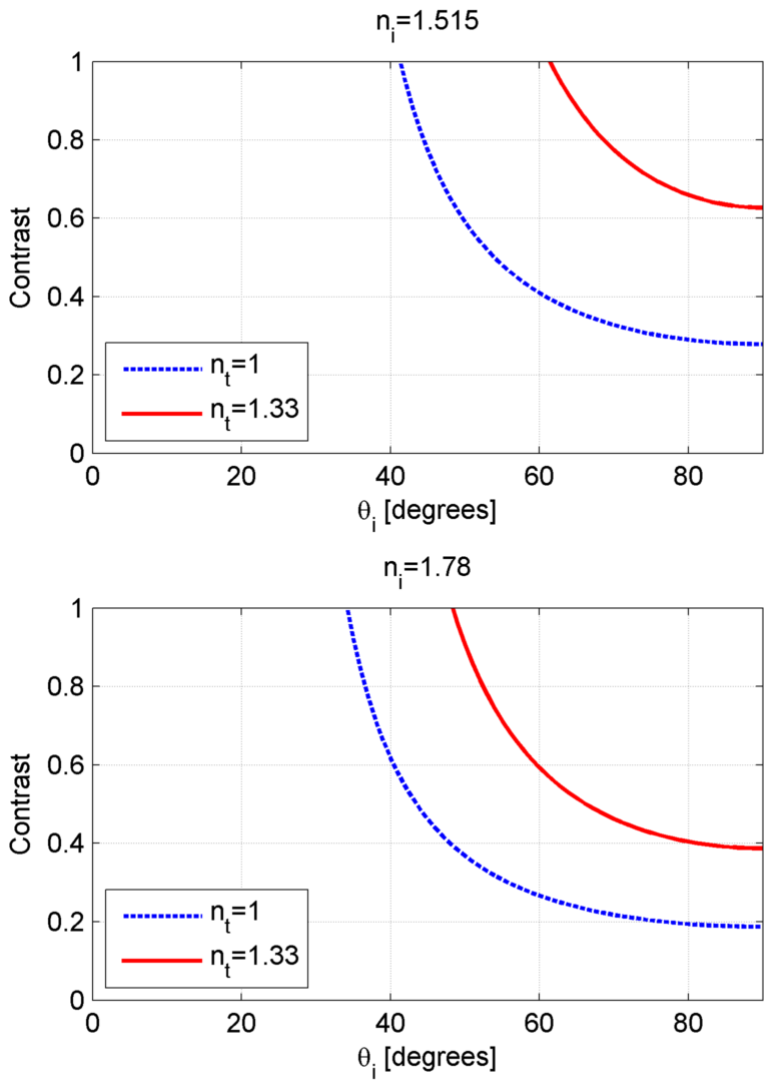

Figure 6-3. Constrast of *p*-polarized standing wave in SW-SPRF for sample medium having refractive index 1 (air, dotted line) or 1.33 (water, solid line). Immersion medium is assumed to have refractive index of 1.515 (top) or 1.78 (bottom).

If the sample is in air, the graph shows that just above the critical angle, the contrast is a maximum. However with increasing angle, the contrast starts to decrease and reaches a minimum at 90 degrees. In SW-SPRF if a gold metal layer is used and the index of the immersion medium is 1.515, the surface plasmon resonance angle is about 45 degrees, which gives a contrast close to 0.8.

6.2.2 SW-SPRF algorithm and resolution

Due to the donut point spread function of SPCEM, the standing-wave algorithm cannot be applied directly to the SPCEM images without modification. The consequence when the algorithm is applied directly without modification is the enlargement of the effective point spread function as shown in Chatper 3. The

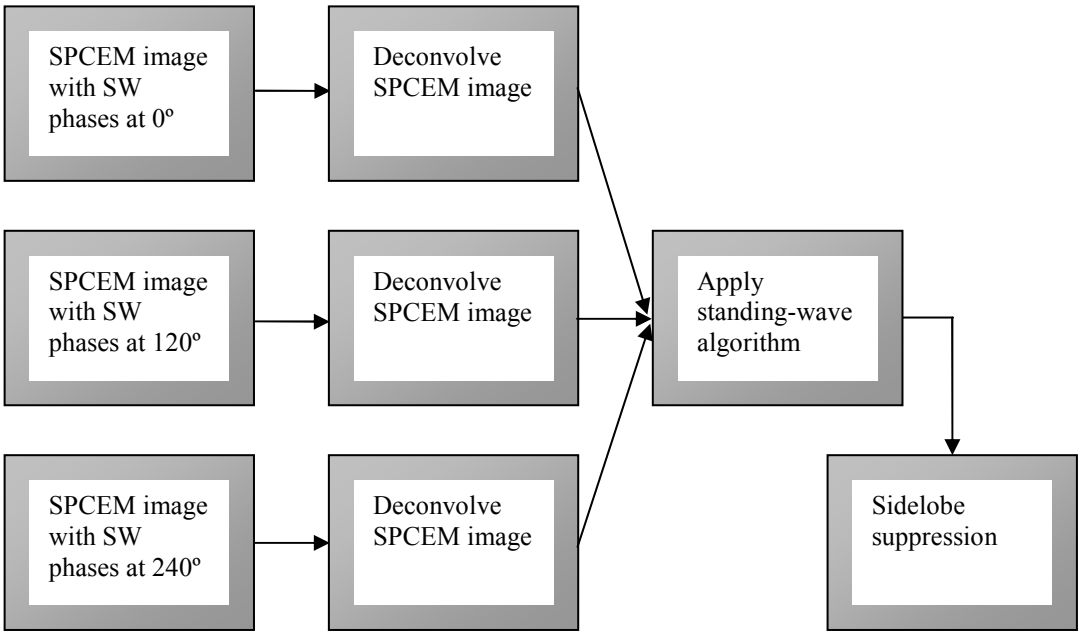

Figure 6-4. Modified standing-wave algorithm with deconvolution as an intermediate step.

proposed modified standing-wave algorithm for SW-SPRF is shown in Figure 6-4 which includes an additional step of compensating for the donut point spread function of SPCEM. For proof of concept, the Richardson-Lucy deconvolution technique is used in this study, although in general the compensation need not be limited to deconvolution and can include optical methods such as the spiral phase plate method described in the previous chapter.

The second intermediate step of compensating for the central dip in the donut-shape point spread function is crucial for the whole process. Otherwise, the reconstruction will lead to a final distorted point spread function with an increased FWHM. This distortion is shown in Figure 6-5 where the final point spread functions without and with deconvolution are simulated. Without the deconvolution step in the algorithm, it is observed that there exists significant distortion to the point spread function. In addition, the FWHM is increased by 16% from the original SPCEM FWHM of 426 nm to 494 nm. With the addition of the intermediate deconvolution step to the standing-wave algorithm, it can be seen that the point spread function becomes a single lobe and the improvement in the FWHM is about four times or a reduction of about 73% compared with that of SPCEM. This FWHM is 40% smaller than the diffraction limited FWHM of 193 nm assuming an emission wavelength of 560 nm and an objective NA of 1.45.

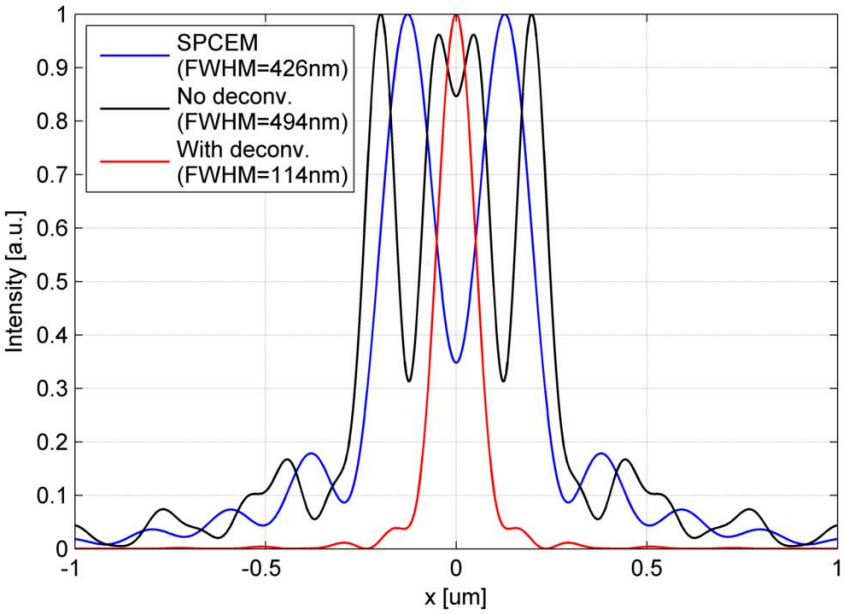

Figure 6-5. Simulation of point spread function without and with deconvolution as an intermediate step to compensate for the donut-shape point spread function of SPCEM.

6.3 Experimental Results

6.3.1 SW-SPRF set-up

A schematic of the SW-SPRF microscope set-up is shown in Figure 6-6. Such a set-up employs the surface plasmon-coupled emission (SPCE) phenomenon (Borejdo, Z. Gryczynski, et al. 2006; Burghardt et al. 2006; Tang et al. 2007). It dispenses with the traditional Kretschmann-Raether prism-based configuration and simplifies overall system design. Furthermore, the advantages of using SPCE include better background suppression, smaller detection volume, and decreased fluorescence lifetime and photobleaching. The excitation light used was a continuous-wave laser with a wavelength of 532 nm (Verdi-10, Coherent) which was isolated from the optical table to minimize vibration. The laser light was coupled into a single-mode polarization-

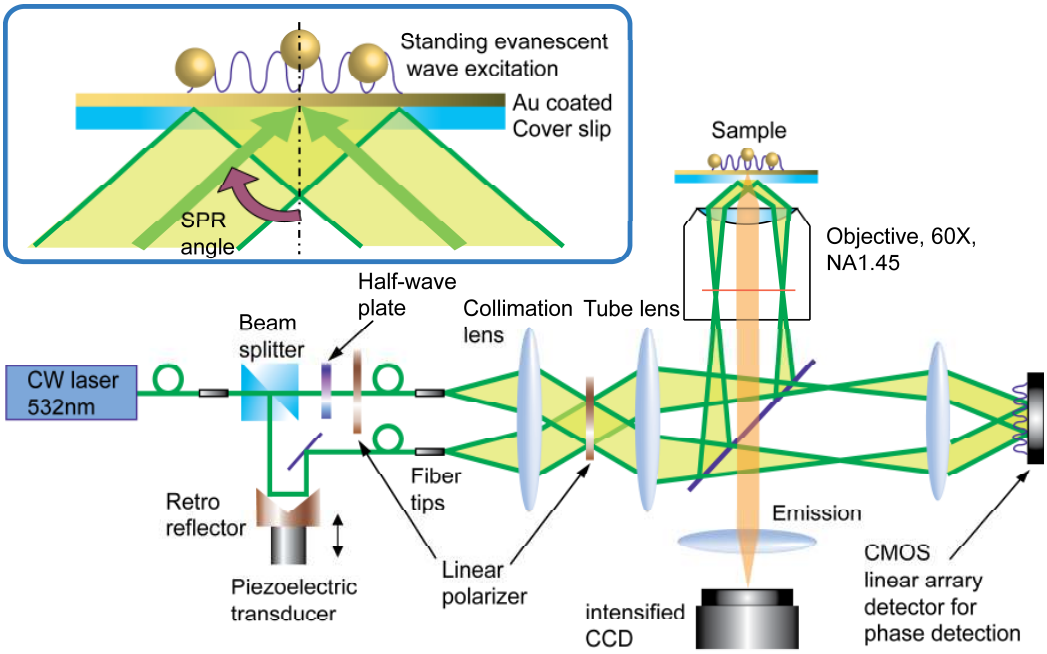

Figure 6-6. Schematic diagram of the experimental set-up of standing-wave surface plasmon resonance fluorescence microscopy.

maintaining fiber (OZ Optics, Otawa) and directed to enter a 50:50 beam splitter. In one of the beam paths, a retro-reflector mirror with a piezo-actuated transducer was inserted so that the optical path difference can be varied to control the phase difference between the two beams. Each of the beams was coupled into a single-mode fiber and directed out through a collimation lens, reflected by a dichroic mirror (z532dc, Chroma) and then focused at the back aperture of a high NA objective lens (PlanApo NA1.45 60X, Olympus). A linear polarizer between the collimation lens and the tube lens can select either *s*- or *p*-polarized illumination. The fiber tips were mounted on a precise translational stage so that the lateral translation transforms into a change in the incident angle of the beams. The angle of incidence can be adjusted over a range of 41.2º to 72.5º.

In the configuration, the angles of incidence of both beams were fixed at the SPR angle of 45° to excite surface plasmons. The counter-propagating plane waves propagating out of the high NA objective met at the interface and resulted in surface plasmon waves on the metal surface which interfered and excited fluorophores on the metal surface. For the substrate, a thin gold film (40 ± 2.3 nm) was prepared on coverslips by vapor deposition. The gold film was covered with a layer of silica (SiOx, 5 nm) to minimize quenching. Thickness of the film was confirmed by AFM (Dimension 3100, Veeco) and ellipsometry (M-2000, J.A. Woollam Co.). The prepared sample consisted of a diluted solution of sub-diffraction size fluorescent beads (diameter 0.04 μm; Molecular Probes, OR) spread on the gold-coated coverslip and dried overnight. The fluorescent sample on the gold-coated coverslip was excited by the surface plasmon standing wave and emitted at a longer wavelength. The emission light was then collected back via the same high NA objective lens. The image was then collected by a tube lens and focused on to an intensified CCD camera (Pentamax, Princeton Instrument, New Jersey). For each image, the phase of the standing wave was controlled by a feedback control system that was functional with *p*-polarized standing wave.

Recalling that due to electromagnetic boundary conditions, surface plasmons can only be excited by *p*-polarized illumination, and unlike typical total internal reflection fluorescence illumination with *s*-polarization where the contrast ratio is 1 for all incident angles and is independent of the refractive indices of the medium, it is noted that the *p*-polarized SPR illumination results in a contrast ratio which is a function of the incident angle and the refractive indices as discussed previously. Thus,

it is important to ensure that the set-up operates at a higher ratio in order to improve image contrast. For gold at the SPR angle of 45°, the contrast ratio was close to 0.8 which provides sufficient contrast for illumination.

The processes in generating extended-resolution images with SW-SPRF in the vertical direction are shown in Figure 6-7. As mentioned, due to the unique donut-shape point-spread function of using surface plasmons in SPCEM, there exists a central dip in the point spread function and the overall FWHM becomes widened as a result of the donut shape. A non-linear deconvolution algorithm was applied to convert the donut-shape point spread function in Figure 6-7(a) into a more conventional Airy disk shape as shown in Figure 6-7(b). Based on the numerical model of the SPCEM point spread function, the Richardson-Lucy deconvolution algorithm was used with the theoretical point spread function kernel as an input. To generate a SW-SPRF image, three SPCEM images were taken at three standing-wave phases (0, $2\pi/3$, and $4\pi/3$). One representative image is shown in Figure 6-7(a). The vertical profile (in the y direction) shows that resolution of SPCEM is poor with a FWHM of 485 nm. The deviation from the simulated SPCEM resolution of 426 nm is attributed to the point dipole used in the model while the actual beads have a nominal diameter of 40 nm.

The deconvolution algorithm was then applied to each of the three images to convert their original donut-shape point spread function into one that is single-lobed as shown in Figure 6-7(b) where the FWHM after deconvolution has been improved to 310 nm. This was followed by the application of the standing-wave algorithm on the three images to synthesize a single high-resolution image (So et al. 2001). The

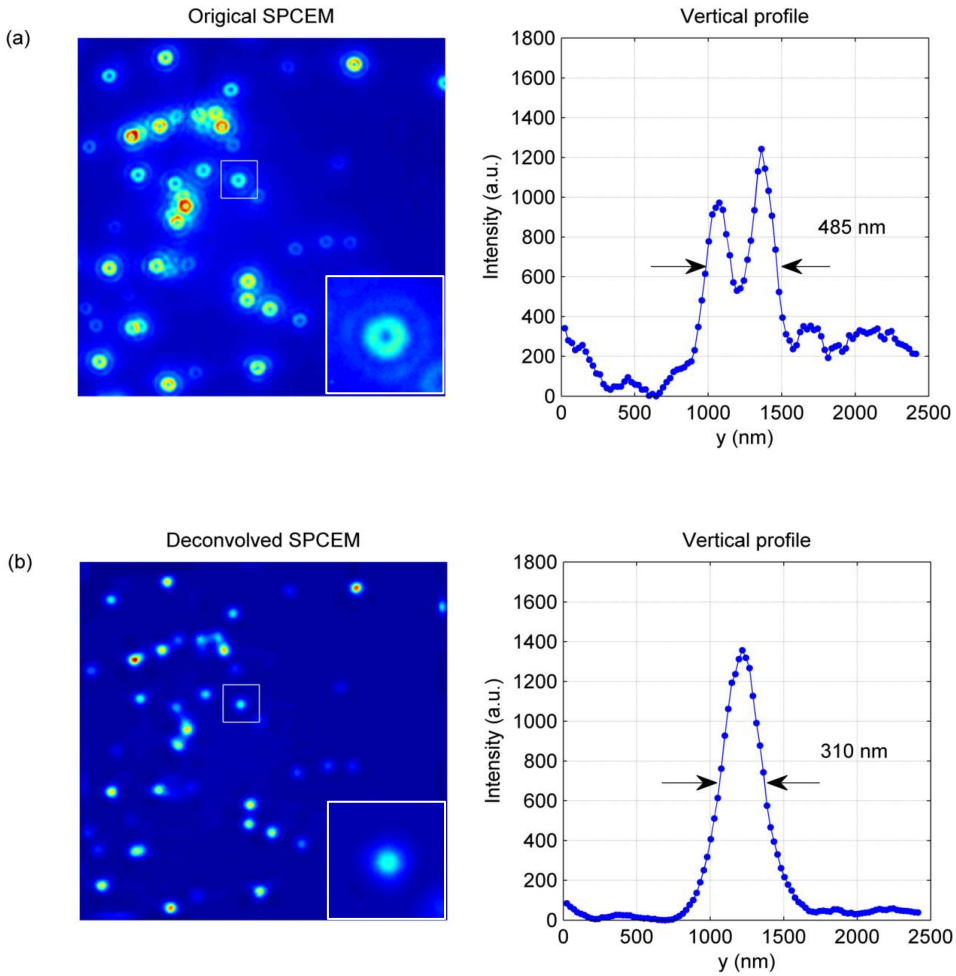

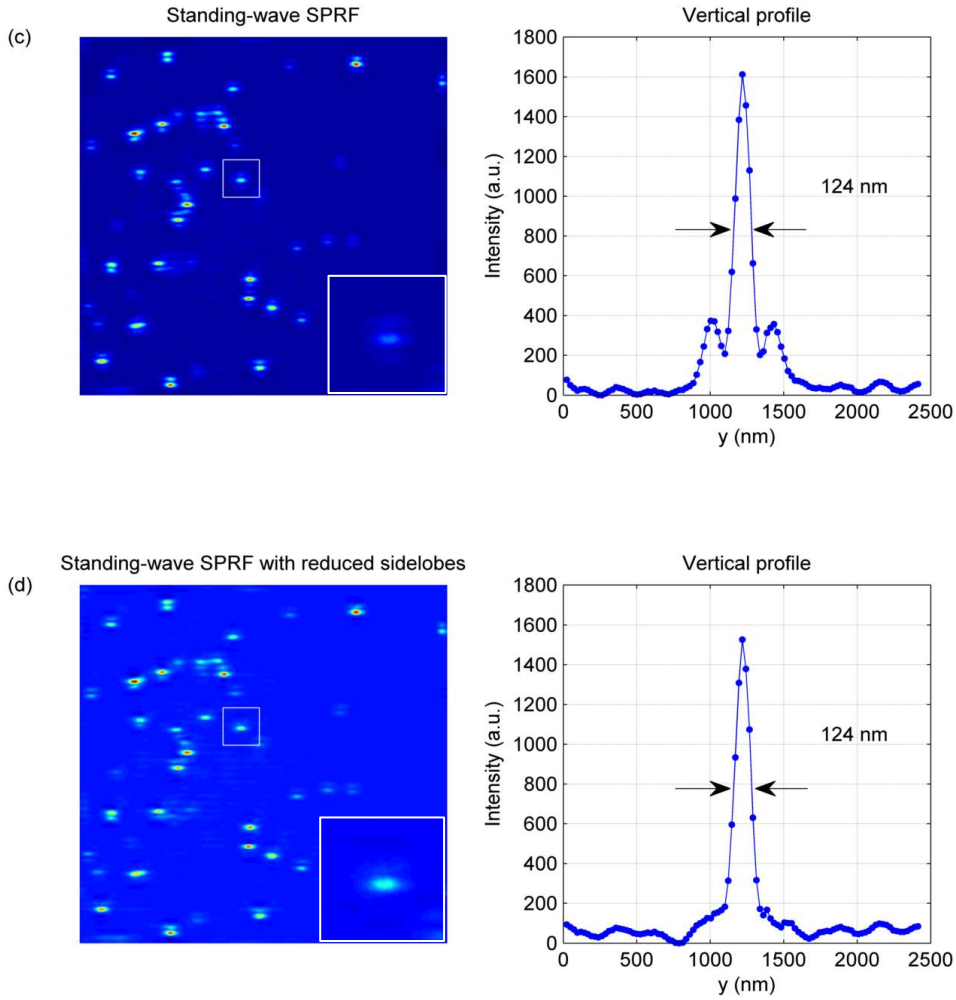

Figure 6-7. Extended-resolution imaging with standing-wave surface plasmon resonance fluorescence (SW-SPRF) microscopy in vertical direction (a) original SPCEM image with donut-shape point spread function (b) deconvolved SPCEM image (c) SW-SPRF image after applying the standing-wave algorithm on three deconvolved SPCEM images with phases (0, $2\pi/3$, and $4\pi/3$) (d) final SW-SPRF image with linear deconvolution to reduce sidelobes. Image size is 12um x 12um. The vertical profiles show the vertical point spread function of the selected region of interest.

result is shown in Figure 6-7(c) where the FWHM has been improved to 124 nm. This is close to the simulated result of about 117 nm. The side band of the point spread function of SW-SPRF in Figure 6-7(c) can be further removed with simple linear deconvolution as shown in Figure 6-7(d). This step does not affect the FWHM but

serves only to suppress the sidelobes. Vertical profiles of the point spread function shown in Figure 6-7(a) to (d) demonstrate that the FWHMs of SW-SPRF is more than a factor of two narrower than that of the deconvolved SPCEM in Figure 6-7(b) and approximately four times narrower that that of the original SPCEM point spread function in Figure 6-7(a). In general although one directional resolution enhancement has been demonstrated here, two-dimensional imaging with extended-resolution in both directions is also possible (Chung et al. 2007; Fiolka et al. 2008).

In conclusion, sub-diffraction-limited resolution is achieved with standing surface plasmon resonance waves. SW-SPRF also shows a significant increase in signal contrast. While SW-SPRF retains the advantages of SPCE microscopy including decreased fluorescence lifetime and thus reduced photobleaching for biological imaging, it does not suffer from a wide point spread function and results in four times improved resolution over SPCE microscopy. The use of silver instead of gold, together with optimized surface roughness and thickness of the silica layer may lead to greater signal enhancement (Borejdo, Calander, et al. 2006). Moreover, the use of metal gratings has a potential for further resolution enhancement (Raether 1988). In general, SW-SPRF may be useful in applications requiring both high signal-to-noise ratio and high spatial resolution such as in imaging, biomolecular sensing, and nano-scale lithography (Liu et al. 2005).

CHAPTER 7: CONFOCAL SURFACE PLASMON RESONANCE FLUORESCENCE MICROSCOPY

The previous chapters looked into the various aspects of employing surface plasmons for wide-field fluorescence microscopy. In those investigations, a *p*-polarized plane wave was launched using a high NA microscope objective to excite surface plasmons, similar to using a plane wave in the Kretschmann-Raether configuration. In a laser scanning type microscope where the image is assembled point by point by scanning the beam across the sample under study, one can also use surface plasmons to excite fluorophores on the sample. However the mode of excitation involves focusing the laser beam with the objective lens into a small focal spot to excite the plasmons unlike the use of a plane wave in wide-field SPCE microscopy which illuminates a much larger area. The use of surface plasmons in confocal fluorescence microscopy can be termed confocal SPRF. The use of surface plasmons in a confocal set-up is only quite recent. The set-up has been used to study single molecule fluorescence mediated by surface plasmons (Stefani et al. 2005) as well as to study the rotational dynamics of actin molecules (Borejdo, Gryczynski, et al. 2006). Furthermore, the same set-up was

utilized in a plasmon-mediated confocal dark-field type microscope (Schmelzeisen et al. 2008), as well as in the measurement of cell-substrate contacts (Moh et al. 2008). It was also extended with multiple photodetectors for refractive index measurements (Tanaka and Yamamoto 2003). The advantage of confocal SPRF lies in its small detection volume, about twofold smaller than in TIRF, in the range of attoliters compared to the femtoliters scale in typical confocal micrososcopy owing to the distance dependent coupling effect of surface plasmons (Borejdo, Gryczynski, et al. 2006). This makes it useful in single molecule studies where a small volume is required for sensitive and quantitative detection of molecular concentrations in the micromolar range. While this can be achieved by using zero-mode waveguides consisting of small apertures patterned on a metal film (Levene et al. 2003; Edel et al. 2005), the fabrication process is more cumbersome and expensive compared to confocal SPRF. In this chapter, improvements are made to the original confocal SPRF by considering radially polarized illumination for exciting fluorescent samples, imaging them in the far-field and measuring their point spread functions. The excitation and image formation of a surface plasmon confocal microscope is modeled to facilitate the study. Finally, modifications are proposed to improve the detection efficiency of the confocal microscope.

7.1 SPR Excitation by Focused Beam

In a typical confocal set-up, the laser source is beam-expanded to fill the back aperture of the objective lens which is then focused on to the sample. For the purpose of exciting surface plasmons, it is noted that a high NA objective lens needs to be

used so that the range of angular spectrum incident on the metal layer is broad enough to contain k-vectors which can match the momentum of the surface plasmons. This condition is similar to the phase-matching condition required for the plane-wave excitation of surface plasmons in wide-field SPCEM. As an example, for the case where a gold layer is used and the sample medium is air, a numerical aperture greater than 1.1 is required to excite surface plasmons. Expressed mathematically, the minimum numerical aperture required is

$$NA > \mathrm{Re}\sqrt{\frac{\varepsilon_1 \varepsilon_2}{\varepsilon_1 + \varepsilon_2}}, \tag{7.1}$$

where ε_1 and ε_2 denote the permittivity of the sample medium and metal layer respectively. Because of the high numerical aperture that is used, the treatment of the imaging model requires the use of high NA theory as opposed to the paraxial theory

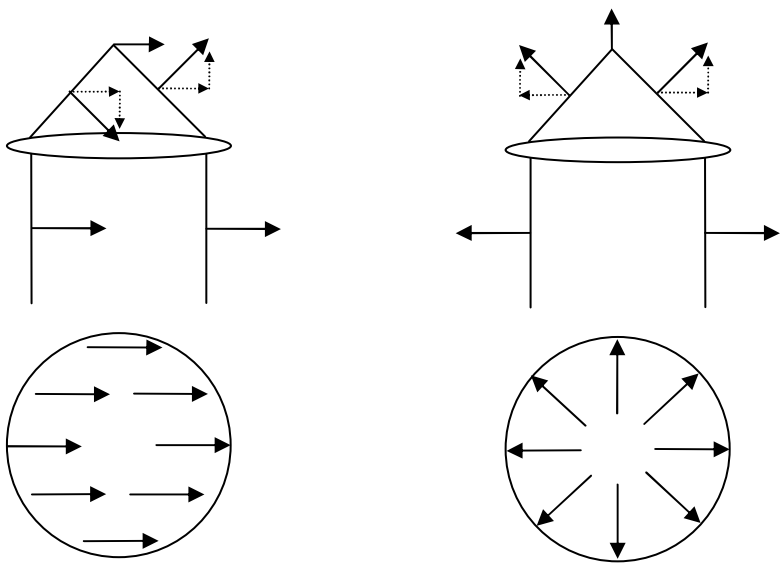

Figure 7-1. Effects of focusing linearly polarized light (left) and radially polarized light (right) through a high NA objective lens. The polarization pattern at the back aperture of the lens is also shown for each case on the bottom.

that is normally used (Gu 2000; Richards and Wolf 1959).

In many confocal fluorescence and confocal SPRF set-ups, a linearly polarized source is normally used to excite the sample (Bouhelier et al. 2007; Chon and Gu 2004; Pawley 2006). For linearly polarized light focused through a high numerical objective, the outer rays bend over a large angle resulting in significant transverse and axial components. Due to the linear polarization of the incoming beam, the polarization on the axis at the focus becomes laterally polarized since the axial components are out of phase and cancel out each other as can be seen in the left panel of Figure 7-1. However, away from the axis of propagation, there is considerable axial component which results in a split focus (Chon et al. 2002; Chon and Gu 2004). In addition, because surface plasmons are necessarily excited by *p*-polarized light, it can be seen that only the part of angular spectrum that is near the horizontal axis of the back aperture will induce surface plasmons while the spectrum near the vertical axis is *s*-polarized and does not contribute to the excitation. Hence, one can expect the excitation point spread function to be asymmetric. Instead of linear polarization, it is also possible to use a radially polarized beam to fill the back aperture of the objective. As shown in the right panel of Figure 7-1, the use of a high NA objective results in significant transverse and axial components as before. However in this case, the on-axis component at the focus is purely axial as the lateral components are out of phase and cancel each other. Furthermore, when compared to the linear case, the radially polarized light is axially symmetric as seen at the back aperture. And as the polarization vectors are radial, it can be seen that all light rays entering the objective will be *p*-polarized when focused, which will be able to excite surface plasmons.

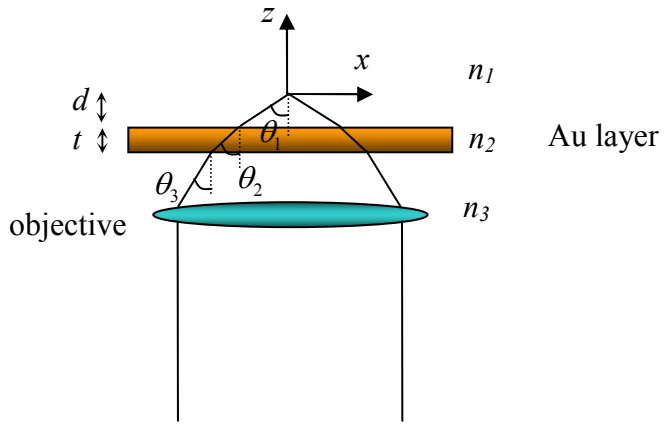

Figure 7-2. Axis convention, n_1 and n_3 are the sample and immersion refractive indices, while n_2 is the refractive index of the gold layer.

Therefore, one can expect that the excitation point spread function will be circularly symmetric in this case.

Referring to the axis convention in Figure 7-2, expressions of the electric field at the focus can be derived. For linearly polarized light (Török and Varga 1997), the field $\mathbf{E_i} = \left(E_{ix}, E_{iy}, E_{iz}\right)^T$ at the focus can be expressed in $\left(r_i, \varphi_i, z_i = 0\right)$ coordinates as

$$\begin{aligned} E_{ix} &= -i\left(I_0 + I_2 \cos 2\varphi_i\right) \\ E_{iy} &= -iI_2 \sin 2\varphi_i \\ E_{iz} &= -2I_1 \cos \varphi_i \end{aligned} \tag{7.2}$$

where I_0, I_1, I_2 are defined as

$$\begin{aligned} I_0 &= \int_0^\sigma \sqrt{\cos\theta_3} \sin\theta_3 \left(t_s + t_p \cos\theta_1\right) J_0\left(k_3 r_i \sin\theta_3\right) \exp\left(i\Phi\right) \mathrm{d}\theta_3 \\ I_1 &= \int_0^\sigma \sqrt{\cos\theta_3} \sin\theta_1 \sin\theta_3 t_p J_1\left(k_3 r_i \sin\theta_3\right) \exp\left(i\Phi\right) \mathrm{d}\theta_3 \\ I_2 &= \int_0^\sigma \sqrt{\cos\theta_3} \sin\theta_3 \left(t_s - t_p \cos\theta_1\right) J_2\left(k_3 r_i \sin\theta_3\right) \exp\left(i\Phi\right) \mathrm{d}\theta_3 \end{aligned} \tag{7.3}$$

J_0, J_1, J_2 denote the zero, first and second order Bessel functions of the first kind. The intensity is thus

$$I_{ex} = |I_0|^2 + 4|I_1|^2 \cos^2 \varphi_i + |I_2|^2 + 2\,\mathrm{Re}\left[I_0 I_2^*\right] \cos 2\varphi_i. \tag{7.4}$$

Similarly, when radially polarized light is used, the field at the focus is given by

$$\begin{aligned} E_{ix} &= 2I_1 \cos\varphi_i \\ E_{iy} &= 2I_1 \sin\varphi_i \\ E_{iz} &= 2iI_0 \end{aligned} \tag{7.5}$$

where I_0, I_1 are defined by

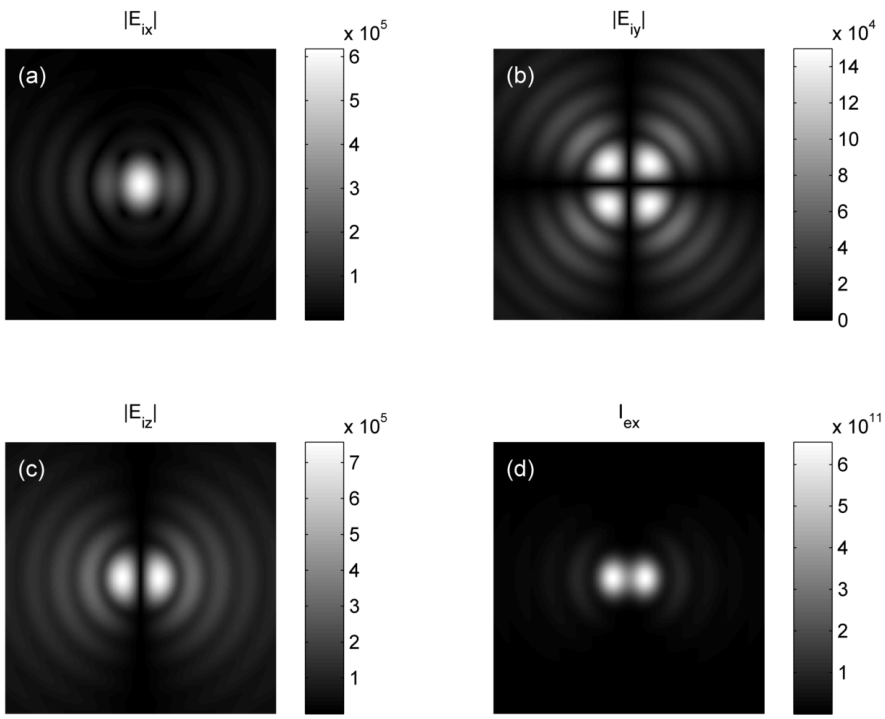

Figure 7-3. Focused beam excitation with linearly polarized beam (horizontal polarization). Magnitude of field components (a) $|E_{ix}|$ (b) $|E_{iy}|$ (c) $|E_{iz}|$ and intensity pattern (d).

$$
\begin{aligned}
I_0 &= \int_0^{\sigma} \sqrt{\cos\theta_3}\,\sin\theta_1 \sin\theta_3 t_p J_0\left(k_3 r_i \sin\theta_3\right)\exp\left(i\Phi\right)\mathrm{d}\theta_3 \\
I_1 &= \int_0^{\sigma} \sqrt{\cos\theta_3}\,\cos\theta_1 \sin\theta_3 t_p J_1\left(k_3 r_i \sin\theta_3\right)\exp\left(i\Phi\right)\mathrm{d}\theta_3
\end{aligned}
\tag{7.6}
$$

and t_s, t_p denote the Fresnel coefficients of the light travelling from medium 3 to medium 1. The upper integration limit σ denotes the angular semi-aperture of the objective lens which satisfies the sine condition, and the wavefront aberration Φ is given by $k_1 \cos\theta_1 d - k_3 \cos\theta_3 \left(d + t\right)$. In the radially polarized case, the intensity is thus

$$
I_{ex} = 4\left|I_0\right|^2 + 4\left|I_1\right|^2 . \tag{7.7}
$$

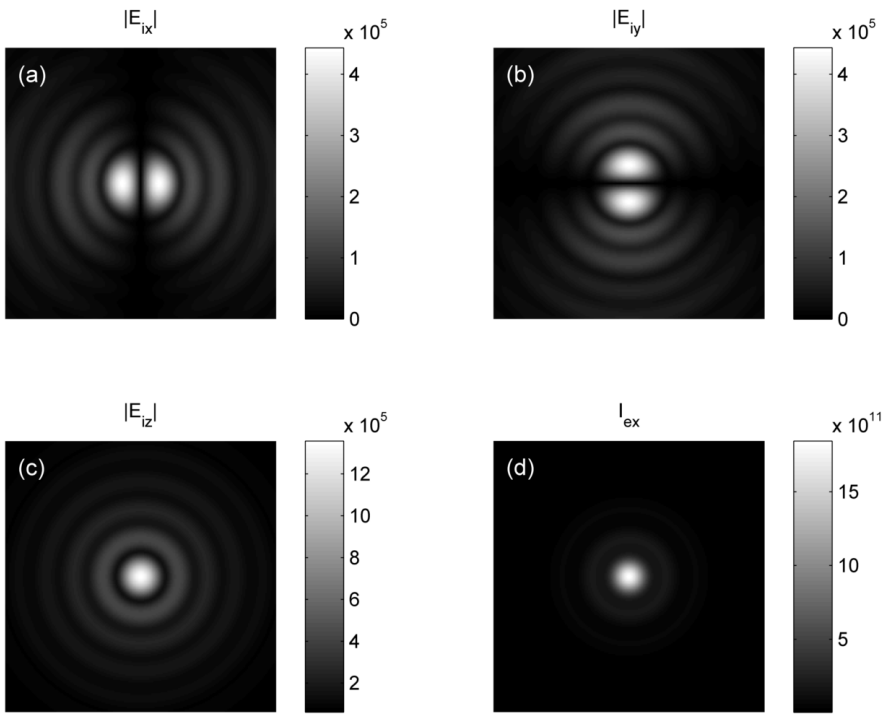

Figure 7-4. Focused beam excitation with radially polarized beam. Magnitude of field components (a) $|E_{ix}|$ (b) $|E_{iy}|$ (c) $|E_{iz}|$ and intensity pattern (d).

Figure 7-3 displays the magnitude of the electric field and the calculated intensity for a linearly polarized beam focused by a high 1.45 NA objective lens. The gold metal layer is assumed to be 40 nm in thickness. At the focus, it is observed that there exists a split in the focal spot which is due to the high numerical aperture used. Furthermore, the excitation point spread function is asymmetric mainly in the horizontal direction in line with the orientation of the incoming polarization which becomes *p*-polarized after focusing. The intensity is zero along the vertical axis because light in the region becomes *s*-polarized after focusing. Figure 7-4 shows the magnitude of the electric field and the calculated intensity for a radially polarized beam focused by the same objective lens. Due to the axial symmetry of the polarization of the incoming beam, it can be seen that the E_{ix} and E_{iy} components are orthogonally symmetric. Furthermore, the axial component of the field is the strongest among all components due to the high numerical aperture. The excitation point spread function is also circularly symmetric as expected. Comparing the excitation point spread function of the radially polarized case to the linearly polarized case, it is also observed that the energy of the former is concentrated into the single lobe, resulting in a higher peak intensity at the origin which can be used to excite the sample more efficiently. The proposed radially polarized beam is considered to be more advantageous compared to the linearly polarized beam for focused excitation of a sample in confocal SPRF owing to a more compact and symmetric excitation point spread function which has a higher resolution as well as a higher peak intensity. It is also of interest to point out that the metal layer on the substrate results in an annulus-like excitation profile due to the transmission coefficient having a narrow passband-

like profile as can be seen in Figure 7-5. This is similar to, although not entirely the same as passing a radially polarized beam through an annular ring(Sheppard and Choudhury 2004).

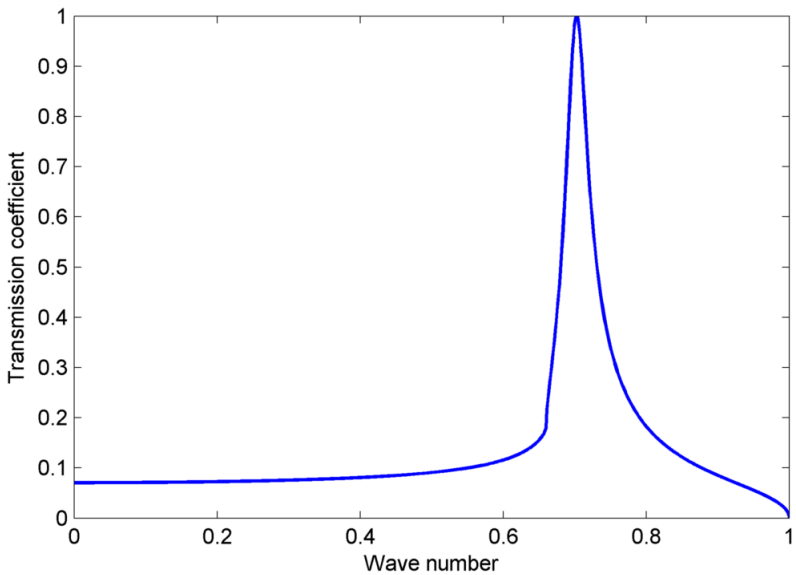

Figure 7-5. Plot of the normalized transmission coefficient as a function of wave-number shows a sharp and narrow peak where most of the energy is passed through the metal layer.

7.2 Theory for Confocal SPRF

To extend the model of wide-field SPCEM to confocal SPRF, it is necessary to take into account the focused excitation, the scanning action, as well as the effect of the pinhole. Based on the expression in chapter two, the wide-field point spread function was derived as

$$I_{PSF} = \int_0^{\pi}\int_0^{2\pi} |\mathbf{E}_\mathrm{i}|^2 I_{em} \sin\theta_d \mathrm{d}\phi_d \mathrm{d}\theta_d, \tag{7.8}$$

averaged over all dipole orientations, where $|\mathbf{E_i}|^2$ is the intensity of the excitation plane wave and I_{em} is the emission point spread function. For the case of confocal SPRF, the intensity at the focal plane can be expressed as

$$I_F = \int_0^{\pi} \int_0^{2\pi} I_{ex} I_{em} \sin\theta_d \mathrm{d}\phi_d \mathrm{d}\theta_d, \tag{7.9}$$

where I_{ex} is the excitation point spread function of the focused beam. I_{ex} is a function of the source coordinates $(r_i, \varphi_i, z_i)^T$ while I_{em} is a function of the detector coordinates $(r_d, \varphi_d, z_d)^T$. To take into account the scanning action, we can consider the lateral displacement of the focused excitation beam from the optical axis as shown in Figure 7-6. If the focus beam is displaced laterally by $\mathbf{r}_i'$, then at the detector plane the image is also displaced by a distance of $-M \times \mathbf{r}_i'$ where M is the total magnification of the microscope. Furthermore, to account for the effects of a finite sized pinhole, it is necessary to integrate I_F over the area of the pinhole detector

$$I_{PSF} = \int_0^{R} \int_0^{2\pi} I_F \; r_p \mathrm{d}r_p \mathrm{d}\phi_p \tag{7.10}$$

where R is the pinhole radius and (r_p, ϕ_p) define the coordinates of the pinhole. The relation between the pinhole coordinates and the detector plane coordinates is $\mathbf{r_p} = \mathbf{r_d} - M \times \mathbf{r}_i'$. The illustration in Figure 7-6 shows the position of the excitation field and the image position in the detector plane relative to the position of the pinhole. Therefore, the point spread function of the confocal SPRF microscope can be calculated based on Equation (7.10) and is shown later in Figure 7-8.

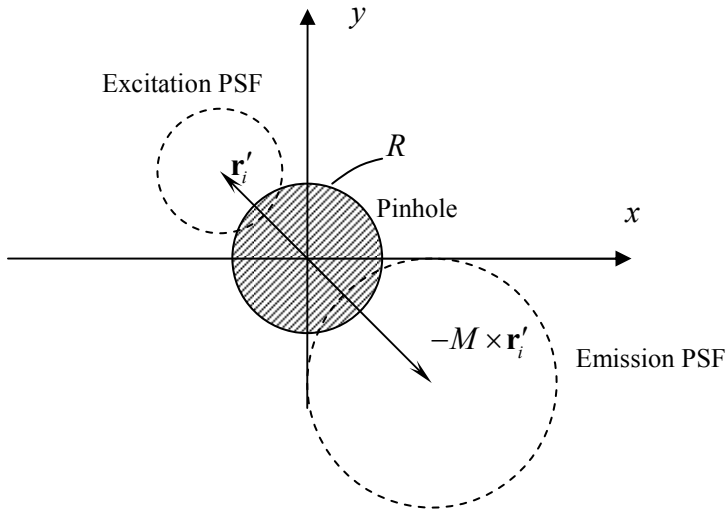

Figure 7-6. Illustration of the calculation to take into account the scanning action in confocal SPRF.

7.3 Experimental Results

7.3.1 Generation of radially polarized beam

There has been much research into the generation of radially polarized beams and a number of methods have been proposed. Generally, the methods can be classified into interferometric and polarization rotation methods. In the interferometric method, the incoming beam is split into two arms and modifications are done to the phase or polarization of each arm, after which both arms are then recombined to approximate radial polarization (Biss et al. 2006). Another method involves interfering two circularly polarized beams, after each passes through a spiral phase delay with differing handedness (Tidwell et al. 1990). Generally, interferometric methods suffer from stability problems and require good control of correction of alignment errors. In this sense, polarization rotation methods are more reliable. One method involves

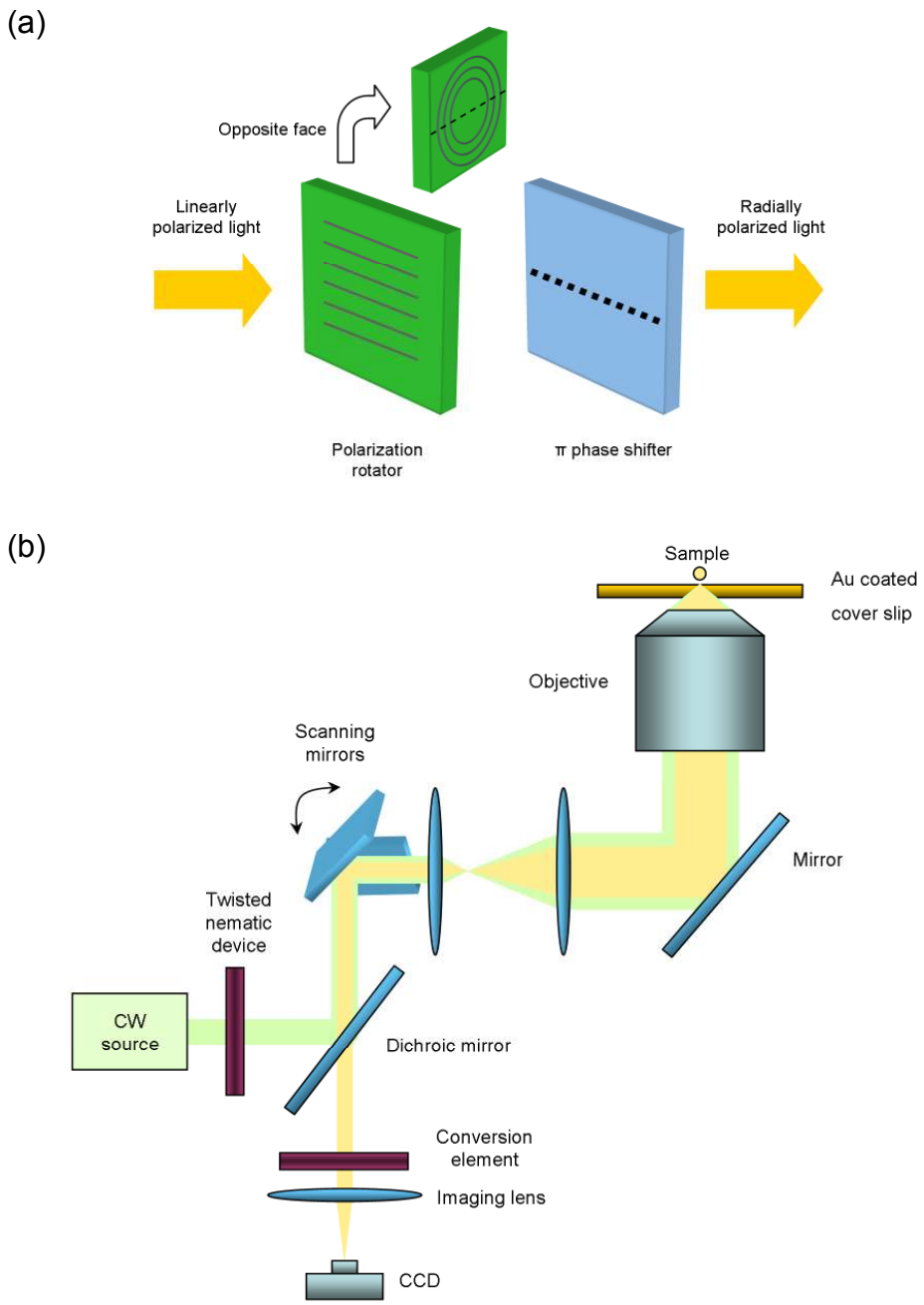

Figure 7-7. (a) Linear to radial polarization converter consisting of a circularly rubbed plate and a π phase shifter (b) schematic diagram of the confocal SPRF set-up.

approximating radial polarization by using four or eight-segmented half wave-plates with the appropriate fast axis orientation in each segment so that polarization vectors

are rotated to the desired radial orientation (Yoshiki et al. 2007; Dorn et al. 2003). Another approach uses a parallel-aligned liquid crystal spatial light modulator device sandwiched between two quarter wave-plates to act as a polarization rotator (Davis et al. 2005; Ye 1995). This method requires the use of another spatial light modulator to correct for the added output phase retardation. Yet another method utilizes a twisted nematic liquid crystal device in which the substrate is linearly rubbed in the input face and circularly rubbed in the output face to produce radial polarization (Yamaguchi et al. 1989; Stalder and Schadt 1996). This method requires the use of a π phase plate to compensate for one half of the plate where the polarization is out of phase due to the limited twist angle of the liquid crystal director molecules.

7.3.2 Confocal SPRF imaging

In our experiments, we chose to use the twisted nematic device to generate radially polarized beams for confocal SPRF. Figure 7-7 shows a schematic of the twisted nematic device and the confocal set-up that is used in the experiments. The device consists of a liquid crystal substrate with one face horizontally rubbed and the opposite face circularly rubbed, as well as a π phase shifter separated by a few millimeters. The device acts as a waveguide by rotating horizontally polarized light to their radial positions as they propagate through it and has a transmission efficiency of 70%. In the confocal set-up, a continuous wave solid state laser source of 532 nm was directed through the twisted nematic device. The outcoming radially polarized light was then fed into the Olympus FV300 scanning unit. The optical path in the FV300 scanning unit is straightforward and consists of a dichroic mirror which reflects the

excitation wavelength of 532 nm and passes the emission wavelength of 560 nm. The reflected excitation beam then falls on to a piezo-actuated dual-axis scan mirror unit. The scan mirrors are aluminum coated and work for a broad range of visible wavelengths. The scan mirrors are also non-polarizing which does not adversely affect the polarization of the radially polarized beam. This was confirmed by removing the objective and observing the donut profile in the far-field as well as by checking with an analyzer placed it at various different orientations and looking at the symmetry of the intensity patterns. The beam is subsequently expanded via the pupil lenses to fill the back aperture of a high NA objective (PlanApo NA1.45 60X, Olympus) and focused on to the sample which is placed on a gold and silicon dioxide coated coverslip (Au 40 nm, SiO_2 5 nm). Fluorescence emission from the sample is collected with the same high NA objective, descanned by the scan mirrors and passed through the dichroic mirror.

Finally, the emission light is focused by an imaging lens and collected by a photomultiplier tube within the scanning unit. Control of the scanning speed, image field of view and image acquisition rate is done via the FluoView 5.0b software provided with the microscope (Olympus, Japan). The typical scan time for each scan is approximately 1 second, and for each averaged scan it takes about 5 to 10 seconds. For the sample, fluorescent beads with a nominal diameter of 40 nm (Molecular Probes, F8792) were dispersed on the gold coater cover slip, dried overnight and sealed onto a glass slide. Figure 7-8(a) and (b) show the far-field image of the beads using a pinhole diameter of 300μm for imaging the excitation point spread function and compares the results of using a linearly polarized and radially polarized light. As

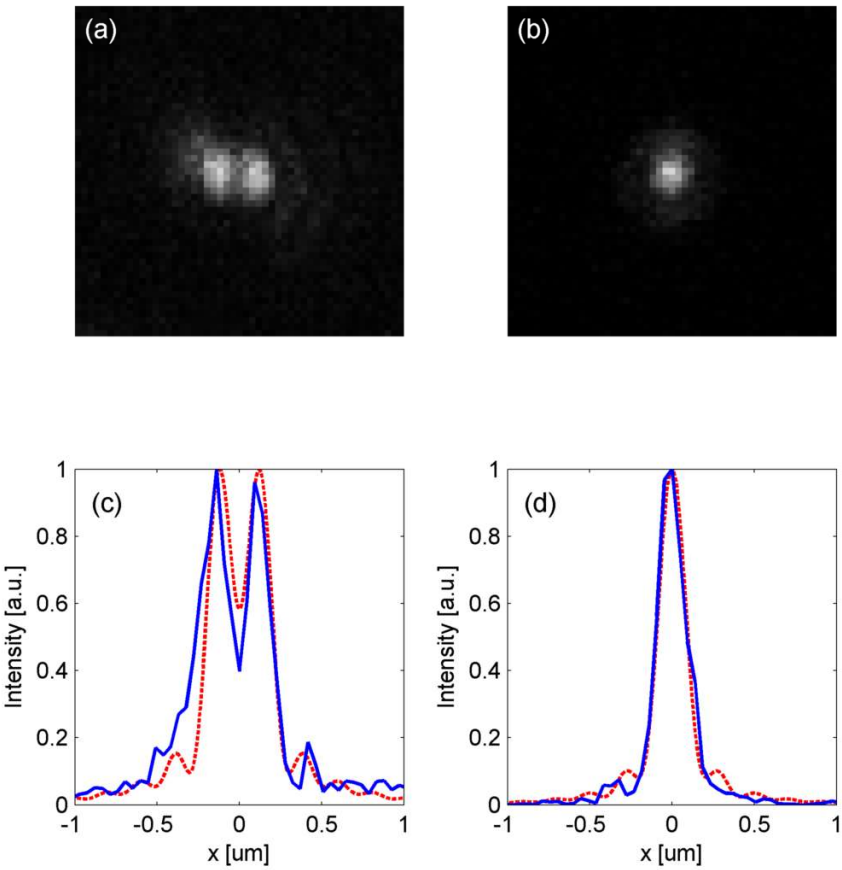

Figure 7-8. Comparison of point spread functions. (a), (c) Linear polarized illumination and (b), (d) radially polarized illumination. Solid line denotes experimental result and dotted line denotes simulated result.

polarized illumination. When linear polarization is used in the confocal SPRF microscope, the point spread function displays two lobes. On the other hand when radially polarized light is used, point spread function becomes circularly symmetric with only a single lobe. Figure 7-8(c) and (d) compare the experimental results with the theoretical point spread functions derived in Equation (7.10). As can be seen, the experimental point spread functions closely resemble the theoretical point spread functions for both cases, when either linear or radial polarization is used. The radially polarized illumination has the advantage of having a symmetric and single-lobed

point spread function as compared to a linearly polarized illumination. It is noted that radially polarized illumination was also used recently in two-photon fluorescence microscopy to image biological samples (Moh et al. 2009), but our study deals with the theoretical model and experimental differences in the excitation point spread function of linearly and radially polarized illumination in confocal SPRF.

7.4 Detection with Conversion Element

Apart from optimizing the excitation point spread function of the focused beam in a confocal SPRF microscope in the previous section, the detection efficiency of the microscope can also be increased by adding a conversion element in the detection path of the microscope as was discussed in chapter five for the wide-field case. The reason for this is that when the SPCE fluorescence is imaged by a tube lens with a small numerical aperture, it results in a donut-shaped spot which has a null in the center. Therefore, the light is not efficiently detected due to the presence of a confocal pinhole in front of the donut-shaped spot. In general, while it is desirable to keep the pinhole size small in confocal microscopy, the null in the center results in poor signal strength and may require enlarging to improve the signal, thereby causing a reduction in both the lateral and axial resolutions. In view of such conflicting requirements, a choice of either the spiral phase plate (SPP) or the polarization mode converter (PMC) can be used as a conversion element inserted in the detection path of the microscope. Such an improvement can be important for many applications especially for weakly fluorescent samples or for single molecule tracking applications. To calculate the improvement in detection efficiency with and without the conversion element, a

radiating axial dipole is used as a single point source. For the case without any conversion element, an expression for the power collected by the finite size detector with a radius of v_p can be derived as

$$P_1 = \int_0^{v_p} \left(4|K_0|^2 + 4|K_1|^2 \right) v \, \mathrm{d}v \tag{7.11}$$

where K_0, K_1 are defined as

$$\begin{aligned} K_0 &= \int_0^{\alpha} a(\theta)\tau_p \sin^3\theta J_0\left(\frac{v\sin\theta}{\sin\alpha}\right)\mathrm{e}^{i\Phi}\mathrm{d}\theta \\ K_1 &= \int_0^{\alpha} a(\theta)\tau_p \sin^2\theta\cos\theta J_1\left(\frac{v\sin\theta}{\sin\alpha}\right)\mathrm{e}^{i\Phi}\mathrm{d}\theta. \end{aligned} \tag{7.12}$$

For the case where the SPP element is used, then the power collected is

$$P_2 = \int_0^{v_p} \left(2|M_0|^2 + 4|M_1|^2 + 2|M_2|^2 \right) v \, \mathrm{d}v \tag{7.13}$$

where M_0, M_1, M_2 are

$$\begin{aligned} M_0 &= \int_0^{\alpha} a(\theta)\tau_p \sin^2\theta\cos\theta J_0\left(\frac{v\sin\theta}{\sin\alpha}\right)\mathrm{e}^{i\Phi}\mathrm{d}\theta \\ M_1 &= \int_0^{\alpha} a(\theta)\tau_p \sin^3\theta J_1\left(\frac{v\sin\theta}{\sin\alpha}\right)\mathrm{e}^{i\Phi}\mathrm{d}\theta \\ M_2 &= \int_0^{\alpha} a(\theta)\tau_p \sin^2\theta\cos\theta J_2\left(\frac{v\sin\theta}{\sin\alpha}\right)\mathrm{e}^{i\Phi}\mathrm{d}\theta. \end{aligned} \tag{7.14}$$

For the case where the PMC element is used, then the power collected is

$$P_3 = \int_0^{v_p} \left(|G_0|^2 + 2|G_1|^2 + |G_2|^2 \right) v \, \mathrm{d}v \tag{7.15}$$

and G_0, G_1, G_2 are

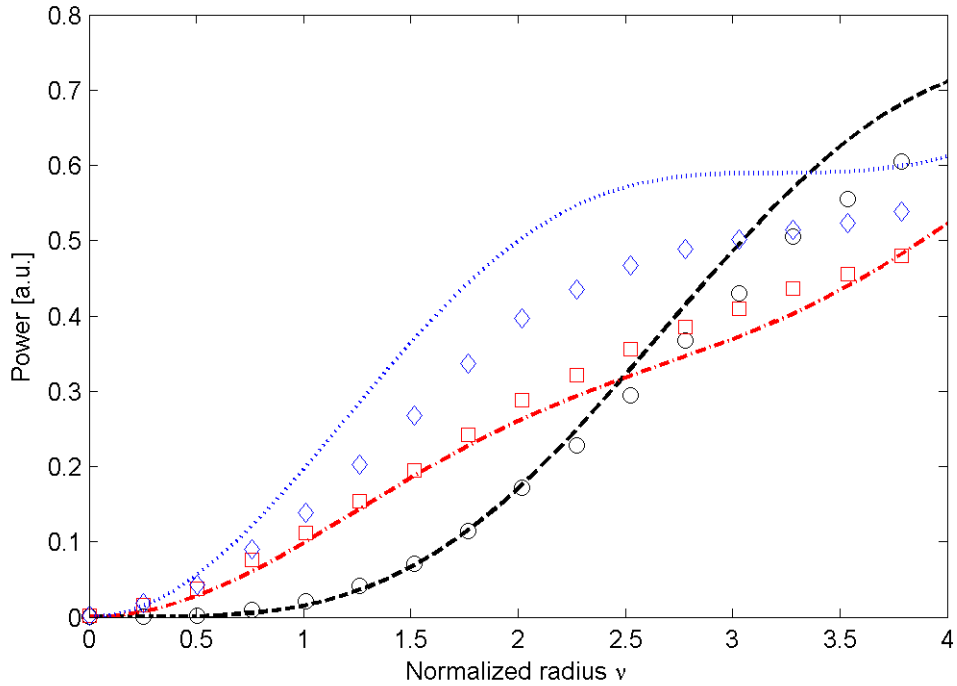

Figure 7-9. Comparison of power collected by a pinhole with normalized radius v. Theoretical calculation: (Dashed line) without conversion element, (dash-dotted line) with SPP, (dotted line) with PMC. Experimental results: (circles) without conversion element, (squares) with SPP, (diamonds) with PMC.

$$
\begin{aligned}
G_0 &= \int_0^{\alpha} a(\theta)\tau_p \sin^2\theta\left(1+\cos\theta\right)J_0\left(\frac{v\sin\theta}{\sin\alpha}\right)\mathrm{e}^{i\Phi}\mathrm{d}\theta \\
G_1 &= \int_0^{\alpha} a(\theta)\tau_p \sin^3\theta J_1\left(\frac{v\sin\theta}{\sin\alpha}\right)\mathrm{e}^{i\Phi}\mathrm{d}\theta \qquad (7.16) \\
G_2 &= \int_0^{\alpha} a(\theta)\tau_p \sin^2\theta\left(1-\cos\theta\right)J_2\left(\frac{v\sin\theta}{\sin\alpha}\right)\mathrm{e}^{i\Phi}\mathrm{d}\theta.
\end{aligned}
$$

J_0, J_1, J_2 denote the zero, first and second order Bessel functions of the first kind, while α is the semi-angular aperture of the imaging lens and is given by the objective NA divided by its magnification. v is the normalized pinhole radius $v = kr\sin\alpha$ and $a(\theta)$ is the aplanatic factor expressed as a function of θ, the objective magnification β, and the refractive index of the immersion oil n_{oil},

$$a(\theta) = \left(\frac{\cos^2 \theta}{1 - \beta^2 \sin^2 \theta / n_{oil}^2} \right)^{1/4} . \tag{7.17}$$

As a comparison, Figure 7-9 shows a graph with the collected powers P_1, P_2 (with SPP) and P_3 (with PMC) for increasing pinhole sizes. P_1, P_2 and P_3 are normalized by the total power when pinhole size is infinite which corresponds to the widefield case. The theoretical curves are plotted using dashed, dash-dotted and dotted lines respectively. Experimental results obtained using the system in Figure 5-9 with a NA0.9 40X objective are also shown in the same figure. In the experiments, the wide-field point spread functions are obtained and a virtual pinhole is considered by integrating the image intensities falling within the pinhole of a specified radius. The experimental results are shown in the figure denoted with circles, squares and diamonds, respectively. In general, the experimental results are reasonably close to the theoretical curves. The slight differences between theoretical and experimental results are attributed to the background signal of the captured images, as well arising from the discretization effects of the virtual pinhole. In essence, a confocal pinhole with a normalized radius less than 2 is desired due to a better lateral and axial resolution (i.e. less than 0.52 Airy units). Another reason to avoid pinhole with sizes greater than 2 is that imaging artifacts can start to appear owing to the finite detector size (Gu 1996). From Figure 7-9, it is observed that for pinhole radii less than ~2.5, both the SPP and PMC give improved detection efficiencies compared to not using any conversion elements. However, the PMC gives consistently better performance compared to the SPP.

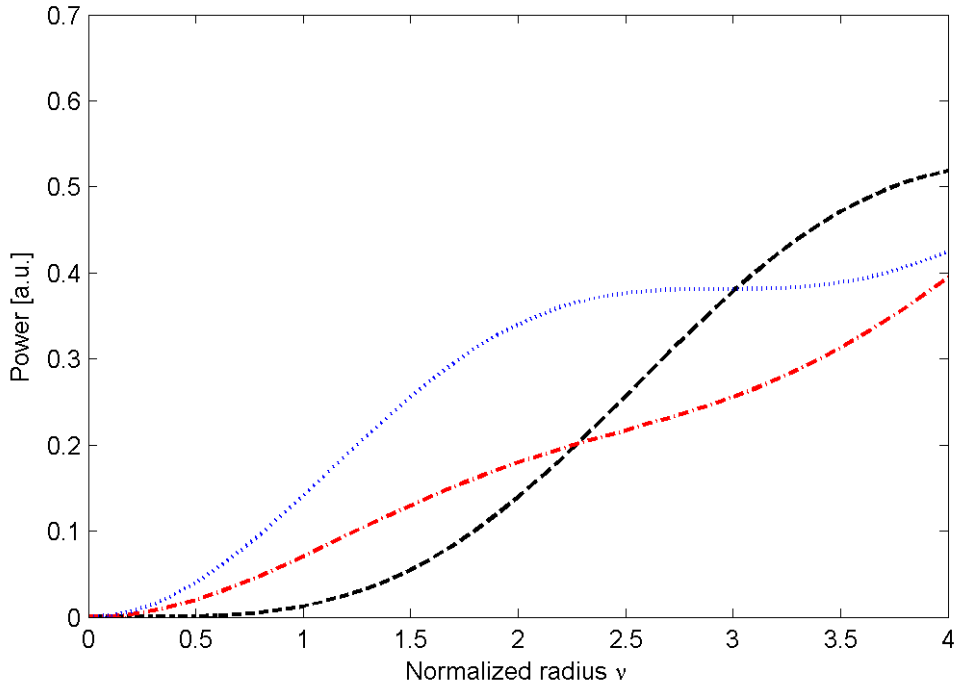

Figure 7-10. Comparison of power collected in confocal SPRF by a pinhole with normalized radius v. (Dashed line) without conversion element, (dash-dotted line) with SPP, (dotted line) with PMC.

To demonstrate the results on actual imaging conditions, the following experiment was carried out by inserting the SPP in the detection path of the FV300 scanning unit of the confocal microscope. The NA1.45 60X objective was used in the confocal microscope. For the confocal SPRF microscope, the power collected P_1, P_2 (with SPP) and P_3 (with PMC) are plotted in Figure 7-10. It can be seen from the curves that more energy is distributed in the sidelobes owing the directional emission of surface plasmons. Due to size constraints of the scanning unit, only the SPP and not the PMC element was tested in the experiment. HeLa cells were grown on Au-SiO_2 coated (40 nm, 5 nm) cover slips overnight. They were then fixed with 4% methanol free formaldehyde and labeled with AlexaFluor 532 (Molecular Probes). The sample was then imaged with the modified confocal microscope both with and

without the SPP element. A normalized pinhole radius of 2 was used for the imaging. This pinhole size was the smallest available with the FV300 unit. The input power entering the back aperture of the objective was maintained at 350μW. Figure 7-11(a) and (b) show the imaging results while Figure 7-11(c) and (d) plot a line section

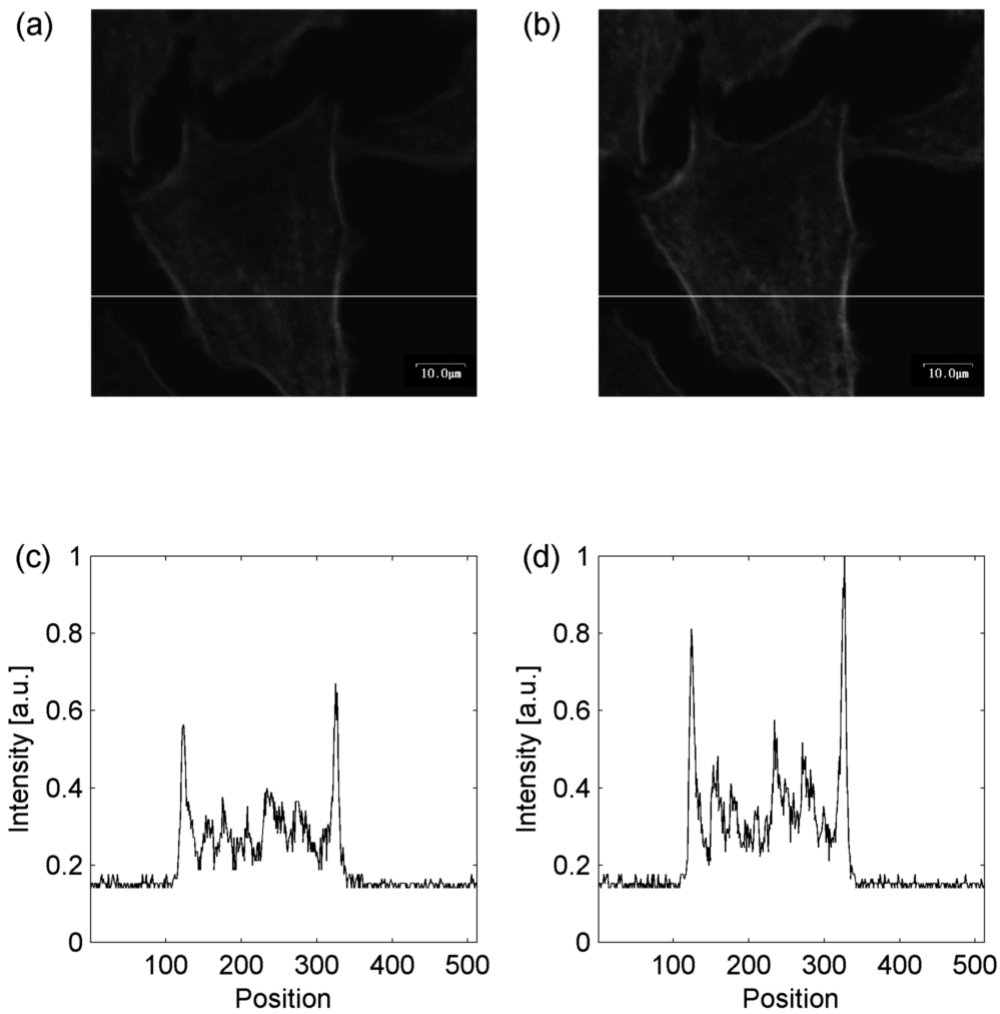

Figure 7-11. Comparison of images (a) without SPP and (b) with SPP. A line profile through the image (denoted by a white line) is plotted in (c) and (d) respectively for both cases.

through the images. It can be seen from figures especially the line plots that there is an increase in the image intensity when the SPP is inserted. Overall the image intensity is improved by a factor of 13% compared to the theoretical factor of 17%. This difference can be attributed to losses incurred by the SPP element introduced into the detection path. According to Figure 7-10, use of the PMC element will give a higher improvement factor.

In this chapter, radially polarized illumination has been proposed for confocal SPRF and is shown to be better in comparison to linearly polarized illumination. This was confirmed both with our theoretical model and with experimental results. Furthermore, modification of confocal SPRF with the addition of a conversion element can give better detection efficiency and is able to improve the overall detected signal.

CHAPTER 8: PERSPECTIVES AND CONCLUSION

Currently, surface plasmonics is an area of active research, with applications found in many diverse fields such as nanolithography, negative index materials, imaging and biological sensing. Although much work has been done in the above areas, there is still much room in the study of using surface plasmons in microscopy. In this thesis, we explored the use of surface plasmons in fluorescence microscopy, both in wide-field as well as scanning systems. Apart from the advantages of surface plasmons in fluorescence imaging, such as an increased excitation efficiency, reduced photobleaching and fluorescence lifetime, as well as improved background rejection, this thesis discussed and demonstrated ways to improve the image formation aspects of utilizing surface plasmons in microscopy. This included using special phase or polarization elements to improve the point spread function and detection efficiency of the microscope as well as using the standing surface plasmon wave technique to achieve sub-diffraction limited resolution. The advantage of low photobleaching, high single molecule sensitivity and high resolution capability of this microscopy technique can play a significant role in the imaging and understanding of cellular

processes. In the following, an example where our technique may be useful is discussed.

T-cells play an important role in a body's adaptive immune system by mediating responses to foreign invading pathogens. The T-cell response is typically induced through T-cell receptors (TCR) by recognizing antigens presented on peptide-major histocompatibility complexes (pMHC) of antigen presenting cells (APC). Studies of the interaction between T-cells and APCs at the TCR-pMHC interface gave rise to the discovery of a complex structure at the interface known as the immunological synapse (Grakoui et al. 1999; Monks et al. 1998). The mature immunological synapse is characterized by an accumulation of TCR-pMHC clusters in the central region known as the central supramolecular activation cluster (c-SMAC) surrounded by a ring consisting of leukocyte function associated molecule-1 (LFA-1) – intercellular cell adhesion molecule-1 (ICAM-1) interactions known as the peripheral supramolecular activation cluster (p-SMAC). Larger molecules such as CD45 are located further away in the distal supramolecular activation cluster (d-SMAC). The c-SMAC is also enriched in protein kinase C θ (PKCθ), a TCR downstream effector signaling molecule. Other proteins which are important for T-cell activation include costimulatory molecules such as CD28-CD80/CD86 complexes, as well as signaling and adaptor proteins leukocyte C-terminal Src kinase (Lck), linker for activation of T-cell (LAT), zeta-associated protein of 70kDa (ZAP-70) and Src homology 2 (SH2) domain containing leukocyte phosphoprotein of 76 kDa (SLP-76) (Dustin 2008; Huppa 2003; Saito 2006).

The formation of a characteristic “bull’s-eye” structure within the immunological synapse was initially thought to be functionally important in concentrating TCR clusters within the c-SMAC in order to facilitate the sustained recognition of low-affinity ligands. It was also suggested that the c-SMAC was associated with the initiation of signaling in T-cells (Grakoui et al. 1999; Monks et al. 1998). However, further studies seemed to indicate otherwise. Experiments using phosphotyrosine antibodies showed that signaling in the c-SMAC was lower compared to the p-SMAC in wildtype CD4 T-cells (Lee et al. 2002, 2003). In addition, the heterogeneous structure of the immunological synapse in T, B and natural killer cells together with the fact that c-SMAC formation was not necessary for T-cell activation upon TCR engagement in cytotoxic T-cells questioned the role of the c-SMAC in TCR signaling (O'Keefe 2005; Purbhoo et al. 2004).

In recent works, the c-SMAC is suggested to be involved with TCR internalization and degradation while initial and sustained signaling in T-cells is shown to be due to the formation of TCR microclusters in the periphery of the contact site (Varma et al. 2006; Yokosuka et al. 2005). These TCR microclusters, which are suggested to be the minimal unit for initial and sustained TCR signaling, are formed at the periphery upon initial contact between T-cells and APCs, and translocate towards the center of the contact interface to form the c-SMAC. After the engagement of TCR with pMHC and the associated interaction with CD4/8 surface receptors, the Src family kinase Lck is recruited to the TCR/CD3 complex to phosphorylate tyrosine residues within the immunoreceptor tyrosines-based activation motifs (ITAMs), which then leads to recruitment of ZAP-70 to bind to the SH2 domains. Activated

ZAP-70 causes phosphorylation of transmembrane adaptor protein LAT which acts as a scaffold for adaptor proteins Grb2 and Gads and indirectly binds to SLP-76. It was also shown that while the signaling molecules LAT, ZAP-70 and SLP-76 were present in the initial microclusters, they did not move to the c-SMAC and were dissociated from the microclusters during translocation to the c-SMAC, thereby supporting the idea that microclusters function as a signalosome for T cell activation (Yokosuka et al. 2005).

However, as the visible TCR microclusters are composed of 30 to 300 TCRs, whose sizes can range from 500 nm to 700 nm (Campi 2005; Yokosuka 2010), it is conceivable that the initial TCR signaling can start even before the visible microclusters are formed. Furthermore, studies have showed the high sensitivity of antigen recognition by T-cells, and that even a single peptide-MHC ligand was able to trigger a transient calcium response (Irvine et al. 2002; Krogsgaard et al. 2005). Therefore, it can be hypothesized that initial signaling may occur at an earlier time before microcluster formation, and that sub-micron sized clusters may have aggregated to form the microclusters.

In order to study early cluster formation, a cell-bilayer model can be used. Previous studies on the immunological synapse have made use of either a cell-cell (e.g. Jurkat T-cell and Raji B-cell), or a cell-bilayer (e.g. McConnell's planar bilayer (McConnell et al. 1986)) model. The advantage of the supported planar bilayer is that it allows control of the bilayer composition as well as the availability to use a wide range of optical imaging methods such as TIRFM and interference reflection microscopy (IRM). Furthermore, there has been much research into the use of planar

bilayers in immunology for studying interactions at interfaces. For example, the cell-bilayer model has been shown to be able to activate CD4 and CD8 positive T-cells (Brian et al. 1984; Watts et al. 1984), and molecular segregation at the synapse has been shown to occur using both cell-cell and cell-bilayer models (Dustin et al. 1998; Monks et al. 1998). Data showing that the dynamics of the immune synapse in a cell-bilayer system follow a similar pattern to that of the cell-cell system, supports its use in many immunological studies. Apart from MHC molecules which are essential for antigen presentation, other important proteins which function as adhesion or costimulatory molecules such as ICAM-1, CD58, and CD80 are also reconstituted in the bilayer (Selvaraj et al. 1987; Takai et al. 1987), and are glycophosphatidylinositol (GPI)-linked to enable their ability for free lateral movement.

In the cell-cell model, either wide-field epi-illumination fluorescence microscopy or confocal laser scanning microscopy can be used (Irvine et al. 2002; Monks et al. 1998). However, even though the confocal microscope has better resolution due to its optical sectioning capability as compared to the conventional wide-field microscope, the main disadvantage is its slow scanning speed and long image acquisition time, which makes it undesirable for real-time imaging of cluster formation. On the other hand, for the cell-bilayer model, which is also commonly used in the study of the immunological synapse, the TIRF microscope is used because of its ability to image surfaces or interfaces with significant background rejection (Grakoui et al. 1999; Yokosuka et al. 2005). Another advantage is its fast acquisition rate, which makes it ideal for monitoring events in real-time. However, one disadvantage of using the TIRFM system in many of the studies (Irvine et al. 2002;

Yokosuka et al. 2005) is that, due to the diffraction-limited nature of light, structures much smaller than the TCR microclusters cannot be resolved adequately.

Therefore, in order to prove or disprove the above hypothesis, the SW-SPRF technique developed in this thesis, which can resolve structures about the size of a quarter of the wavelength of light, can be used to monitor early cluster formation within the T-cells at the T-cell–bilayer immunological synapse. Apart from the resolution advantage of this method over TIRFM, two other benefits include higher contrast and sensitivity owing to better background suppression, as well as reduced photobleaching due to the decreased fluorescence lifetime. As an experiment, antigen specific T-cells from transgenic mouse expressing EYFP-tagged CD3ζ can be placed on the supported planar bilayer system (Grakoui et al. 1999; McConnell et al. 1986) loaded with ICAM-1 and specific peptide-MHC II complex which are anchored to the bilayer via glycophosphatidylinositol (GPI). This would then allow SW-SPRF to monitor the dynamic formation of small clusters after antigen stimulation of the T-cells. Interactions of the T-cells with unloaded MHC II proteins are to be imaged as well, as a negative control test. In addition, colocalization studies of CD3ζ and anti-pZAP-70 can also be carried out to identify signaling sites. In these tests, a reduction in photobleaching in SW-SPRF will also be advantageous for live cell imaging in real-time for an extended period of time. Overall, it is envisaged that the SW-SPRF technique will be helpful in elucidate the initial signaling events which lead up to TCR activation.

In summary, the conventional SPCE microscope was shown to produce a point spread function that has a donut shaped structure. This was proved by developing a

model of the microscope as well as by substantiating the model with experimental results. The distorted point spread function can also be explained in terms of the derived vectorial optical transfer function, where the dark center valley of the point spread function can be attributed to zero crossings and the negative values in the transfer function. In order to compensate for the distortion, one can use either non-physical or physical methods. For the former, one way to achieve this is to use numerical deconvolution techniques, where an iterative method was shown to give good results. For the latter, one way to remedy the problem is through optical compensation techniques which were developed to correct for the distorted point spread function. This involved the use of conversion elements such as the spiral phase plate and the polarization mode converter. The characteristics of using these elements in the microscope were also elucidated. Experimental results showed that with the conversion elements, the point spread function can be engineered to give a single lobe with the peak at the origin. This result was corroborated by our theoretical model. Images of actin filaments in cells also showed an improvement in overall quality. Another contribution of this thesis is a demonstration of the increase in the resolution of surface plasmon microscopy. This method made use of two counter-propagating surface plasmon evanescent waves to form a standing-wave on the substrate. By stepping the phase of the standing-wave and collecting three separate images, a high resolution image can be synthesized. The resolution improvement was four times that of the conventional surface plasmon microscope. Finally, the use of surface plasmon in the confocal fluorescence microscope was studied. Instead of linearly polarized illumination, a radially polarized illumination was proposed to increase peak intensity

and a more symmetric point spread function. In addition, the efficiency of confocal detection was increased by the insertion of conversion elements. This was demonstrated both theoretically and experimentally.

While this thesis has contributed to the understanding of surface plamons in fluorescence microscopy, especially in terms of modeling as well as imaging characteristics, there still remains much to be explored. Future directions can include the study of grating launched surface plasmons and the effects of surface corrugations on coupling efficiency and imaging resolution. For instance, Sentenac and coworkers proposed using periodic nanostructures and plane wave illumination at various angles to synthesize a high resolution image which is below 100 nm (Sentenac et al. 2006). This technique has yet to be demonstrated experimentally. Another area that could be useful for future investigation is the optimization of surface plasmon structures for the sensing of biomolecules.

Bibliography

Alleyne, C. J., A. G. Kirk, R. C. McPhedran, N. P. Nicorovici, and D. Maystre (2007), "Enhanced SPR sensitivity using periodic metallic structures," *Opt. Express*, *15*(13), 8163-8169.

Amos, R. M., and W. L. Barnes (1997), "Modification of the spontaneous emission rate of Eu3+ ions close to a thin metal mirror," *Phys. Rev. B*, *55*(11), 7249-7254.

Arnison, M. (2002), "A 3D vectorial optical transfer function suitable for arbitrary pupil functions," *Opt. Commun.*, *211*(1-6), 53-63.

Arnoldus, H. F., and J. T. Foley (2004), "Transmission of dipole radiation through interfaces and the phenomenon of anti-critical angles," *J. Opt. Soc. Am. A*, *21*(6), 1109-1117.

Axelrod, D. (2001), "Total internal reflection fluorescence microscopy in cell biology," *Traffic*, *2*(11), 764-774.

Axelrod, D. (2003), "Total internal reflection fluorescence microscopy in cell biology," *Meth. Enzymol.*, *361*, 1-33.

Bewersdorf, J., R. Schmidt, and S. W. Hell (2006), "Comparison of I5M and 4Pi-microscopy," *J. Microsc.*, *222*(2), 105-117.

Biacore (2010), *Biacore Life Sciences, General Electric Inc.*

Biss, D. P., K. S. Youngworth, and T. G. Brown (2006), "Dark-field imaging with cylindrical-vector beams," *Appl. Opt.*, *45*(3), 470-479.

Borejdo, J., N. Calander, Z. Gryczynski, and I. Gryczynski (2006), "Fluorescence correlation spectroscopy in surface plasmon coupled emission microscope," *Opt. Express*, *14*(17), 7878-7888.

Borejdo, J., Z. Gryczynski, N. Calander, P. Muthu, and I. Gryczynski (2006), "Application of surface plasmon coupled emission to study of muscle," *Biophysical Journal*, *91*(7), 2626-2635.

Born, M., and E. Wolf (1999), *Principles of optics: electromagnetic theory of propagation, interference and diffraction of light*, 7th ed., Cambridge University Press, Cambridge; New York.

Bouhelier, A., F. Ignatovich, A. Bruyant, C. Huang, G. Colas des Francs, J. Weeber, A. Dereux, G. P. Wiederrecht, and L. Novotny (2007), "Surface plasmon interference excited by tightly focused laser beams," *Opt. Lett.*, *32*(17), 2535-2537.

Boutet de Monvel, J., S. Le Calvez, and M. Ulfendahl (2001), "Image restoration for confocal microscopy: improving the limits of deconvolution, with application to the visualization of the mammalian hearing organ," *Biophysical Journal*, *80*(5), 2455-2470.

Bozhevolnyi, S., J. Erland, K. Leosson, P. M. Skovgaard, and J. M. Hvam (2001), "Waveguiding in surface plasmon polariton band gap structures," *Phys. Rev. Lett.*, *86*(14), 3008-3011.

Brian, A. A., and H. M. McConnell (1984), "Allogeneic stimulation of cytotoxic T cells by supported planar membranes," *Proceedings of the National Academy of Sciences*, *81*, 6159-6163.

Burghardt, T., J. Charlesworth, M. Halstead, J. Tarara, and K. Ajtai (2006), "In situ fluorescent protein imaging with metal film-enhanced total internal reflection microscopy," *Biophysical Journal*, *90*(12), 4662-4671.

Campi, G. (2005), "Actin and agonist MHC-peptide complex-dependent T cell receptor microclusters as scaffolds for signaling," *Journal of Experimental Medicine*, *202*(8), 1031-1036.

Chance, R. R., A. Prock, and R. Silbey (1974), "Lifetime of an excited molecule near a metal mirror: Energy transfer in the Eu3+/silver system," *J. Chem. Phys.*, *60*(5), 2184-2185.

Chon, J. W. M., X. Gan, and M. Gu (2002), "Splitting of the focal spot of a high numerical-aperture objective in free space," *Appl. Phys. Lett.*, *81*(9), 1576-1578.

Chon, J. W. M., and M. Gu (2004), "Scanning total internal reflection fluorescence microscopy under one-photon and two-photon excitation: image formation," *Appl. Opt.*, *43*(5), 1063-1071.

Chung, E., D. Kim, Y. Cui, Y. Kim, and P. T. C. So (2007), "Two-dimensional standing wave total internal reflection fluorescence microscopy: superresolution imaging of single molecular and biological specimens," *Biophysical Journal*, *93*(5), 1747-1757.

Davis, J. A., G. H. Evans, and I. Moreno (2005), "Polarization-multiplexed diffractive optical elements with liquid-crystal displays," *Appl. Opt.*, *44*(19), 4049-4052.

Dorn, R., S. Quabis, and G. Leuchs (2003), "Sharper focus for a radially polarized light beam," *Phys. Rev. Lett.*, *91*(23), 2339011-2339014.

Drexhage, K. H. (1970), "Influence of a dielectric interface on fluorescence decay time," *Journal of Luminescence*, *1-2*, 693-701.

Dustin, M. L. et al. (1998), "A novel adaptor protein orchestrates receptor patterning and cytoskeletal polarity in T-cell contacts," *Cell*, *94*(5), 667-677.

Dustin, M. L. (2008), "T-cell activation through immunological synapses and kinapses," *Immunol. Rev*, *221*, 77-89.

Ebbesen, T. W., H. J. Lezec, H. F. Ghaemi, T. Thio, and P. A. Wolff (1998), "Extraordinary optical transmission through sub-wavelength hole arrays," *Nature*, *391*(6668), 667-669.

Edel, J., M. Wu, B. Baird, and H. G. Craighead (2005), "High spatial resolution observation of single-molecule dynamics in living cell membranes," *Biophysical Journal*, *88*(6), L43-L45.

Enderlein, J., and M. Bohmer (2003), "Influence of interface dipole interactions on the efficiency of fluorescence light collection near surfaces," *Opt. Lett.*, *28*(11), 941-943.

Evans, S. D., H. Allinson, N. Boden, T. M. Flynn, and J. R. Henderson (1997), "Surface plasmon resonance imaging of liquid crystal anchoring on patterned self-assembled monolayers," *J. Phys. Chem. B*, *101*(12), 2143-2148.

Fägerstam, L. G., Å. Frostell-Karlsson, R. Karlsson, B. Persson, and I. Rönnberg (1992), "Biospecific interaction analysis using surface plasmon resonance detection applied to kinetic, binding site and concentration analysis," *Journal of Chromatography A*, *597*(1-2), 397-410.

Fang, N., H. Lee, C. Sun, and X. Zhang (2005), "Sub-diffraction-limited optical imaging with a silver superlens," *Science*, *308*(5721), 534-537.

Fiolka, R., M. Beck, and A. Stemmer (2008), "Structured illumination in total internal reflection fluorescence microscopy using a spatial light modulator," *Opt Lett*, *33*(14), 1629-1631.

Ford, G. W., and W. Weber (1984), "Electromagnetic interactions of molecules with metal surfaces," *Physics Reports*, *113*(4), 195-287.

Fuerhapter, S., A. Jesacher, S. Bernet, and M. Ritsch-Marte (2005), "Spiral phase contrast imaging in microscopy," *Opt. Express*, *13*(3), 689-694.

Giebel, K., C. Bechinger, S. Herminghaus, M. Riedel, P. Leiderer, U. Weiland, and M. Bastmeyer (1999), "Imaging of cell/substrate contacts of living cells with surface plasmon resonance microscopy," *Biophysical Journal*, *76*(1), 509-516.

Gonzalez, R. (2002), *Digital image processing*, 2nd ed., Prentice Hall, Upper Saddle River N.J.

Grakoui, A., S. K. Bromley, C. Sumen, M. M. Davis, A. S. Shaw, P. M. Allen, and M. L. Dustin (1999), "The immunological synapse: a molecular machine controlling T cell activation," *Science*, *285*(5425), 221-227.

Gryczynski, I., J. Malicka, Z. Gryczynski, and J. R. Lakowicz (2004a), "Radiative decay engineering 4. Experimental studies of surface plasmon-coupled directional emission," *Analytical Biochemistry*, *324*(2), 170-182.

Gryczynski, I., J. Malicka, Z. Gryczynski, and J. R. Lakowicz (2004b), "Surface plasmon-coupled emission with gold films," *J. Phys. Chem. B*, *108*(33), 12568-12574.

Gryczynski, Z., J. Borejdo, N. Calander, E. Matveeva, and I. Gryczynski (2006), "Minimization of detection volume by surface-plasmon-coupled emission," *Analytical Biochemistry*, *356*(1), 125-131.

Gu, M. (1996), *Principles of three dimensional imaging in confocal microscopes*, World Scientific, Singapore; River Edge N.J.

Gu, M. (2000), *Advanced optical imaging theory*, Springer, Berlin; New York.

He, R., G. Chang, H. Wu, C. Lin, K. Chiu, Y. Su, and S. Chen (2006), "Enhanced live cell membrane imaging using surface plasmon-enhanced total internal reflection fluorescence microscopy," *Opt. Express*, *14*(20), 9307-9316.

Hecht, E. (2002), *Optics*, 4th ed., Addison-Wesley, Reading Mass.

Hellen, E. H., and D. Axelrod (1987), "Fluorescence emission at dielectric and metal-film interfaces," *J. Opt. Soc. Am. B*, *4*(3), 337-350.

Huang, X., P. K. Jain, I. H. El-Sayed, and M. A. El-Sayed (2007), "Plasmonic photothermal therapy (PPTT) using gold nanoparticles," *Lasers Med. Sci.*, *23*(3), 217-228.

Hung, Y., I. I. Smolyaninov, C. C. Davis, and H. Wu (2006), "Fluorescence enhancement by surface gratings," *Opt. Express*, *14*(22), 10825-10830.

Huppa, J. B., and M. M. Davis (2003), "T-cell-antigen recognition and the immunological synapse," *Nat. Rev. Immunol*, *3*(12), 973-983.

Irvine, D. J., M. A. Purbhoo, M. Krogsgaard, and M. M. Davis (2002), "Direct observation of ligand recognition by T cells," *Nature*, *419*(6909), 845-849.

Kah, J. C. Y., T. H. Chow, B. K. Ng, S. G. Razul, M. Olivo, and C. J. R. Sheppard (2009), "Concentration dependence of gold nanoshells on the enhancement of optical coherence tomography images: a quantitative study," *Appl. Opt.*, *48*(10), D96-D108.

Kano, H. (2000), "A scanning microscope employing localized surface-plasmon-polaritons as a sensing probe," *Opt. Commun.*, *182*(1-3), 11-15.

Kawata, S. (2001), *Near-field optics and surface plasmon polaritons*, Springer Berlin Heidelberg, Berlin, Heidelberg.

Kitson, S. C., W. L. Barnes, J. R. Sambles, and N. P. K. Cotter (1996), "Excitation of molecular fluorescence via surface plasmon polaritons," *J. Mod. Opt.*, *43*(3), 573-582.

Krogsgaard, M., Q. Li, C. Sumen, J. B. Huppa, M. Huse, and M. M. Davis (2005), "Agonist/endogenous peptide-MHC heterodimers drive T cell activation and sensitivity," *Nature*, *434*(7030), 238-243.

Lakowicz, J. R. (2004), "Radiative decay engineering 3. Surface plasmon-coupled directional emission," *Analytical Biochemistry*, *324*(2), 153-169.

Lakowicz, J. R. (2005), "Radiative decay engineering 5: metal-enhanced fluorescence and plasmon emission," *Analytical Biochemistry*, *337*(2), 171-194.

Lakowicz, J. R., J. Malicka, I. Gryczynski, and Z. Gryczynski (2003), "Directional surface plasmon-coupled emission: a new method for high sensitivity detection," *Biochemical and Biophysical Research Communications*, *307*(3), 435-439.

Larkin, K. G., D. J. Bone, and M. A. Oldfield (2001), "Natural demodulation of two-dimensional fringe patterns. I. General background of the spiral phase quadrature transform," *J. Opt. Soc. Am. A*, *18*(8), 1862-1870.

Lee, K. et al. (2003), "The immunological synapse balances T cell receptor signaling and degradation," *Science*, *302*(5648), 1218-1222.

Lee, K., A. D. Holdorf, M. L. Dustin, A. C. Chan, P. M. Allen, and A. S. Shaw (2002), "T cell receptor signaling precedes immunological synapse formation," *Science*, *295*(5559), 1539-1542.

Levene, M. J., J. Korlach, S. W. Turner, M. Foquet, H. G. Craighead, and W. W. Webb (2003), "Zero-mode waveguides for single-molecule analysis at high concentrations," *Science*, *299*(5607), 682-686.

Liedberg, B. (1983), "Surface plasmon resonance for gas detection and biosensing," *Sensors and Actuators*, *4*(1), 299-304.

Lin, A. W. H., N. A. Lewinski, J. L. West, N. J. Halas, and R. A. Drezek (2005), "Optically tunable nanoparticle contrast agents for early cancer detection: model-based analysis of gold nanoshells," *J. Biomed. Opt.*, *10*(6), 064035.

Liu, Z., H. Lee, Y. Xiong, C. Sun, and X. Zhang (2007), "Far-field optical hyperlens magnifying sub-diffraction-limited objects," *Science*, *315*(5819), 1686-1686.

Liu, Z., Q. Wei, and X. Zhang (2005), "Surface plasmon interference nanolithography," *Nano Lett.*, *5*(5), 957-961.

Loo, C., A. Lowery, N. Halas, J. West, and R. Drezek (2005), "Immunotargeted nanoshells for integrated cancer imaging and therapy," *Nano Lett.*, *5*(4), 709-711.

Lucy, L. B. (1974), "An iterative technique for the rectification of observed distributions," *Astronomical Journal*, *79*, 745-747.

Lukosz, W. (1966), "Optical Systems with Resolving Powers Exceeding the Classical Limit," *J. Opt. Soc. Am.*, *56*(11), 1463-1471.

Lukosz, W., and R. E. Kuhn (1977), "Fluorescence lifetime of magnetic and electric dipoles near a dielectric interface," *Optics Communications*, *20*(2), 195-199.

Mair, A., A. Vaziri, G. Weihs, and A. Zeilinger (2001), "Entanglement of the orbital angular momentum states of photons," *Nature*, *412*(6844), 313-316.

Malicka, J., I. Gryczynski, Z. Gryczynski, and J. R. Lakowicz (2003), "DNA hybridization using surface plasmon-coupled emission," *Analytical Chemistry*, *75*(23), 6629-6633.

Matveeva, E., Z. Gryczynski, I. Gryczynski, and J. R. Lakowicz (2004), "Immunoassays based on directional surface plasmon-coupled emission," *Journal of Immunological Methods*, *286*(1-2), 133-140.

Matveeva, E., Z. Gryczynski, I. Gryczynski, J. Malicka, and J. R. Lakowicz (2004), "Myoglobin immunoassay utilizing directional surface plasmon-coupled emission," *Analytical Chemistry*, *76*(21), 6287-6292.

McConnell, H. M., T. H. Watts, R. M. Weis, and A. A. Brian (1986), "Supported planar membranes in studies of cell-cell recognition in the immune system," *Biochim. Biophys. Acta*, *864*(1), 95-106.

Moh, K. J., X. Yuan, J. Bu, S. W. Zhu, and B. Z. Gao (2008), "Surface plasmon resonance imaging of cell-substrate contacts with radially polarized beams," *Opt. Express*, *16*(25), 20734-20741.

Moh, K. J., X. Yuan, J. Bu, S. W. Zhu, and B. Z. Gao (2009), "Radial polarization induced surface plasmon virtual probe for two-photon fluorescence microscopy," *Opt. Lett.*, *34*(7), 971-973.

Monks, C. R., B. A. Freiberg, H. Kupfer, N. Sciaky, and A. Kupfer (1998), "Three-dimensional segregation of supramolecular activation clusters in T cells," *Nature*, *395*(6697), 82-86.

Nanophoton Corp. (2010), *Nanophoton Corporation, Z polarization device (ZPol)*.

Neil, M. A. A., R. Juskaitis, and T. Wilson (1997), "Method of obtaining optical sectioning by using structured light in a conventional microscope," *Opt. Lett.*, *22*(24), 1905-1907.

O'Keefe, J. P., and T. F. Gajewski (2005), "Cutting edge: cytotoxic granule polarization and cytolysis can occur without central supramolecular activation cluster formation in CD8+ effector T cells," *J. Immunol*, *175*(9), 5581-5585.

Palik, E. D. (1997), *Handbook of optical constants of solids*, Academic Press.

Pawley, J. (2006), *Handbook of biological confocal microscopy*, 3rd ed., Springer, New York N.Y.

Pendry, J. (2000), "Negative refraction makes a perfect lens," *Phys. Rev. Lett.*, *85*(18), 3966-3969.

Piliarik, M., H. Vaisocherová, and J. Homola (2005), "A new surface plasmon resonance sensor for high-throughput screening applications," *Biosensors and Bioelectronics*, *20*(10), 2104-2110.

Purbhoo, M. A., D. J. Irvine, J. B. Huppa, and M. M. Davis (2004), "T cell killing does not require the formation of a stable mature immunological synapse," *Nat. Immunol*, *5*(5), 524-530.

Raether, H. (1988), *Surface plasmons on smooth and rough surfaces and on gratings*, Springer-Verlag, Berlin; New York.

Richards, B., and E. Wolf (1959), "Electromagnetic diffraction in optical systems. II. Structure of the image field in an aplanatic system," *Proc. Roy. Soc. London A*, *253*(1274), 358-379.

Richardson, W. (1972), "Bayesian-based iterative method of image restoration," *J. Opt. Soc. Am.*, *62*(1), 55-59.

Rothenhäusler, B., and W. Knoll (1988), "Surface-plasmon microscopy," *Nature*, *332*(6165), 615-617.

Saito, T., and T. Yokosuka (2006), "Immunological synapse and microclusters: the site for recognition and activation of T cells," *Curr. Opin. Immunol*, *18*(3), 305-313.

Schmelzeisen, M., J. Austermann, and M. Kreiter (2008), "Plasmon mediated confocal dark-field microscopy," *Opt. Express*, *16*(22), 17826-17841.

Schmid, E. L., A. P. Tairi, R. Hovius, and H. Vogel (1998), "Screening ligands for membrane protein receptors by total internal reflection fluorescence: the 5-HT3 serotonin receptor," *Anal. Chem.*, *70*(7), 1331-1338.

Schönle, A., and S. W. Hell (2002), "Calculation of vectorial three-dimensional transfer functions in large-angle focusing systems," *J. Opt. Soc. Am. A*, *19*(10), 2121-2126.

Schurig, D., J. J. Mock, B. J. Justice, S. A. Cummer, J. B. Pendry, A. F. Starr, and D. R. Smith (2006), "Metamaterial electromagnetic cloak at microwave frequencies," *Science*, *314*(5801), 977-980.

Selvaraj, P., M. L. Plunkett, M. Dustin, M. E. Sanders, S. Shaw, and T. A. Springer (1987), "The T lymphocyte glycoprotein CD2 binds the cell surface ligand LFA-3," *Nature*, *326*(6111), 400-403.

Sentenac, A., P. Chaumet, and K. Belkebir (2006), "Beyond the Rayleigh criterion: grating assisted far-field optical diffraction tomography," *Phys. Rev. Lett.*, *97*(24), 2439011-2439014.

Sheppard, C. J. R., and A. Choudhury (2004), "Annular Pupils, Radial Polarization, and Superresolution," *Appl. Opt.*, *43*(22), 4322.

Sheppard, C. J. R., and K. C. Larkin (1997), "Vectorial pupil functions and vectorial transfer functions," *Optik*, *107*(2), 79-87.

Simpson, N. B., L. Allen, and M. J. Padgett (1996), "Optical tweezers and optical spanners with Laguerre-Gaussian modes," *J. Mod. Opt.*, *43*(12), 2485-2491.

Slavík, R., and J. Homola (2007), "Ultrahigh resolution long range surface plasmon-based sensor," *Sensors and Actuators B: Chemical*, *123*(1), 10-12.

Smolyaninov, I. I., Y. Hung, and C. C. Davis (2007), "Magnifying superlens in the visible frequency range," *Science*, *315*(5819), 1699-1701.

So, P. T., H. S. Kwon, and C. Y. Dong (2001), "Resolution enhancement in standing-wave total internal reflection microscopy: a point-spread-function engineering approach," *J. Opt. Soc. Am. A*, *18*(11), 2833-2845.

Somekh, M. G. (2002), "Surface plasmon fluorescence microscopy: an analysis," *J. Microsc.*, *206*(2), 120-131.

Sönnichsen, C., B. M. Reinhard, J. Liphardt, and A. P. Alivisatos (2005), "A molecular ruler based on plasmon coupling of single gold and silver nanoparticles," *Nat. Biotechnol.*, *23*(6), 741-745.

Stabler, G., M. G. Somekh, and C. W. See (2004), "High-resolution wide-field surface plasmon microscopy," *J. Microsc.*, *214*(3), 328-333.

Stalder, M., and M. Schadt (1996), "Linearly polarized light with axial symmetry generated by liquid-crystal polarization converters," *Opt. Lett.*, *21*(23), 1948-1950.

Stefani, F., K. Vasilev, N. Bocchio, N. Stoyanova, and M. Kreiter (2005), "Surface-plasmon-mediated single-molecule fluorescence through a thin metallic film," *Phys. Rev. Lett.*, *94*(2), 0230051-0230054.

Steyer, J. A., H. Allinson, and W. Almers (1997), "Transport, docking and exocytosis of single secretory granules in live chromaffin cells," *Nature*, *388*(6641), 474-478.

Sund, S., and D. Axelrod (2000), "Actin dynamics at the living cell submembrane imaged by total internal reflection fluorescence photobleaching," *Biophysical Journal*, *79*(3), 1655-1669.

Takai, Y., M. L. Reed, S. J. Burakoff, and S. H. Herrmann (1987), "Direct evidence for a receptor-ligand interaction between the T-cell surface antigen CD2 and lymphocyte-function-associated antigen 3," *Proc. Natl. Acad. Sci. U.S.A*, *84*(19), 6864-6868.

Tanaka, T., and S. Kawata (2005), "Real-time observation of birefringence by laser-scanning surface plasmon resonance microscope," *Opt. Express*, *13*(18), 6905-6911.

Tanaka, T., and S. Yamamoto (2003), "Laser-scanning surface plasmon polariton resonance microscopy with multiple photodetectors," *Appl. Opt.*, *42*(19), 4002-4007.

Tang, W. T., E. Chung, Y. Kim, P. T. C. So, and C. J. R. Sheppard (2007), "Investigation of the point spread function of surface plasmon-coupled emission microscopy," *Opt. Express*, *15*(8), 4634-4646.

Tidwell, S. C., D. H. Ford, and W. D. Kimura (1990), "Generating radially polarized beams interferometrically," *Appl. Opt.*, *29*(15), 2234-2239.

Török, P., P. D. Higdon, and T. Wilson (1998), "Theory for confocal and conventional microscopes imaging small dielectric scatterers," *J. Mod. Opt.*, *45*(8), 1681-1698.

Török, P., and C. J. R. Sheppard (2002), "The role of pinhole size in high-aperture two- and three-photon microscopy," in *Confocal and two-photon microscopy: foundations, applications, and advances*, pp. 127-151, Wiley-Liss, New York.

Török, P., and P. Varga (1997), "Electromagnetic diffraction of light focused through a stratified medium," *Appl. Opt.*, *36*(11), 2305-2312.

Varma, R., G. Campi, T. Yokosuka, T. Saito, and M. L. Dustin (2006), "T Cell Receptor-Proximal Signals Are Sustained in Peripheral Microclusters and Terminated in the Central Supramolecular Activation Cluster," *Immunity*, *25*(1), 117-127.

Vasilev, K., F. D. Stefani, V. Jacobsen, W. Knoll, and M. Kreiter (2004), "Reduced photobleaching of chromophores close to a metal surface," *J. Chem. Phys.*, *120*(14), 6701-6704.

Veselago, V. G. (1968), "The electrodynamics of substances with simultaneous negative values of epsilon and mu," *Soviet Physics Uspekhi*, (4), 509-514.

Watts, T. H., A. A. Brian, J. W. Kapples, P. Marrack, and H. M. McConnell (1984), "Antigen presentation by supported planar membranes containing affinity-purified I-Ad," *Proceedings of the National Academy of Sciences*, *81*(23), 7564-7568.

Weeber, J., A. Dereux, J. R. Krenn, and J. Goudonnet (1999), "Plasmon polaritons of metallic nanowires for controlling submicron propagation of light," *Phys. Rev. B*, *60*(12), 9061-9068.

Weyl, H. (1919), "Ausbreitung elektromagnetischer Wellen uber einem ebenen Leiter," *Annalen der Physik*, *365*(21), 481-500.

Wolf, E. (1959), "Electromagnetic diffraction in optical systems. I. An integral representation of the image field," *Proc. Roy. Soc. London A*, *253*(1274), 349-357.

Yamaguchi, R., T. Nose, and S. Sato (1989), "Liquid crystal polarizers with axially symmetrical properties," *Jpn. J. Appl. Phys.*, *28*(Part 1, No. 9), 1730-1731.

Ye, C. (1995), "Construction of an optical rotator using quarter-wave plates and an optical retarder," *Opt. Eng.*, *34*(10), 3031-3035.

Yeatman, E., and E. A. Ash (1987), "Surface plasmon microscopy," *Electron. Lett.*, *23*(20), 1091-1092.

Yokosuka, T., and T. Saito (2010), "The immunological synapse, TCR microclusters, and T cell activation," *Curr. Top. Microbiol. Immunol*, *340*, 81-107.

Yokosuka, T., K. Sakata-Sogawa, W. Kobayashi, M. Hiroshima, A. Hashimoto-Tane, M. Tokunaga, M. L. Dustin, and T. Saito (2005), "Newly generated T cell receptor microclusters initiate and sustain T cell activation by recruitment of Zap70 and SLP-76," *Nat Immunol*, *6*(12), 1253-1262.

Yokota, H., K. Saito, and T. Yanagida (1998), "Single molecule imaging of fluorescently labeled proteins on metal by surface plasmons in aqueous solution," *Phys. Rev. Lett.*, *80*(20), 4606-4609.

Yoshiki, K., K. Ryosuke, M. Hashimoto, T. Araki, and N. Hashimoto (2007), "Second-harmonic-generation microscope using eight-segment polarization-mode converter to observe three-dimensional molecular orientation," *Opt. Lett.*, *32*(12), 1680-1682.

Publications

Journals

W. T. Tang, E. Chung, Y. Kim, C. J. R. Sheppard, P. T. C. So, "Investigation of the point spread function of surface plasmon coupled emission microscopy", Opt. Express, Vol. 15, No. 8, 4634-4646 (2007)

W. T. Tang, E. Chung, Y. Kim, C. J. R. Sheppard, P. T. C. So, "Effects of using a metal layer in total internal reflection fluorescence microscopy", Appl. Phys. A, 89, 333-335 (2007)

W. T. Tang, Elijah Y. S. Yew, C. J. R. Sheppard, "Polarization conversion in confocal microscopy with radially polarized illumination, Opt. Lett. 34, 2147 (2009)

C. J. R. Sheppard, S. Rehman, N. K. Balla, Elijah Y. S. Yew, W. T. Tang, "Bessel beams: effects of polarization," Opt. Comm. 282, 4647-4656 (2009)

E. Chung, Y. Kim, W. T. Tang, C. J. R. Sheppard, P. T. C. So, "Wide-field extended-resolution fluorescence microscopy with standing surface-plasmon-resonance waves," Opt. Lett. 34(15), 2366 (2009)

W. T. Tang, E. Chung, Y. Kim, C. J. R. Sheppard, P. T. C. So, "Surface plasmon-coupled emission microscopy with a spiral phase plate", Opt. Lett., 35, 517-519 (2010)

Conferences

W. T. Tang*, E. Chung, Y. Kim, P. T. C. So, C. J. R. Sheppard, "Effects of using a metal layer in total internal reflection fluorescence microscopy," International Workshop on Plasmonics and Applications in Nanotechnologies, Singapore (2006)

E. Chung*, W. T. Tang, Y. Kim, C. J. R. Sheppard, P. T. C. So, "Towards the standing wave surface plasmon resonance fluorescence microscopy", Photonics West, Plasmonics in Biology and Medicine, San Jose, USA (2007)

W. T. Tang*, E. Chung, Y. Kim, P. T. C. So, C. J. R. Sheppard, "Surface plasmon microscopy", 5th International Symposium on Nanomanufacturing (ISNM-5), Singapore (2008)

W. T. Tang*, E. Chung, Y. Kim, P. T. C. So, C. J. R. Sheppard, "Surface plasmon enhancement of total internal reflection fluorescence for biosensors", Optics within Life Sciences 10, Biophotonics Asia 2008, Singapore (2008)

W. T. Tang*, P. T. C. So, C. J. R. Sheppard, "Surface plasmon coupled emission microscopy and its vectorial optical transfer function", The 4th Asian and Pacific Rim Symposium on Biophotonics, Jeju, Korea (2009)

W. T. Tang, C. J. R. Sheppard*, "Application of spiral phase plate in surface plasmon microscopy", Focus on Microscopy, Shanghai, China (2010)